DEVELOPMENT OF PHASE STABILIZED SWEPT SOURCE OPTICAL COHERENCE TOMOGRAPHY FOR BIOMEDICAL IMAGING AND SENSING

A Dissertation

Presented to

the Faculty of the Department of Mechanical Engineering

University of Houston

In Partial Fulfillment

of the Requirements for the Degree of

Doctor of Philosophy

in Mechanical Engineering

by

Ravi Kiran Manapuram

August 2012

DEVELOPMENT OF PHASE STABILIZED SWEPT SOURCE OPTICAL COHERENCE TOMOGRAPHY FOR BIOMEDICAL IMAGING AND SENSING

_____
(Ravi Kiran Manapuram)

Approved:

_____
Chairman of the Committee
Kirill V. Larin, Associate Professor
Biomedical Engineering
Mechanical Engineering

Committee Members:

_____
Pradeep Sharma, Professor
Mechanical Engineering

_____
Matthew Franchek, Professor
Mechanical Engineering

_____
Ralph Metcalfe, Professor
Mechanical Engineering

_____
Lowell Wood, Professor
Physics Department

_____
Suresh K. Khator, Associate Dean
Cullen College of Engineering

_____
Pradeep Sharma, Professor and Chairman,
MechanicalEngineering

ACKNOWLEDGEMENTS

I am extremely thankful to my advisor, Dr. Kirill Larin, for his guidance and support throughout this work. I would like to convey my gratitude for all the time he spent on for this project to make it as flawless as possible. I would like to thank Dr. Sharma, Dr. Wood, Dr. Metcalfe and Dr. Franchek for serving on my committee.

I would like to thank my lab members and friends especially Naren, Maleeha, Shang, Floredes, Jiasong, Venu, Steven, Esteban, Mohamad, Saba, Dr. Ghosn and Dr. Baranov for continuously helping and motivating me for completing my studies. I would also like to thank Dr. Larina, Maleeha, Shang, Floredes and Saba for helping me with *in vivo* experiments.

I owe special thanks to my parents, my brother Eswar, my sister Smita, my brother-in-law Srinivas, my niece Sruti and my colleague Maleeha for always encouraging me and supporting me with patience throughout my PhD studies. Therefore, I would like to dedicate my dissertation to them.

DEVELOPMENT OF PHASE STABILIZED SWEPT SOURCE OPTICAL COHERENCE TOMOGRAPHY FOR BIOMEDICAL IMAGING AND SENSING

An Abstract

of a

Dissertation

Presented to

the Faculty of the Department of Mechanical Engineering

University of Houston

In Partial Fulfillment

of the Requirements for the Degree

Doctor of Philosophy

in Mechanical Engineering

by

Ravi Kiran Manapuram

August 2012

ABSTRACT

Several life-threatening diseases could either be cured or be eased by diagnosing them during earlier stages. Currently, medical imaging is one of the most reliable methods of disease diagnostics. This dissertation describes the development of a medical imaging device that has a great potential for early diagnosis of various diseases. The developed system utilizes optical coherence tomography (OCT) and is capable of 3D imaging of tissues with near cellular resolution noninvasively. It is also capable of sensing minute changes in tissue refractive index or surface displacement via phase-sensitive measurements. The system showed an axial resolution of 8 μm, lateral resolution of 15 μm, an imaging depth of 9 mm, signal to noise ratio of 101 dB and a phase stability of 9 mrad.

After development, the system was applied to several biomedical applications such as the detection of microbubbles in mice tails *in vivo* and mechanical wave propagation in mice corneas *in vivo.* In the live mice tails, microbubbles of sizes as small as 50 μm were detected, therefore indicating the capability of the system to serve as an early diagnostic tool for diseases caused by decompression sickness or gas emboli.

Apart from imaging, this dissertation also describes a method to apply OCT for elastography applications. Results demonstrate that the system is capable of measuring amplitude of mechanical waves as small as 30 nm. The high sensitivity of the system was exploited to measure wave propagation in live mice corneas as a function of age. To the best of our knowledge, this is the first time OCT has been applied to measure wave parameters in ocular tissues *in vivo.*

TABLE OF CONTENTS

LIST OF FIGURES

LIST OF TABLES

I. CHAPTER 1. INTRODUCTION

Successful treatment and accurate diagnostics of many devastating diseases rely on the availability of imaging devices. In the past few decades, several new imaging technologies have emerged that have revolutionized the diagnosis and clinical management of different diseases. This thesis presents development of an optical imaging device with a motive to translate it to an early diagnostic tool. It utilizes relatively new technology called optical coherence tomography (OCT) that allows noninvasive 3D imaging of biological samples under *in vivo* conditions based on the endogenous contrast mechanism (*e.g*., no need for tissue staining or labeling).

In particular, the system was applied to detect and quantify microbubbles in the arteries of mice tails with a resolution of 8 μm. The device was then modified to enable high sensitive elastography measurements while maintaining its imaging capabilities. High sensitive elastography measurements allowed better understanding of wave propagation through ocular tissues. For example, it was shown that the wave velocities in older mice corneas are higher than younger mice in live conditions. From all these findings, it can be stated that the developed device has the potential to reveal the pathologies of various tissues under *in vivo* conditions.

This dissertation is organized as follows: the introduction overviews different imaging techniques and introduces optical coherence tomography. Chapter II deals with the detailed description of instrumentation and design of phase-stabilized swept source OCT (PhS-SSOCT) system. Chapter III discusses the imaging of stationary and circulating microbubbles and the applications of the system for detection of microbubbles in tissue-simulating phantoms, blood, and animals *in vivo*. The application of the system for quantifying mechanical wave parameters propagating on tissue surfaces (elastography) is discussed in Chapter IV. Finally Chapter V summarizes all the achievements and the outcomes of the dissertation and also discusses future work.

1.1 Overview of imaging techniques

The most common clinical imaging modalities include X-ray imaging (Radiography, X-ray computed tomography (CT) and Fluoroscopy), Magnetic Resonance Imaging (MRI), Ultrasound imaging (US), and Nuclear medicine (positron emission tomography (PET) and single photon emission computed tomography (SPECT)). These techniques differ in the principle of operation.

Although they all provide 3D visualization of the tissues with spatial resolution only in the order of millimeters, each one of them has their own advantages. For example, X-ray imaging is performed by sending X-ray radiations and images constructed from the attenuation of the radiation [1]. Although X-ray imaging provides low contrast images with limited resolution and no possibility of functional studies, it still provides with deeper imaging of tissues [2]. Needless to say, it uses ionizing radiation which is linked to DNA damage and tumor development [3].

Similarly, in nuclear medicine, samples are labeled with radioactive materials and through nuclear delays; gamma-rays are emitted and detected. Nuclear imaging offers high sensitivity, deep imaging depth and relatively good spatial resolution [4]. However, this technique requires pre-imaging preparations and studies suggested that this technique cannot be applied to some patients due to its high risks of diseases caused by radioactive radiation exposures [5].

On similar lines, in MRI, images are constructed by detecting the resonating H nuclei due to the exposed magnetic field. It offers excellent contrast, imaging depth and also allows functional studies [6, 7]. However, imaging is very slow. Similarly, ultrasonography (US) detects the reflection of ultrasonic pulses transmitted into the body. It offers good imaging depth and relatively good spatial resolution. Yet it is limited by the depth resolution [8]. Table 1 below summarizes all the above imaging modalities. It can be seen that each technique has to its own limitations. Further analysis of Table 1 shows that optical imaging techniques and US techniques meet the optimal characteristic features. Head to head comparison of these two techniques reveals

that optical techniques offer higher contrast images over US. Therefore, there is a great interest in developing devices based on optical techniques.

Table 1: Characteristics of various medical imaging technologies (adapted from [9])

Characteristics	X-ray	US	MRI	Nuclear	Optical
Contrast	Poor	Good	Excellent	Good	Excellent
Spatial resolution	Excellent	Good	Good	Good	Good
Imaging depth	Excellent	Good	Excellent	Excellent	Good
Function	No	Yes	Yes	Yes	Yes
Data Acquisition	Fast	Fast	Slow	Slow	Fast
Non-ionizing radiation	No	Yes	Yes	No	Yes

Optical imaging is one of the fastest growing imaging modalities for medical diagnostics as it can provide a pathological examination of tissues with sub cellular resolution. Optical imaging utilizes nonionizing radiation, provides excellent tissue contrast, spatial resolution in the order of micrometers and also allows functional imaging. However, due to strong attenuation of light in tissue, imaging depth obtained by optical imaging techniques is limited. One of the optical imaging techniques that allow 3D imaging of tissues at depths up to several millimeters is OCT. This technique was introduced in 1991 to perform tomographic imaging of the human eye [10]. Since then, OCT has been actively developed by several research groups for many clinical diagnostic applications (reviewed in [11-13]). This doctoral thesis describes the development of a phase-sensitive OCT that allows not only noninvasive 3D real time imaging of tissues with

resolution of a few micrometers but also depth resolved sensing of mechanical deformation with an angstrom resolution.

1.2 Optical coherence tomography (OCT)

OCT is an emerging noninvasive imaging modality that enables *in vivo* 3D visualization of internal microstructures. Presently, OCT is being applied in many fields such as ophthalmology, gastroenterology, cardiology, dentistry, *etc.* OCT in its early stages of development was applied to obtain images of the retina *in vivo* and coronary arteries *ex vivo* [10, 14].

In vivo images of the human retina revealed retinal structures with higher resolution than any other imaging method and soon it has become a standard of care in clinical ophthalmology[15]. Clinical studies investigated OCT for diagnosis and monitoring of many macular diseases such as macular edema, central serous retinopathy and age related macular degeneration, choroidal neo vascularization and glaucoma by measuring the retinal layer thicknesses. Advancements in OCT in the field of ophthalmology have already delivered many commercial OCT systems for clinical applications. Therefore, OCT is one of the technologies favorable for developing clinical imaging and diagnostic tools.

OCT is based on principles of low-coherence interferometry (LCI). LCI is a measurement technique developed for characterization of optical components with high axial resolution which is determined by the coherence length of the light source [16, 17]. The first biological application of LCI was in the ophthalmologic biometry for the measurement of eye length [18]. Since then, related versions of this technique have been developed for non-invasive high-precision and high-resolution biometry [19].

LCI measures the field of the optical beam rather than its intensity. The functional form of the electric field in a light wave is

$$E(t) = E_0 \cos\left(2\pi\nu t - \frac{2\pi}{\lambda} z\right),$$

Equation 1

where ν is the frequency of the wave, t is the time of propagation, λ is the wavelength and z is the propagation distance. In a simple Michelson's interferometer, the reference beam field $E_r(t)$ coherently combines with the sample arm field $E_s(t)$ and interferes to form fringes.

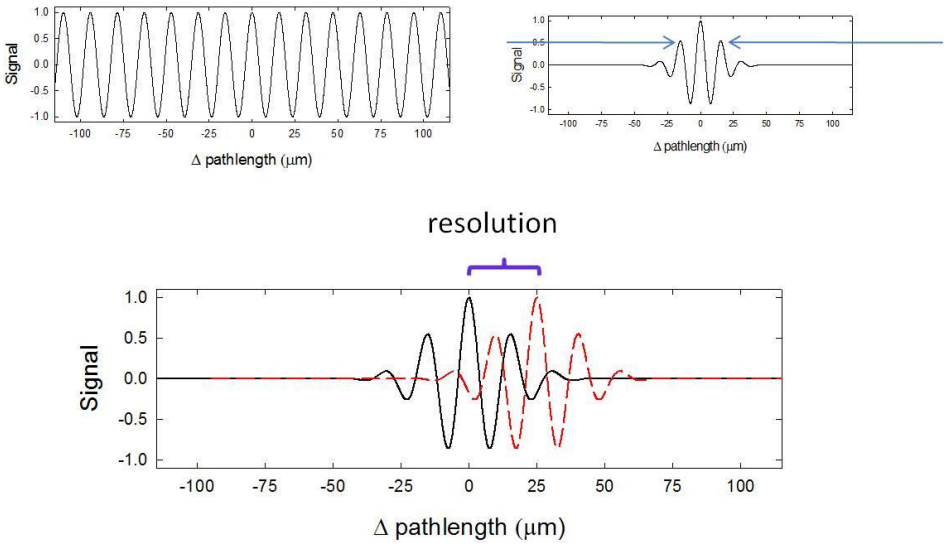

Figure 1: Interferometric signal: (a) long coherence source (b) short coherence source (c) signal with two reflectors separated at 25 microns.

A detector measures the output intensity which is proportional to the square of the electromagnetic field, and if Δl is the difference in the lengths of the reference and sample arms, then the intensity of the interferometer output is given by Equation 2,

$$I_0(t) = |E_r(t) + E_s(t)|^2 \sim |E_r|^2 + |E_s|^2 + E_r E_s \cos\left(2\frac{2\pi}{\lambda}\Delta l\right).$$

Equation 2

The cosine term contains the interference information which depends on Δl, which suggests that the frequency of the cosine term contains the difference in pathlengths. Also, it can be seen that a sharp cosine envelop or a short time duration cosine term can resolve small changes in the

pathlength (as shown in Figure 1). Therefore, high depth resolved information could be obtained by low-coherence light or broad bandwidth sources. However, laser sources with low coherence length limit the depth range where the fringes are formed. To obtain depth-wise imaging, TDOCT implements a scanning mirror that scans along the sample depth to collect the coherent back scattering light. Interference fringes from every depth is collected and used to construct depth-wise images. More recently, spectral information is used to obtain the depth-wise images. The former is called time domain OCT (TDOCT) and the later one is called Fourier domain OCT (FDOCT). The details of the implementation in both the cases are described below.

1.2.1 Time domain OCT (TDOCT)

The basic principle of the OCT is to detect backscattered photons from a tissue of interest within a coherence length of the source using a two-beam interferometer (Figure 2), [10]. A broadband low-coherent laser source is split equally using a beam splitter into two arms, the reference arm and the sample arm. The back-scattered light from the sample recombines with the light in the reference arm. This recombination results in the formation of fringes, as the distance travelled by light in both arms do not differ by more than the coherence length of the laser source just like in LCI.

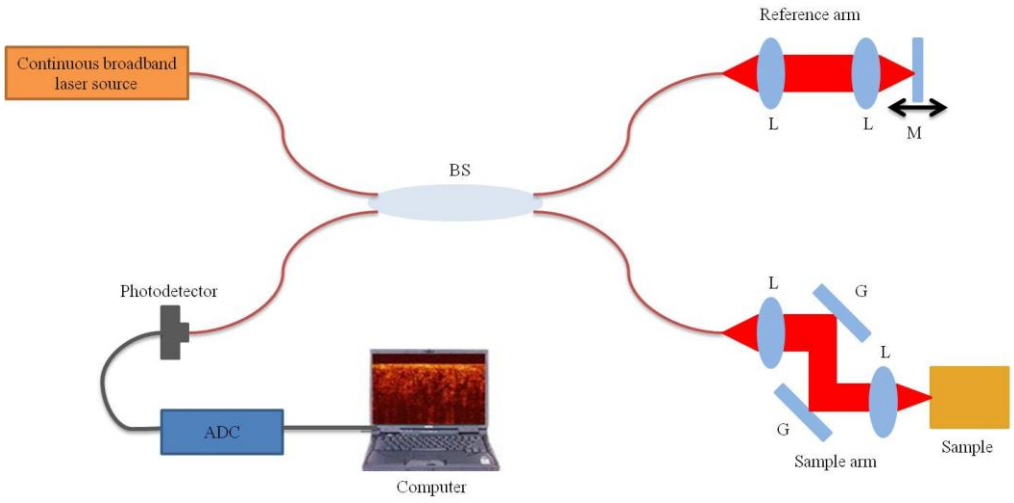

Figure 2: The schematic of a conventional TDOCT.

In the time domain configuration, the echo time delay is measured by moving the reference arm parallel to the tissue depth as shown in Figure 2. Back scattered photons from each depth is obtained at different times with the mirror movement making the information time encoded. The interference signals are recorded by the photo detector. The recorded interference data at points across the surface is gathered by scanning the galvanometer mounted mirror. Cross sectional 2-D images can be constructed in real-time.

1.2.2 Spectral domain OCT (SDOCT)

Recently, novel OCT detection techniques have emerged which do not require mechanical in-depth scanning and can achieve very high detection sensitivities, enabling OCT imaging with a high increase in imaging speed over TDOCT systems. A broadband source is used, where different wavelengths probe into different depths and the depth information is spectrally coded that can be extracted by Fourier transforming the interference fringes making them Fourier domain Optical Coherence Tomography (FDOCT), [11, 13, 20-22]. Fourier domain OCT detection can be performed in two ways: Spectral Domain OCT (SDOCT), using a broadband light source and a spectrometer with a multi-channel analyzer or Swept Source OCT (SSOCT), using a rapidly tunable, narrow line-width laser source [23]. Spectral domain detection techniques measure the echo time delay of light by using an interferometer with a broadband light source and measure the spectrum of the interferometer output. Back reflections or backscattering from the tissue at different delays produces oscillations or fringes in the interference spectrum. Increasing delay differences produces higher frequency oscillations. Thus, the magnitude and delay of the light from the tissue can be measured by the Fourier transform of the interference spectrum.

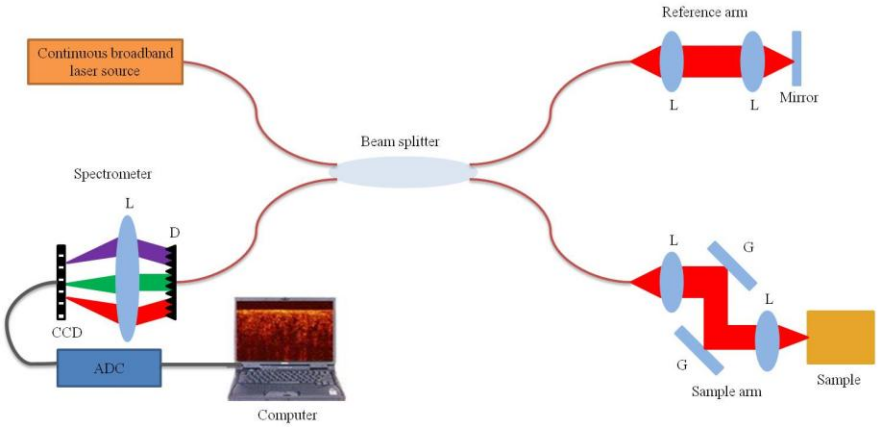

Figure 3: The schematic of a SDOCT.

In SDOCT, backscattered low-coherence light is mixed with a reference beam by an interferometer, and each spectral component is separated by a grating-based spectrometer and detected using a linear detector array as shown in Figure 3. The detected signal is expressed as [24]

$$I(k) = S(k)\left|\sqrt{R_r\gamma_r} + \sqrt{R_s}\int a_s(z)e^{-ikz}dz\right|^2,$$

Equation 3

where $I(k)$ denotes the detected spectrum; $S(k)$, the power spectrum of the light source; γ_r , the amplitude reflectivity of the reference arm and $a_s(z)$, the axial profile of the amplitude backscattering coefficient of the sample. R_r and R_s denote the total power splitting ratios of the reference beam and the sample beam from the light source to the detection arm. The phase term e^{-ikz} denotes the phase offset due to the optical path length difference between the reference beam and the backscattered beam. The fringes in the spectrum are converted to the k-space and its Fourier transformation yields a one-dimensional back scattered intensity versus depth profile from which the image is reconstructed. In a spectral detection, the sensitivity S is given by

$$S = \frac{\eta P T_{exp}}{(h\nu)},$$

Equation 4

where P is the source power, T_{exp} is the exposure time, η is the detection efficiency, and $h\nu$ is the photon energy. With spectral detection, the exposure time is approximately the axial scan time T_{Ascan}; therefore $T_{Ascan} \approx T_{exp}$. In conventional OCT, light from different time delays is detected sequentially, so assuming an axial scan time of T_{Ascan}, the exposure time is approximately T_{Ascan}/M, where M is the number of resolvable elements in one axial scan, defined as the total axial measurement range divided by the axial resolution. Therefore, spectral domain detection has a sensitivity advantage proportional to the number of resolvable elements in an axial scan. This sensitivity advantage is typically ~30 dB, enabling shorter exposure times which dramatically increase imaging speeds. With shorter exposure times, spectral domain OCT is less sensitive to subject motion than conventional time domain OCT [25-27].

1.2.3 Swept source OCT (SSOCT)

A typical SSOCT uses a swept-laser source, an interferometer and signal processing tools. As described previously, OCT imaging requires a low coherence light with a high bandwidth, and the coherence length controls the imaging depth. To obtain higher imaging depths, high-coherence light is required which reduces the axial resolution. So, there is a trade-off between the resolution and the imaging depth in conventional OCT. With the swept-laser source, the broadband laser is chirped into a very narrow line width of 0.1 nm pulses, and the pulses are swept at rates of MHz.

Each narrow pulse has a long coherence length, and all the pulses together form a broadband laser source (up to 170 nm) of a high coherence length thus allowing for a deeper imaging depth and high-depth resolution. In addition, at any given time, laser light would be interrogating the entire depth simultaneously and, because of narrow line width, even the reflections from deeper depths (~6 mm) have the ability to cause interference. The laser output is sent to a fiber based interferometer. Just like in TDOCT and SDOCT, the light from the sample arm and the reference arm are coupled in a 50-50 fiber coupler where the interference fringes are formed. These fringes are typically detected by a dual-balanced high-speed detector. In the dual-balanced detection

mode, the common noise coming from each arm is cancelled, and the out-of-phase interference fringes are added and amplified by a low-noise high-gain trans-impedance amplifier. Because of this amplifier, the electronic noise is suppressed. An ADC card digitizes the photocurrent output of the detector.

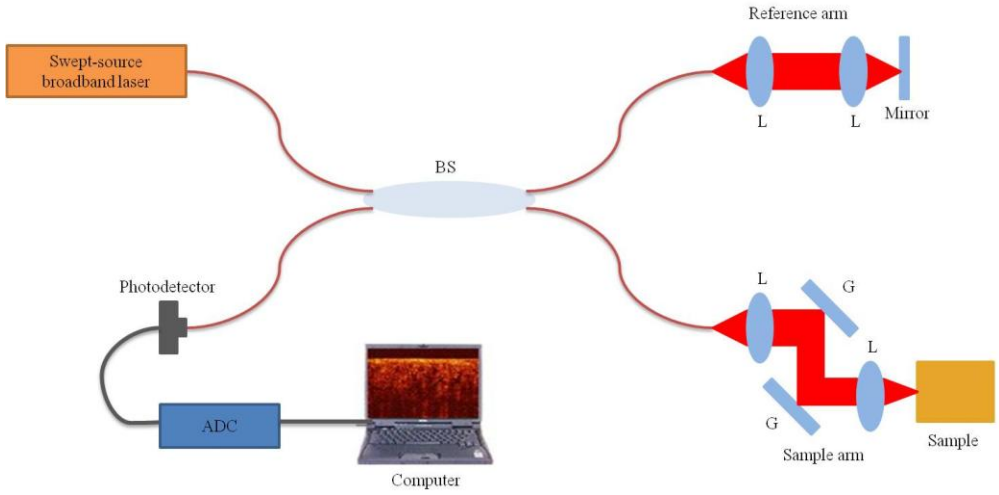

Figure 4: The Schematic of a SSOCT.

The sample points of this photocurrent are not equally spaced as the laser is swept non-linearly with frequency. There are many different techniques to correct this non-linear sweep. The easiest way is to sample the detector signal in non-linear time intervals to compensate for the frequency chirping of the source [28].Alternatively, the existing chirped signal can be numerically mapped to a uniform *k*-space using interpolation [29-33]. Although both methods were previously demonstrated to yield a transform-limited axial resolution, the former one needs complex algorithms to be computed, and the later one is not dynamic calibration. The most popular way of correcting the non-linear sweep is by using MZI-OC. Each of the above techniques has its own advantages and limitations. Details of SSOCT are described in Chapter II.

1.3 Phase resolved OCT

Techniques based on phase information in the field of imaging have been in practice from the mid 1950's. In early studies, phase information from microscopic samples was utilized for live visualization of cells. Phase contrast microscopy is one example in which phase information from microscopic images has been utilized to qualitatively visualize small, subcellular variations in the refractive index. The sensitivity of detection of refractive index variations depends upon the accuracy in the retrieval of phase information.

Phase resolved OCT is a technique that allows retrieving optical phase in low coherence interferometry and quantification of variations in refractive index. Phase resolved OCT can be implemented in various forms such as Doppler OCT, phase variance and contrast. All forms of phase resolved OCT has been applied in various fields such as cell biology, angiography, and elastography. In cell biology, phase resolved OCT has been applied to characterize cardiomyocyte contractility, characterizing cytoplasmic flow in individual cells, characterizing mechanical properties of the cytoskeleton and whole cell imaging. Therefore, even though OCT cannot achieve sub-cellular resolution in imaging, phase resolved imaging allows sub-cellular analysis. Similarly, phase resolved OCT is extensively used in detecting blood flow [34]. For example, Vakoc et al., have used phase resolved optical Fourier domain imaging (OFDI) to detect blood flow in capillaries. Similarly Baumann *et al*., have developed Doppler OCT to detect blood flow in ocular tissues [35].

As described earlier, the sensitivity of the measurements depends on the phase stability of the system. Phase stability of the system depends mainly on the presence of mechanical moving parts in the system. In the case of the swept source OCT, the laser is swept using a mechanical mirror whereas in the case of SDOCT, there are no moving parts and therefore spectral domain (SDOCT) has better phase stability. Due to the above reason, most of the phase resolved

techniques were implemented using SDOCT; most commonly known as spectral domain phase microscopy (SDPM). SDPM offers measurements of displacements with picometer to nanometer scale sensitivities [36]. However, until recently, SDOCT was implemented in the wavelength range of 800 nm due to the unavailability of high speed InGaAs cameras required to detect 1300 nm. In order to take the advantage of longer wavelengths that allow deeper penetration, phase resolved techniques have been implemented in swept source OCT as well. However, the phase stability offered by SSOCT is much lower compared to SDOCT mainly due to the instabilities in the swept laser source. Therefore, to enhance the measurement sensitivities in SSOCT, phase stabilized techniques were performed prior to imaging. For example, Vakoc et al., have utilized an extra arm in the interferometer to collect the phase noise, from which the phase was calibrated, which improved the detection sensitivities by ten-fold. In this dissertation, phase stabilization techniques were implemented to improve the phase stability by 40 times and phase resolved measurements were performed using SSOCT.

II. CHAPTER 2. SYSTEM DEVELOPMENT

This chapter is dedicated to the description of Phase Stabilized Swept Source OCT (PhS-SSOCT) system development. The first section of this chapter describes instrumentation and functioning of individual components that were essential for developing PhS-SSOCT. The second section deals with the image reconstruction algorithms and signal processing techniques that have been adapted to improve the quality of images. The final section deals with the description of final characteristics of the developed system.

2.1 PhS-SSOCT design and operation

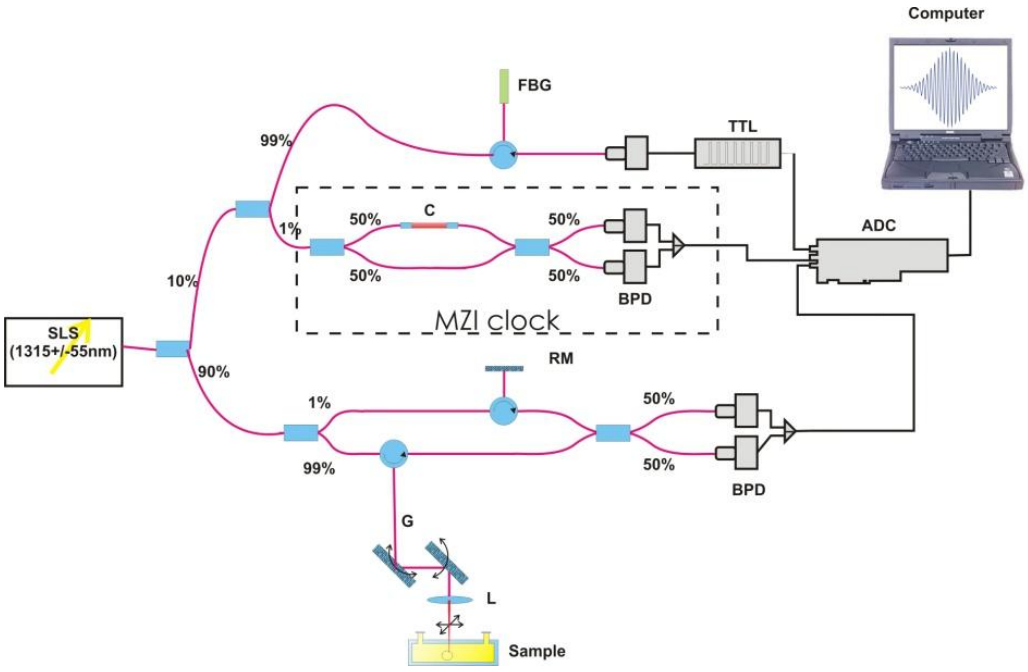

Figure 5: The schematic outline of PhS-SSOCT (ADC: Analog to Digital Converter, BPD: Balanced Photo Detector, C: Collimators, FBG: Fiber Bragg Grating, G: Galvanometer Scanner, L: Lens, RM: Reflective Mirrors, SLS: Swept Laser Source, TTL: TTL Signal Generator).

The schematic outline of the developed PhS-SSOCT system is shown in Figure 5. The system consists of four main units: the source, interferometer (Mach-Zehnder in this particular setup), the calibration system, and data acquisition electronics. The laser source output is split into two arms by a 90/10 fiber splitter (FC1310-70-90-APC, Thorlabs). The first arm (90% of the light) is used to construct the interferometer while the second arm is further split by a 99-1 fiber splitter with 99% going to a fiber Bragg grating (FBG) for triggering and 1% to the Mach-Zehnder Interferometer based optical clock (MZI-OC) for calibration (these described in detail in the next sections of this chapter).

The light going to the FBG is directed through a three-arm circulator and the reflected pulse is received by a detector. The detector outputs a voltage signal which is converted to an electrically tunable TTL pulse by a pulse generator (Stanford Research Systems, Inc.). The TTL signal is tuned to a required duty cycle and connected to the analog to the digital converter's (ADC) external trigger channel. The other 1% is fed to the MZI -OC whose signal is detected in balanced detection mode, and these electric signals from the detector are acquired by one of the channels of the ADC. In the interferometer arm, the 90% light is further split into another 10% and 90%, each going to the reference arm and sample arm, respectively, via circulators. The light coming from the reference arm is passed through an adjustable pin hole to allow control of attenuation as required. The reflected light from the reference arm and sample arm are coupled into a 50-50 fiber coupler where they recombine and form the interference fringes.

These fringes are then detected by a balanced photo detector (BPD), which subtracts the two signals to remove the common mode noise. As the fringes would be out of phase, this BPD is effectively adding the fringes but subtracting the common mode noise. After removing the common mode noise, the fringe encoded voltage is then amplified by a Transimpedance amplifier (TIA) and then RF modulated and acquired by a PC through the other channel of the ADC. Both the information from the MZI-OC and the interferometer is acquired simultaneously by the ADC

with the receiving of the trigger from the FBG. Fringes from the MZI-OC are utilized for calibrating the fringes obtained from the interferometer. These calibrated fringes are passed through image reconstruction algorithms to obtain 2D and 3D images. Therefore, image quality depends on the components responsible for generating both MZI-OC and interferometer fringes. Hence, it is important to understand the major components of the system in detail. The next section deals with the description and testing of each component.

2.1.1 Description of components

2.1.1.a Laser source

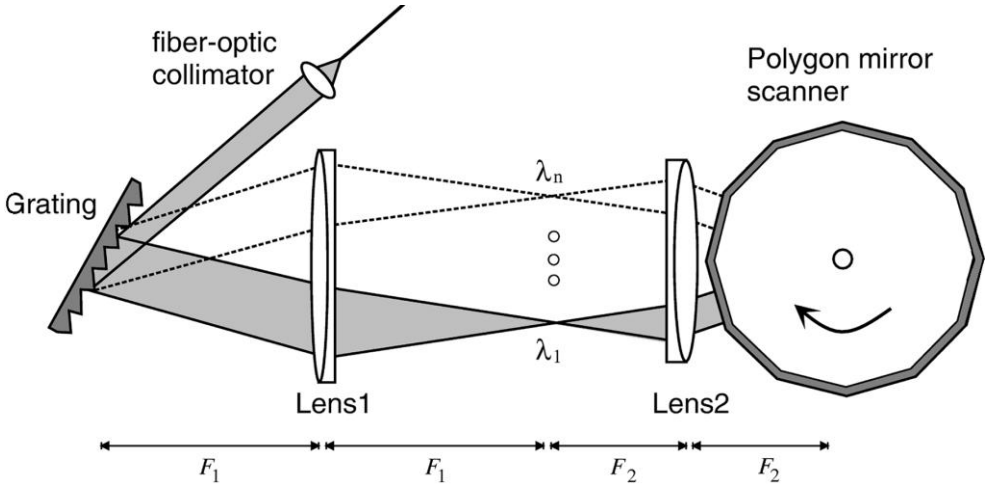

Figure 6: Schematic of a polygon scanner based wavelength tuning laser, F1 and F2 are focal lengths of Lens1 and Lens2, respectively, λ1-λn spectrally decomposed wavelengths from the grating (adopted from [37]).

The laser source used for the development of PhS-SSOCT system was purchased from Santec, Inc. (HSL-2000, Santec Inc., Japan). A typical high-speed scanning laser consists of a wavelength scanning filter based on a polygon scanner, diffraction grating and a telescope with two lenses in an infinite-conjugate configuration [31] (Figure 6). The light coming out from the

grating that has all the wavelengths within the scan range falls on the polygon mirror. At a particular instant of time, only a single frequency light can be focused perpendicular to the polygon mirror. The narrow-band light that is normal to the front facet of the polygon mirror reflects back into the telescope configuration and is selected by the filter. The polygon mirror is rotated to accomplish the wavelength scan.

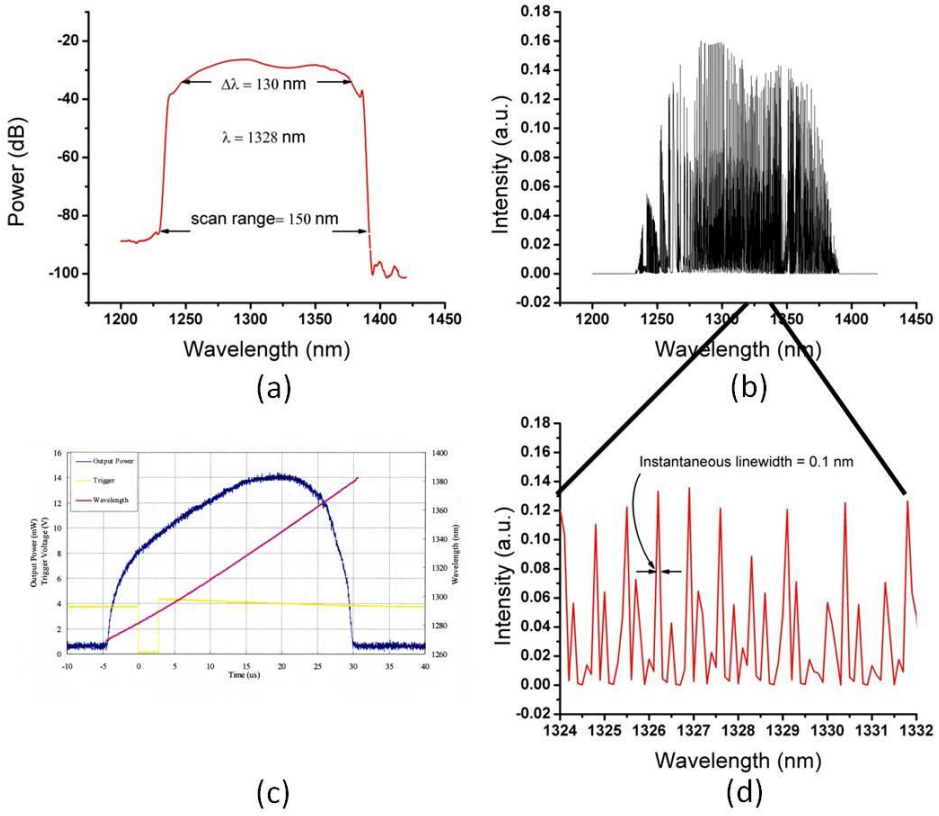

Figure 7: Power spectrum of the laser source in peak mode is shown in (a) dB scale and instantaneous power spectrum in (b) and (d), wavelength sweep function with time in (c).

Figure 7 (a) shows the output spectrum of the HSL-2000 high-speed scanning laser measured with an optical spectrum analyzer with a resolution of 0.1 nm in peak-hold mode where the peak value is always held constant. The output spectrum spans from 1240 nm to 1390 nm over a range

of 150 nm, with a maximum output power of 48 mW at a central wavelength λ_0 = 1328 nm. The spectrum has a profile with FWHM $\Delta\lambda$ = 130 nm and predicts the axial resolution of 5.7 μm.

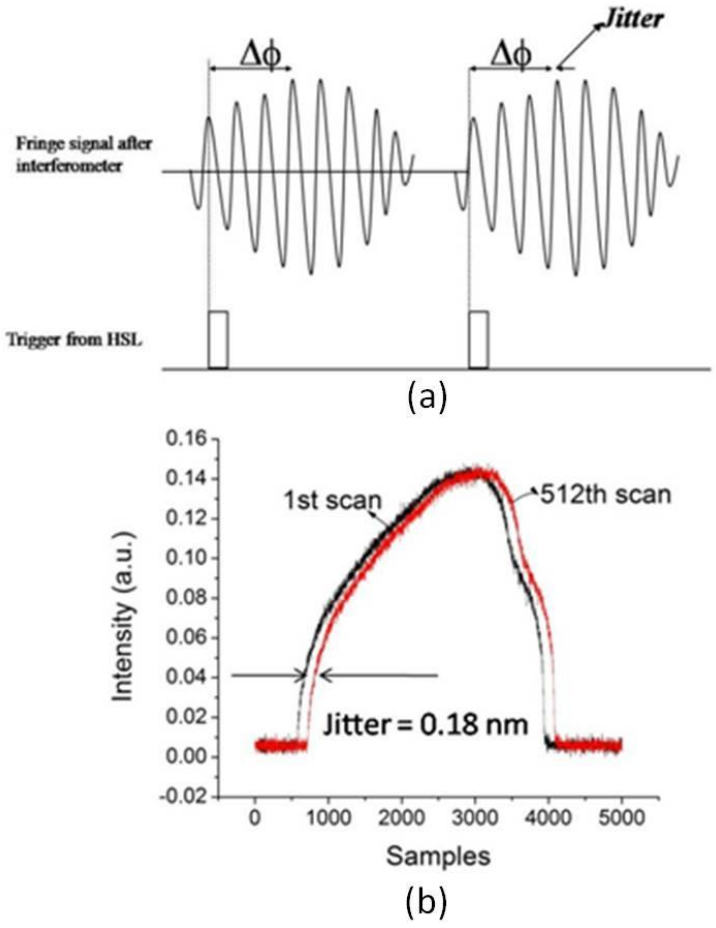

Figure 8: (a) Definition of jitter (b) jitter recorded between the first and the 512th laser sweep.

The instantaneous line width (0.1 nm) is measured from the output spectrum obtained from the spectrum analyzer in continuous mode as shown in Figure 7 (d) which shows that the wavelengths are not scanned at regular intervals of wavelength. Wavelength sweep over time is shown in Figure 7 (c). These figures suggest that the laser emits wavelengths in non-uniform intervals of time. Therefore, the intensities of the laser scan non-uniformly in the wavelength

space. Since k-vector is defined by wavelength ($k = 2\pi/\lambda$), the laser intensities are scanned non-uniformly in *k*-space as well. Since the application of fast Fourier transform required the sampling space to be uniform; remapping this k-vector to a uniform k-space is required to correct the non-linearity. Details of the non-linearity correction are dealt with in a later section 2.1.1.e.

The other important characteristic of a laser is the drift of the laser spectrum in time (jitter) after a certain number of scans as shown in Figure 8. Figure 8 (b) demonstrates that the jitter measured between the 1st and 512th scans is 0.18 nm. To account for this, we have utilized FBG with linewidth of 0.1 nm as described in the section 2.1.1.c.

2.1.1.b Balanced photo detector (BPD)

The detector used for detecting the interference fringes for the PhS-SSOCT is a Balanced Amplified Photo Detector (PDB130C Series, Thorlabs). This detector consists of two well-matched photodiodes and an ultra-low noise; high-speed transimpedance amplifier (TIA) with a gain of 10^4 V/A that generates an output voltage proportional to the difference between the photocurrents in the two photodiodes. This dual-balanced detection reduced the source's relative intensity noise (RIN) and autocorrelation noise of the detector. The fringes from each of the arms are detected out of phase, and on subtraction, the common noise would be subtracted whereas the fringes are added as they are out of phase and amplified by the TIA. Thus, the common noise is also reduced. The common noise rejection efficiency of the receiver is approximately 35 dB in the range of DC-350 MHz. In addition to the RIN and common noise, the RF modulation after balanced detection also provides benefits like suppressing the self-interference noise, originating from the multiple reflections within the sample and optical components as well as increasing dynamic range.

2.1.1.c Fiber Bragg grating (FBG)

Generally, the wavelength scan is very consistent from scan-to-scan in the employed swept-source laser. However, there was a jitter on output trigger (up to ~0.18 nm) due to noise in the electronics and slow drift over time, as shown earlier in Figure 8. Therefore, the delay between the trigger signal and the subsequent ADC conversion varied resulting in phase jumps up to a maximum value of π. These phase jumps would severely degrade the phase stability of the system and, therefore, the sensitivity of phase measurements. To remove this delay between data acquisition and laser sweeping, PhS-SSOCT makes use of FBG for the accurate triggering of ADC for data acquisition [23]. Triggering with FBG significantly reduced source/acquisition timing variations and significantly increased the accuracy of the system for the phase-resolved measurements. Detailed description of how this correction was achieved as follows:

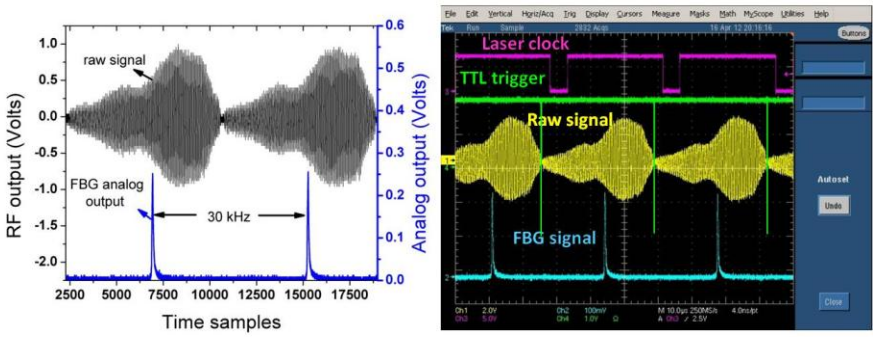

Figure 9: FBG output (a) analog output and the raw signal (b) Image showing the synchronization of FBG trigger, raw signal and MZI-OC signal.

An optical pulse is detected by the detector every time the laser swept 1328 nm (the reflection wavelength of FBG as well as the central wavelength of the laser), thus the frequency of the FBG pulses are also at 30 kHz as shown in Figure 9 (a). Moreover, the FBG signal jitters along with

the laser's sweep and therefore, the TTL signal formed from the FBG signal compensates for the delay. Figure 9 (b) depicts the oscilloscope trace showing the TTL trigger signal (green trace), the signal from the sample (yellow trace) and the FBG signal (blue trace). We can see that the TTL signal is occurred in perfect synchronization with the raw signal.

Before the correction, the mismatch in fringe signal and the trigger would result in phase jumps of up to a maximum value of π as shown in Figure 10 (a). The correction reduced the phase variations and the phase stability was improved up to 40 times (standard deviation of 0.016 radians for 512 A-line scans) as shown in Figure 10 (b).

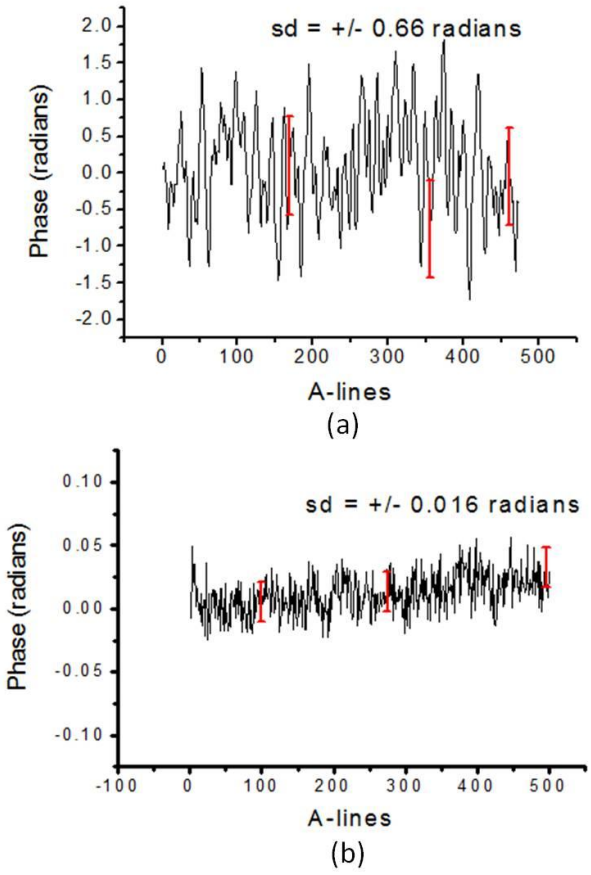

Figure 10: The temporal phase response of 500 µm cuvette at 500 µm depth (a) before stabilization (b) after stabilization (Note the scale).

With the stabilized phase, the refractive index change as small as 6.3 x 10^{-6} (in a 1 mm thick sample) can be detected using the PhS-SSOCT.

2.1.1.d Data acquisition card

A high-speed digitizer, analog-to-digital converter (ADC) from AlazarTech (ATS9350) has been used to acquire the detector current. The detector current can be digitized at a sampling rate of 500 MS/s with 12-bit encoding. It has two channels that can be triggered simultaneously using an external trigger or a digital clock or even internally using software. In the PhS-SSOCT, it is digitized externally using the TTL signal generated from the FBG reflected optical pulse as discussed earlier. The data from the digitizer was recorded in a high speed computer with eight processors and 6 GB memory and the data flow was passed into queues such that all eight processors are utilized while executing the program.

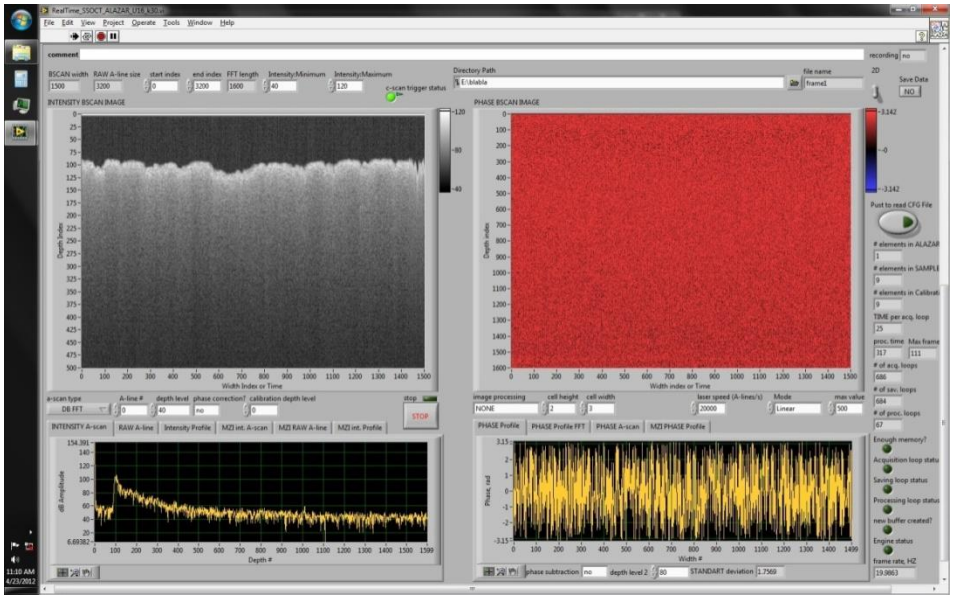

Figure 11: User interface of PhS-SSOCT controlling software showing the real time monitoring of images, intensity and phase profiles.

LabVIEW 9 (National Instruments) interface was utilized to achieve the data acquisition. The program was developed in such a way that it was user friendly; one can choose the sampling rate, number of samples, control for 2-D and 3-D scanning and select the required algorithm for the recalibration and remapping to uniform k-space. Direct monitoring of the real time images, their A-line profiles as well as the phase responses can be visualized from the front panel of the program as shown in Figure 11.

The program also supports real time recording of raw data of both the MZI-OC signal and the sample signal, calibrated sample data and image data. One can generate images using offline calibration of the raw sample data using MZI-OC data, thus enabling flexibility to analyze the fringe signal in its raw as well as calibrated formats.

2.1.1.e Mach Zehnder interferometer-based optical clock (MZI-OC)

In SSOCT systems utilizing broadband laser-swept sources, the optical frequency is not sampled uniformly as discussed earlier. Since the in-depth information in PhS-SSOCT is in the optical time-delay domain, Fourier transform is required to obtain images of objects under study. In general, widely used Fast Fourier Transform (FFT) algorithms are performed using a uniform sampling interval. The non-linearity in the laser introduces non-uniformity in the sampling in wavelength domain.

In order to correct for this non-linearity, we utilized the MZI-based approach where fringes formed in MZI are equally spaced in frequency. For this, 10% of the output source is split into 1% and 99%, where 1% light is directed to the MZI-OC, which generates an equally-spaced frequency interferogram (with optical frequency spacing adjustable range: 12.5 GHz - 200 GHz). The interferogram obtained from MZI–OC has all peaks, as well as the zero crossings equally spaced in optical frequency space and so they can be used for recalibrating the interference signals coming from the main interferometer. Hereafter, the signal that is to be calibrated

(interference signal formed by the sample and reference) is referred to as the raw signal, and the signal which is calibrated using MZI-OC is referred to as the calibrated signal.

This MZI-OC interferogram was recorded via a separate channel in the data acquisition card, and standard procedure of PhS-SSOCT data re-mapping was performed in the frequency-domain before the application of FFT. Using a high-speed nearest-neighbor check algorithm, indices corresponding to the peaks and zeros of the MZI-OC signals are recorded, and the intensity values of the raw signal corresponding to these indices are obtained. Since the number of samples with peaks and zeros is always less than the total number of points, the obtained values are interpolated to get a standard number of samples (2048) in order to overcome the problem of under sampling. This remapping procedure using MZI-OC eliminated errors associated with non-uniform sampling intervals.

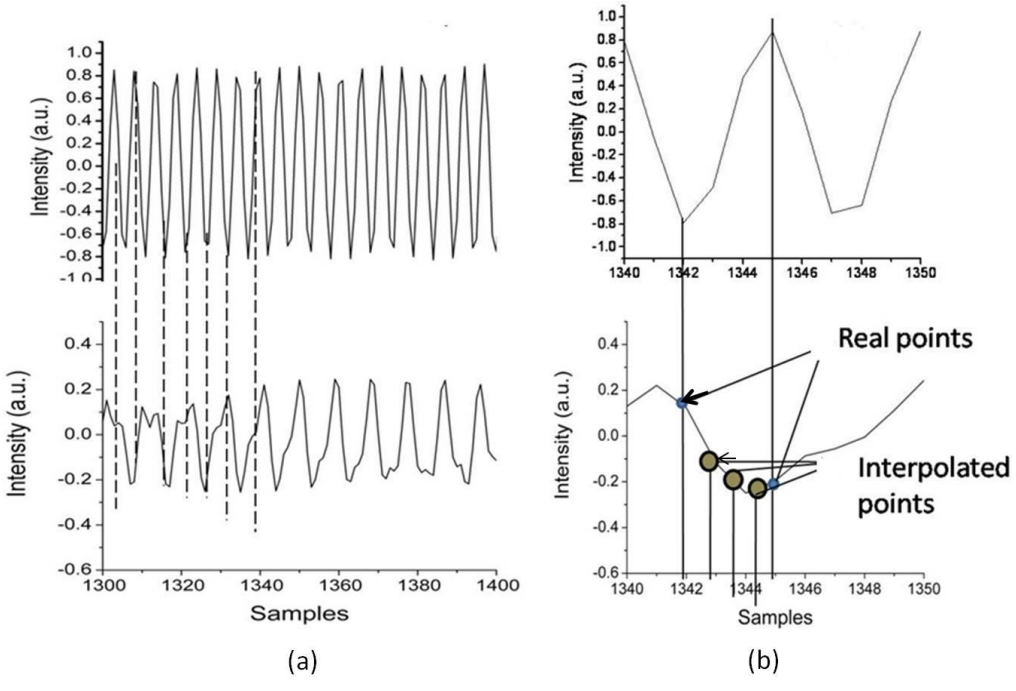

Figure 12: Recalibration process (a) detection of peaks in MZI-OC and resampling of raw data (b) interpolation.

The fringes are acquired by the 12- bit high-speed digitizer. The digitizer is operated at 180 MS/s and the laser scans every 33 μs. Therefore, 6000 sample points per A-scan were acquired for both the raw signal and the MZI-OC signal. The sampling rate is chosen by considering the fact that the sampling interval in the wavelength should be smaller than the instantaneous line-width; otherwise, a large sensitivity drop off along the depth scan would be observed. For example, with 180 MS/s sampling rate, the 170 nm bandwidth is spanned over 6000 points. Therefore, each point corresponds to ~0.02 nm which is less than the instantaneous linewidth (0.1 nm).

The recalibration using MZI-OC, which is required to correct the non-linearity in the laser sweep, involves three steps; detect the peaks and zeros, acquire the raw data corresponding to the sample points where the MZI-OC peaks and zeros are present (resampling), and then interpolate, if required, to have 1600 points. The nearest neighbor check algorithm is used to detect the peaks and zeros, the number of peaks and zeros registered was at least 3200 for a total acquisition of 6000 MZI-OC signal points. The raw signal was resampled with the MZI-OC's zero crossings and peak indices as shown in the Figure 12. As, these points are equally spaced in frequency, the resampled signal from the raw data now has points that are equally spaced in frequency. But the resampled signal has 3200 points where the acquired raw signal has 6000 points. To overcome this under sampling problem, intensity values can be interpolated for three equidistant sample points using spline interpolation thus having 6000 sample points.

However, interpolation reduces the real time imaging speed. Any presence of interpolation errors introduces side lobes in the Fourier transform. Moreover, the loss in signal information due to under sampling was too low that we traded it off for the imaging speed. Therefore, no interpolation was performed for *in vivo* studies where real time imaging speed was critical.

Figure 13 shows the signal from the sample before calibrating to uniform k-space and after calibration. Chirping of the signal could be noticed in the signal before calibration that was corrected by recalibrating the signal to uniform k-space. So, the laser chirp frequencies are not reflected in the depth profile any more, thus removing the resolution degradation along *z.*

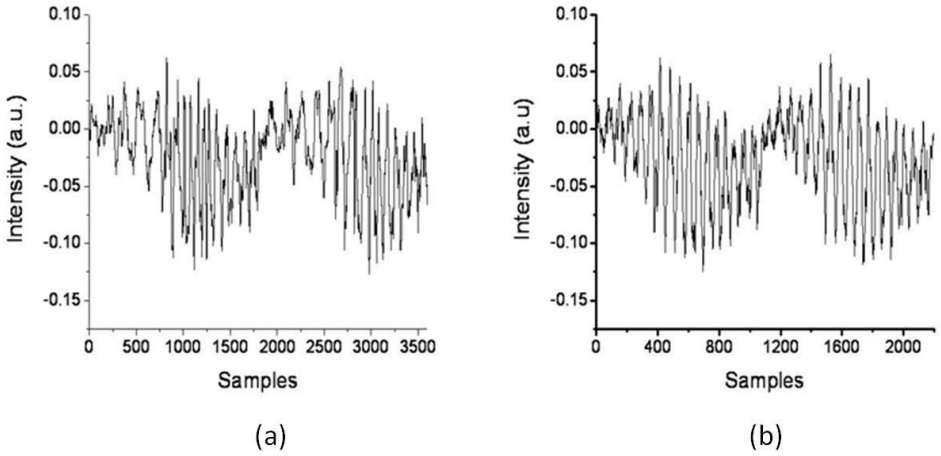

Figure 13: The raw signal (a) before calibration (chirped) (b) after calibration (uniform frequencies).

2.1.1.f Galvanometer-mounted scanning mirror

To obtain 2-D and 3-D images, a two-axis galvanometer scanning mirror is utilized. The galvanometer scanner has two mirrors mounted on a galvanometer-driven motor at 45^0 to each other. Scanning these mirrors is controlled by the LabVIEW program described earlier, and a multi-function DAQ card (National Instruments, PCI 6731) is used to generate analog voltage signals to drive the galvanometer motors. The DAQ card has two output voltage channels, thus enabling control for both the mirrors.

Each depth profile is obtained from the Fourier transform of the interference fringe signal as described above. The logarithm of the absolute value of this complex FFT is mapped to the gray scale intensity values to get an image of a single A-scan. By generating a transversal set of similar

1-D depth profiles with the scanning galvanometer-mounted mirrors, 2-D and 3D images are constructed. Thus, these images contain both axial and transverse information. Data is acquired during 80% of the B-scan and saved in to a local buffer and the rest of the time is allowed for clearing the buffer. With this procedure, the system achieved a real time speed of 40 frames per second with a frame size of 1600X 500 pixels.

2.2 Signal processing

Signal processing includes several steps such as reference subtraction, windowing, and image construction.

2.2.1 Background subtraction

The background signal is recorded at the beginning of every acquisition by blocking light in the sample arm. This signal contains the 10% residual light reflected from the reference arm and from the residual signal in the detectors due to imperfect symmetry of the BPD. Subtracting the reference from the interference signal helps to increase the contrast and remove the artifacts. Subtraction also removes the low-frequency components introduced by the reference or ambient light.

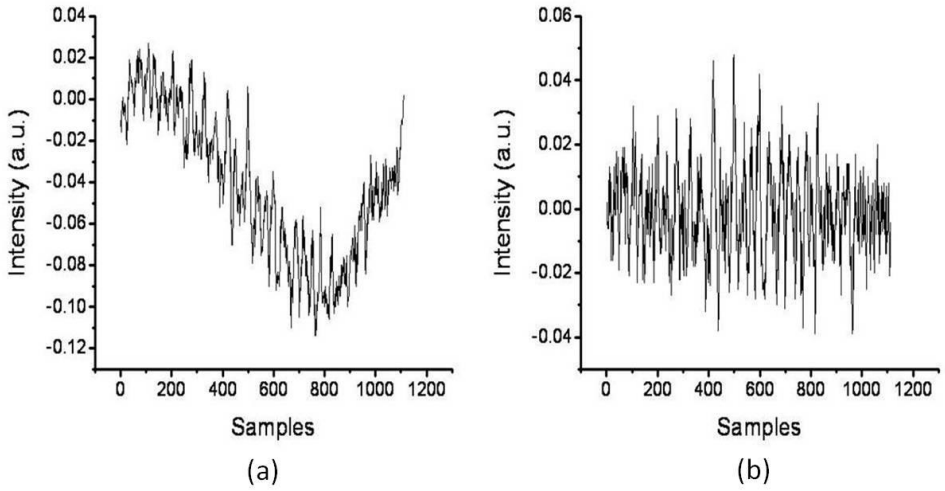

Figure 14: The calibrated signal from the sample (a) before subtraction of the reference power (background) (b) after reference subtraction (enhanced contrast).

Figure 14(a) shows the raw signal from the sample and Figure 14(b) after subtracting the reference signal from the sample signal. The reference subtracted fringe signal shows many zero crossings which increase the contrast in the image. These signals are then passed through a Gaussian window after normalization to get a perfect Gaussian-like peak at that frequency/depth in the 1-D profile.

2.2.2 Windowing

Frequency response of the MZI-OC signal is shown in Figure 15 which helps to choose the frequency filter and the required interference time domain signal that effectively increase the SNR. By selecting the sample numbers corresponding to B_1 and B_2 in Figure 15, only the ON time of the laser is selected. A_1 and A_2 select the cut-off frequency and the highest frequency for windowing in the frequency response of the sample.

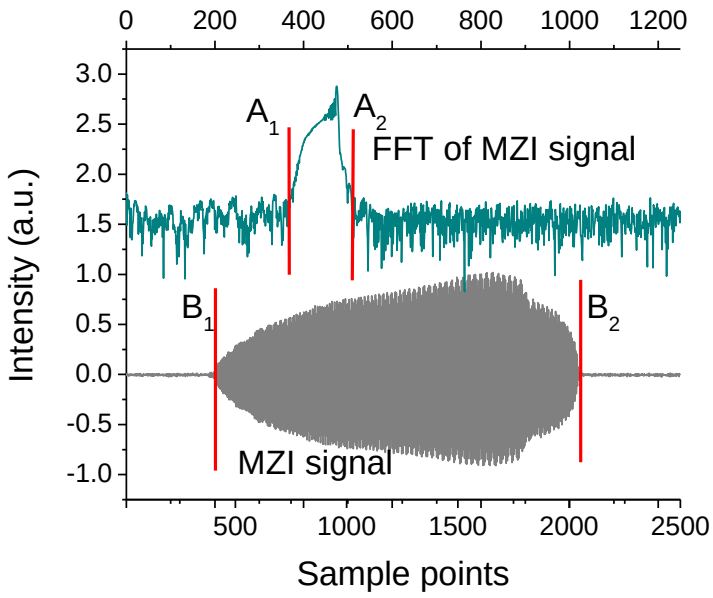

Figure 15: MZI-OC signal and its frequency response, A1, A2 are the lower and higher cut offs of frequency filter, B1, B2 are the time window that selects only ON time of the laser.

However, this procedure is followed only when offline images are required to be generated as in the case of real time imaging, no MZI is utilized for *k*-space calibration.

2.3 Characterization of the system

The most important parameters of OCT are the depth and transverse resolution, signal to noise ratio (SNR), imaging depth, and speed of imaging. Each of these parameters were calculated theoretically and compared with the experimental values.

The depth or axial resolution could be calculated as [38]

$$\Delta z = \frac{2ln2\ \lambda^2}{\pi\Delta\lambda},$$

Equation 5

where λ is the central wavelength and $\Delta\lambda$ is the bandwidth. $\lambda^2/\Delta\lambda$ give the coherence length of the laser source.

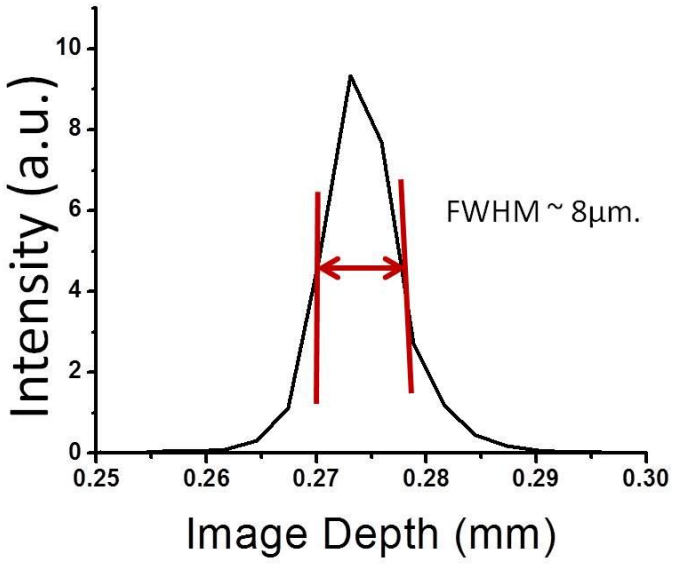

Figure 16: Resolution calculated by FWHM drop of the PSF.

Equation 1.6 indicates that lower wavelengths and broader bandwidths will yield higher resolutions. The laser used in this dissertation has a wavelength of 1328 nm and a bandwidth of 150 nm, the theoretical resolution obtained would be 5.9 µm. The resolution has been verified with two different methods. The first method was by calculating the distance corresponding to the FWHM drop in the point spread function (measured in linear scale) as shown in Figure 16.

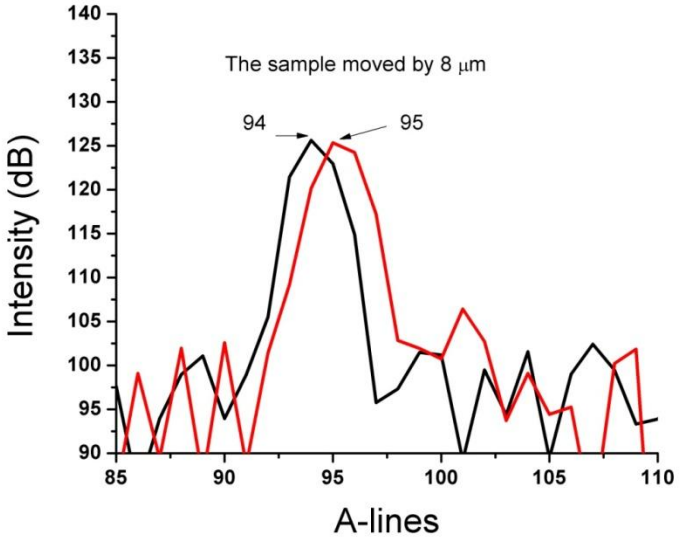

Figure 17: Change in the PSF with a movement of 8 μm in the sample arm.

The other method was by shifting the sample arm by 8 μm to see if there is a change in the peak position at 3 dB drop as shown in the Figure 17; there is a peak shift by 1 index for change of 8 μm in the sample distance. Therefore the measured resolution is 8 μm which is 2.1 μm higher than the theoretical resolution. The main reason for not achieving the theoretical resolution is mainly due to the roughness in the spectrum [39]. The roughness in the spectrum leads to the roughness in the fringes which in turn induces side lobes in the point spread function, therefore degrading the resolution. Similarly, the roughness in the spectrum is an attribute of spectral noise. Other factors that affect the resolution is dispersion. As the laser light passes through the optical fiber and other optics, the laser source is dispersed and leads to degradation of the resolution. In order to achieve resolution closer to the theoretical value, spectrum reshaping, noise reduction and dispersion compensation techniques can be implemented. Spectral reshaping techniques such as the apodization of spectrum and digital dispersion compensation techniques increase the real-time imaging speed and therefore, they were not implemented in this dissertation. However,

dispersion due to the scanning lens was compensated by incorporating a dispersion compensation lens at the sample arm.

Transverse resolution is the ability to resolve two points on the surface or the transverse direction. Thus, the transverse resolution depends upon the beam spot size falling onto the sample. The transverse resolution Δx is calculated using [38]

$$\Delta x = 1.22 \times \frac{\lambda}{1.4 \times N.A.},$$

Equation 6

where *N.A.* is the Numerical Aperture at the lens that can be calculated as

$$N.A. = n \times \sin\tan^{-1}\frac{w}{2f},$$

Equation 7

where *n* is the refractive index of the medium where the sample is placed, *w* is the beam diameter, and *f* is the focal length of the lens. Thus, a high *N.A.* producing lens gives better transverse resolution, but from Equation 7, high *N.A.* can be obtained by having higher beam diameters. For most handheld devices, the galvanometer mounted mirror size limits the freedom of having very large beam diameters (~7 mm). For a 4 mm beam diameter with a wavelength of 1328 nm, and a lens with a focal length of 2.54 cm, obtained transverse resolution is 14.4 μm and the experimentally measured value is 15.6 μm as seen in the Figure 18.

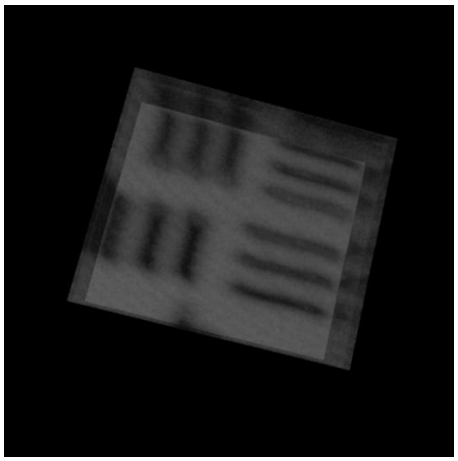

Figure 18: 3D image of the Air Force resolution target showing the gap between the lines to be 15.6 µm.

The signal to noise ratio of the SS-OCT is given by

$$SNR = 10\log\left(\frac{\acute{\eta}P}{2\frac{hc}{\lambda}NEB}\right),$$

Equation 8

where, $\acute{\eta}$ – is the quantum efficiency of the detector, P is the input power, hc/λ is the photon energy and *NEB* is the noise equivalent bandwidth of the filter and is defined as a geometric measure of how much noise passes through the filter. For the detector, the quantum efficiency is given by [33]

$$\acute{\eta} = (\frac{P \times 1240}{\lambda}) \times 100.$$

Equation 9

Therefore, $\acute{\eta}$ = 93% and *NEB* = 75 MHz and substituting laser power P = 30 mW at 1328 nm central wavelength in the equation, the *SNR* obtained would be 107.31 dB for a perfect reflector. To test SNR experimentally we used a 0.22 mm micro slide that has a 60 dB reflectivity (the

measurements are taken in the inter-interference mode). The power spectrum function (PSF) at various depths for the micro slide were acquired and checked if the resolution was maintained over the distance. Figure 20 (a) and (b) shows that with the increase in the depth, there was neither peak broadening nor degradation in the resolution. The Figure 20 also shows that the maximum imaging depth obtained was around 6 mm. The signal to noise ratio (SNR) was calculated using the formula given in the equation,

$$SNR = 20log_{10}\frac{max.intensity}{SD\ of\ the\ noise}.$$

Equation 10

The SD of the noise obtained was around 23728.56 in linear scale and the peak value = 3306095.56. Plugging these values in the above equation, the SNR obtained was 45 dB. As we were utilizing a 60 dB attenuated glass slide, the actual SNR was 45 + 60 = 105 dB.

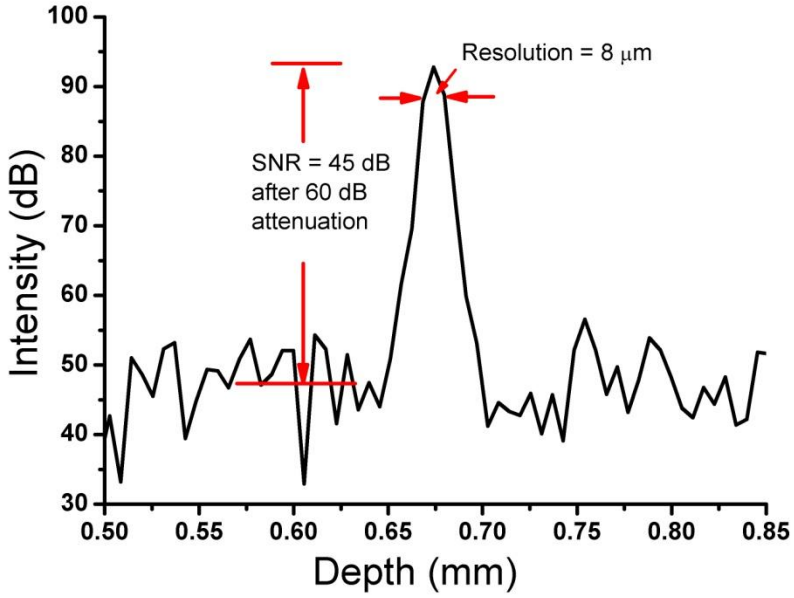

Figure 19: SNR and Resolution.

One of the inherent drawbacks of using Fourier domain OCT is that the sensitivity drop-off with respect to the depth is very high. Figure 20 (b) clearly demonstrates this effect as signal amplitude decreased for about 20 dB over 6 mm depth. However, this drop is very less compared to the SDOCT systems (20 dB over 3 mm depth) which are one of the advantages of SSOCT over SDOCT.

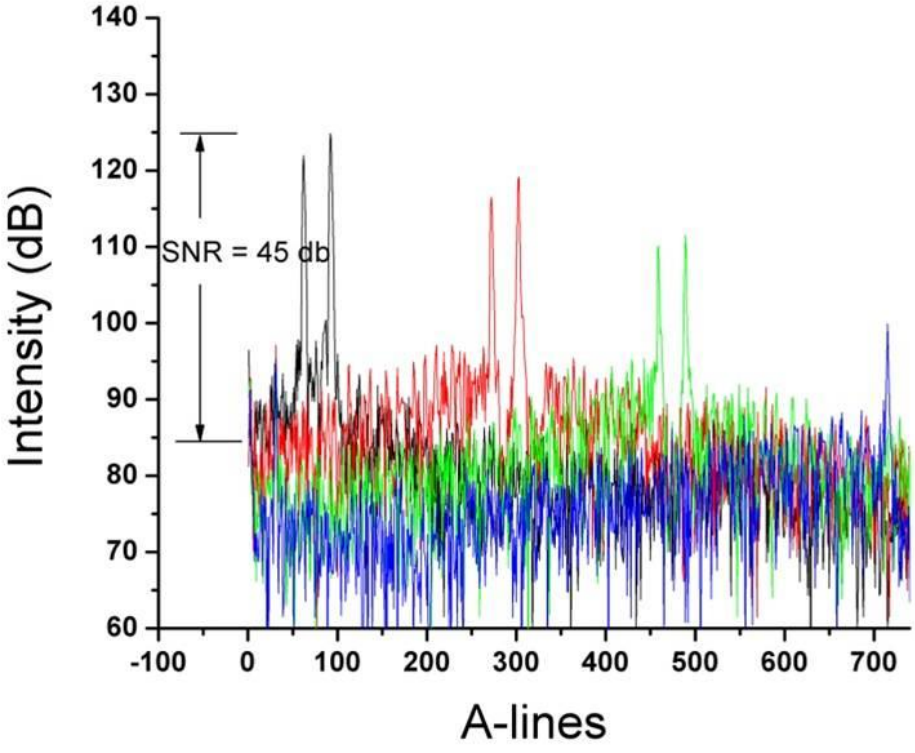

Figure 20: The PSF's at different depths indicating the maximum depth and the SNR.

To summarize, the developed system showed an axial resolution of 8 μm, transverse resolution of 16 μm, SNR of 105 dB, imaging depth of 6 mm, imaging speed of 40 fps with 1600 X 500 pixels of frame size, and a phase stability of 0.01 radians [40, 41].

III. CHAPTER 3. IMAGING OF MICROBUBBLES

This dissertation introduced a new phase-resolved system that allows comprehensive imaging of biological systems *in vivo*. In this chapter, the application of PhS-SSOCT for detecting microbubbles in clear media, scattering media, blood *ex vivo* and mice tails *in vivo* will be discussed.

3.1 Motivation

Formation of microbubbles in the human body has been extensively studied by many researchers since the discovery of Caisson disease by Paul Bert in 1878. In its classic and most severe form, gas emboli present catastrophically (~4% of victims) with collapse, loss of consciousness, apnea, and cardiac arrest. Formation of microbubbles inside the body could be attributed due to different physiological, physical, and intervention mechanisms. These bubbles can travel to any part of the body, accounting for many serious (and sometimes life-threatening) disorders [42]. Gas bubbles in the back or joints can cause localized pain (the bends). In the spinal cord or peripheral nerve tissues, bubbles may cause paresthesias, neurapraxia, or paralysis. A bubble forming in the circulatory system can lead to pulmonary or cerebral gas emboli. Formation and/or introduction of gas microbubbles in human blood and tissues remains a serious long-term sequel in patients undergoing cardiac valve replacement (with an annual risk of up to 4%) [43-45]; high-intensity focused US therapy [46-48]; cesarean section and operative hysteroscopy [30, 49-60]; cardiopulmonary bypass and other open-heart surgeries [44, 45, 61-64]; orthopedic surgery [65, 66]; and various laser ablation and laparoscopic surgeries [67-70]. Additionally, gas embolism happens in endoscopy [71], tissue biopsy [72], neurosurgery [73], liver transplantation [74-76], during central venous line insertion and removal [77, 78], and even during intravenous antibiotic delivery at home [79]. The use of ultrasound bubble contrast media could also lead to the emboli [80, 81]. Thus, formation and introduction of gas microbubbles in

human blood and tissues is a significant everyday clinical problem affecting thousands of patients undergoing various surgical and therapeutic procedures. If detection of these bubbles at an early stage is possible, action can be taken to prevent the neurological or other complications. Moreover, FDA and Bristol Myers Squibb Imaging issued a new alert and important safety changes to the prescribing information for DEFINITY® (Perflutren Lipid Microsphere, a diagnostic drug used as a contrast enhancement during echocardiographic procedures) in October 2007 [80]. A new clinical study found serious cardiopulmonary problems including fatalities associated with the use of DEFINITY® microbubbles likely attributed to venous gas emboli. The maximum diameter of these bubbles is 20 μm. Therefore, development of an imaging modality capable of imaging and quantification of the circulating microbubbles would have direct clinical benefit for the patients undergoing different echocardiographic procedures.

Bubbles in tissues act as emboli and block circulation, as well as cause mechanical compression and stretching of the blood vessels and nerves [82-85]. Additionally, the blood-bubble interface acts as a foreign surface, activating the early phases of blood coagulation and the release of vasoactive substances from the cells lining the blood vessels and may trigger activation of inflammatory response and, therefore, expression of different proteins and protein patterns [86-94]. This can further worsen gas emboli symptoms. However, the underlying pathophysiology is still poorly understood [95]. Currently, there is no reliable method for prediction or diagnosis of bubble-associated diseases prior to commencement of apparent clinical symptoms (*e.g.*, severe pain in joints, pulmonary problems, disorientation and mental dullness, vomiting, skin rush, and coma). It is widely recognized that prompt detection of microbubbles in tissues and blood is the key for successful management and treatment of persons with required for effective treatment and prediction of severity of emboli as well as for many therapeutic and research applications utilizing bubbles as contrast or drug delivery agents.

Depending on the clinical situation, the nature of the gas emboli and the number of embolic events can vary greatly. For example, Hills and Butler [96] measured intravascular

gaseous emboli ranging from 19 up to 700 μm following decompression in living dogs. Gersh detected bubble sizes between 60 and 300 μm in both intravascular and extravascular sites. However, several studies suggested that bubbles with diameter as small as 8 μm could cause blockage and result in the trauma and onset of the symptoms [80, 97, 98]. Therefore, in order to be effective, an imaging or sensing technique should accurately detect bubbles with a diameter lesser than 8μm. The number of embolic signals can also show wide variations. Georgiadis *et al.* recorded between 0 and 620 embolic events per 30 min period for patients with prosthetic heart valves [99]. Mullges *et al.* have observed between 0.53 and 59.05 embolic signals per minute during extracorporeal circulation in patients undergoing cardiac surgery [100]. However, these observations were limited by the resolution of utilized technique (that is 50 μm at the best) and actual number of "trouble" microbubbles (diameter $\geq$ 8 μm) is unknown. Accordingly, development of a device that allows detection of small microbubbles with sufficient accuracy and sensitivity would be a valuable tool.

Previously, several imaging techniques have been proposed and applied to study microbubbles in blood and tissues including Doppler Sonography, MRI, Nuclear Imaging, and Computer Tomography. Doppler Sonography, the most popular technique since air-bubble interface produce a strong ultrasonic reflection in the region of 1 MHz to 20MHz, which is an ultrasound diagnostic imaging technique, enhanced with Doppler effect, capable of assessment moving bubbles by calculating frequency shift of a particular sample volume [101, 102]. However, Doppler Sonography can detect only moving intravascular bubbles with a diameter of approximately 50 μm [103-105]. Evidently, the resolution of this imaging method should be improved in order to achieve sensitive imaging and assessment of small μm-sized bubbles. Also, a new method has to be developed for the detection of stationary bubbles in tissue that could be used for prediction or diagnosis of gas emboli [106].

Optics-based techniques have great intrinsic potential to achieve the goal of noninvasive imaging of microbubbles in epithelial tissues and blood microvessels. Confocal laser scanning microscopy (CLSM) [107], two-photon fluorescence microscopy (2P-FM) [108-112], and higher harmonic generation (HHG) microscopy [113, 114] are some examples of optical methods that have been applied in different fields of biological research. CLSM have significant axial and lateral resolutions, but it is limited to ~100 μm penetration depth due to high attenuation of visible/ultraviolet excitation light. 2P-FM has a higher penetration depth due to near-infrared (NIR) excitation of fluorophores, but general needs of exogenous fluorophores make this technique not truly "noninvasive." HHG microscopy does not require application of exogenous fluorophores, but is very costly (a commercial Ti:sapphire system with just the basics goes for over $100-150K) and bulky [115]. Optical interferometric techniques are extremely sensitive to local changes in scattering, absorption, and refractive index of the tissues and cells. Since the average refractive indexes of blood, skin, and air are quite different (1.4, 1.55 and 1.0, respectively in NIR), an optical-based sensor will be capable of assessing the formation of gas bubbles with ultra-high sensitivity and accuracy [116, 117]. Here we describe our progress in applying the developed functional biosensor for noninvasive, accurate, and sensitive imaging, monitoring, and assessment of microbubbles in skin and skin's blood mirovessels by using both amplitude imaging and phase-resolved sensing methods.

3.2 Imaging and quantification of microbubbles in clear and tissue simulating scattering media and blood *in vitro*

First, the performance of the developed PhS-SSOCT system was evaluated in water and scattering media that simulates tissue optical properties containing gas microbubbles of different diameters. After the initial testing, the system was used to detect microbubbles in blood *in vitro* and mice tail *in vivo*.

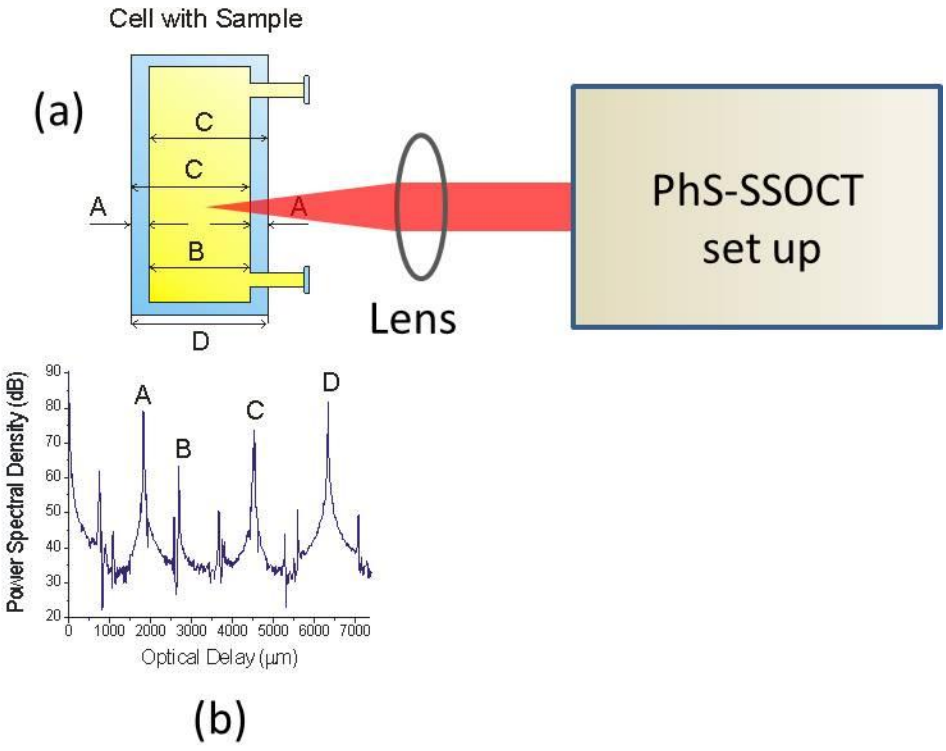

Figure 21: (a) Orientation of the cuvette with respect of the laser beam (b) corresponding 1-D depth profile (A- glass thickness, B- optical path thickness, C=A+B).

For evaluation of the system, the media was injected into a 500 μm flow cuvette and bubbles were generated by introducing different pressures using a peristaltic pump (Fisher Scientific). The cuvette was imaged in M-mode (where 2D OCT images were obtained over time without galvo scanning) before and after inducing bubbles as shown in Figure 21. The amplitude of the interference signals in the time-delay domain was recorded from the cuvette. Four characteristic interferometric peaks were observed corresponding to the interferences between the four surfaces of the cuvette as shown in the Figure 21 (b).

In these experiments, the optical delay is calculated as a function of dynamic refractive index (modified by the presence/absence of microbubbles) from the interferometric peaks that are produced by the reflection from the inner walls of the cuvette in the time-delay domain (B in

Figure 21). The phase is extracted from the complex Fourier transform of the interference fringes and monitored at the interferometric peak that corresponds to the self- interference between the inner glass surfaces. Phase-sensitive measurements of water and scattering media are taken before and after injection of the microbubbles. Since the bubbles induced changes in the refractive index, the diameter of the bubble from the phase shift is calculated from the equation,

$$dn = \frac{1}{l}\frac{\lambda}{4\pi}d\varphi,$$

Equation 11

where *dn* is the refractive index change introduced by the bubble (equal to 0.33 for an air bubble in water), *l* is the diameter of the bubble, $d\varphi$ is the bubble-induced phase shift.

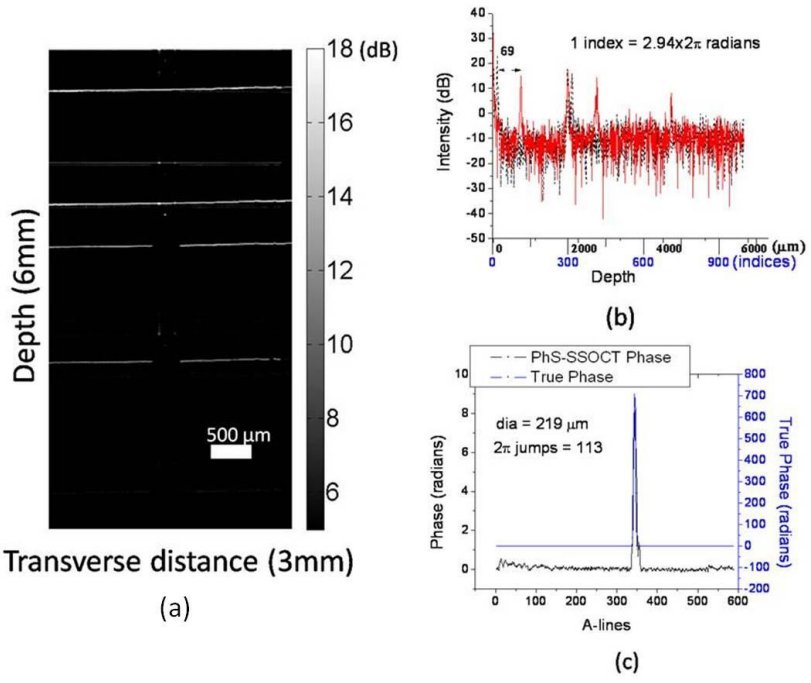

Figure 22: (a) Image of a cuvette of 500 µm thick containing a bubble of 224 µm (fast moving) (b) corresponding 1-D profile showing the shift in peak: red trace is with no bubble and black dashed trace is with the bubble. c) Temporal Phase response at 665 µm peak.

Phase difference between the A-line corresponding to the center of the bubble (determined as a maximal possible change in the phase) and the A-line outside the bubble are computed to quantify the diameters of the bubbles. Bubbles are generated by creating a pressure difference and are circulated using the pump. Bubbles of diameters greater than 8 μm, were imaged first to test the consistency of the PhSSSOCT imaging.

The images were taken in the inter-interference mode, in which the reference arm was placed in such a way that all surfaces of the cuvette were captured in the image as shown in the Figure 22 (a). Since the phase stability was higher in self-interference mode when compared with inter-interference, the phase responses were obtained in self-interference mode whereas images were obtained in inter-interference mode.

Figure 22 also shows the image of a 500 μm cuvette filled with water containing a bubble of diameter 224 μm (actual diameter). The 1-D profile of the corresponding self-interference image and the temporal phase response are shown in Figure 22 (b) and (c). It should be noted that the imaging and the phase response were taken one after the other in very quick succession, as the imaging was done in inter-interference mode and the phase response was studied in self-interference mode. The reference arm is placed at a distance so that the whole cuvette can be imaged without any complex-conjugated images that arise due to the symmetry of FFT. Therefore, for Figure 22 (a), all four bright lines correspond to all four surfaces of the cuvette. In the clear aqueous media, the maximal phase variations were as low as 0.03 radians after a 5-point averaging, which implies that any microbubble that introduces a random phase greater than 0.03 radians can be detected.

Generally, for an optical path difference of one wavelength the phase shift would be 2π in a homogenous media. For an air bubble in water, the change in the refractive index would be 0.33 which translates to a minimum bubble size of 2 μm for the phase to be unwrapped by one 2π

jump. Since the system's resolution is 8 μm, bubbles with diameters greater than 8 μm can be clearly seen in the structural image. When there is no bubble, the optical path length between the inner surfaces of the cuvette is 665 μm (refractive index of water is 1.33, so 500 x 1.33 = 665 μm), which is observed as a peak at 665 μm in corresponding 1-D depth profile as shown in Figure 22 (b). As the beam interacts with the bubble, the optical path length keeps decreasing until it reaches the center of the bubble and increases again to the original value. This change in the optical path length is reflected as a shift in the peak in the corresponding 1-D profile. The larger the bubble, the greater is the decrease in the optical path length and hence the greater is the shift. The number of 2π jumps by which the phase to be unwrapped is then calculated from the peak shifted in the 1-D profile. This unwrapped phase is then added to the PhS-SSOCT phase response to get the true phase response. For the clear media, each depth pixel corresponds to a path difference of 5.88 μm, which is equal to 2.94 "2π" jumps. Thus, for the bubble shown in Figure 22 (a), the number of 2π jumps would be 69/2*2.94 = 113 as the peak shifts by 69 depth pixels (Figure 22 (b)). By plugging this true phase in Equation 11, the size of the bubble obtained is 219 μm. The actual diameter of the bubble measured is 224 μm. The true phase and the PhS-SSOCT phase (phase before adding required 2π jumps) is plotted in the same graph with two different scales on the right and left of the Y-axis.

Figure 23 show an example of small bubbles which cannot be resolved from SSOCT structural imaging. These bubbles can, however, be detected by the phase analysis. The sizes of the bubbles were estimated to be 1.9 μm (but could be 3.9 μm, 5.9 μm, 7.9 μm or 9.9 μm due to the 2π ambiguity as discussed above) and calculated from the phase response shown in Figure 23. The phase response also depicts a small disturbance which can be postulated as another bubble of size less than 1 μm. Therefore, PhS-SSOCT is an effective device for ultra-sensitive quantification of microbubbles with diameters significantly less than imaging capabilities of the

employed system. However, the error due to ambiguity can still be decreased by increasing the number of A-line scans within the same frame and by reducing the beam diameter at the focus.

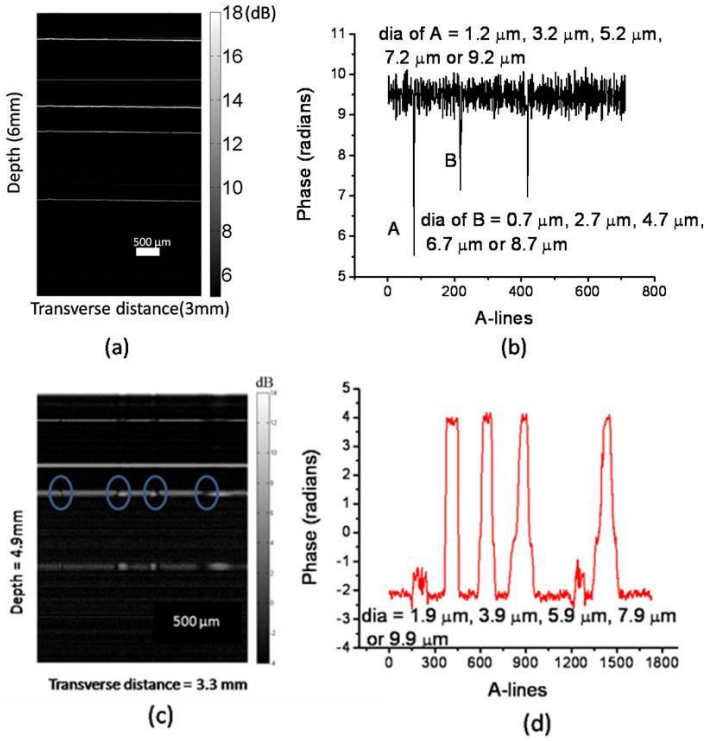

Figure 23: : Image of a cuvvette of 500 μm thick with very small bubbles (a) and (c); and corresponding temporal phase response at 665 μm peak: (b) of (a) and (d) of (c).

For instance, as the beam propagates across the bubble, it interacts more air volume in the bubble indicating the increase in diameter. If an 8 μm bubble is scanned in 4 steps of 2 μm, then the phase needed to be unwrapped only once. Hence, no 2 π ambiguities would be observed.

In scattering media, the detection and quantification of microbubbles were performed on a similar note. 1.54 % polystyrene spheres (PS) were used to simulate the scattering media with a scattering coefficient of 100 cm^{-1} for the 1324 nm wavelength. Figure 24 (a) depicts the image of the cuvette when filled with scattering media. The phase is monitored at the peak corresponding to 705 μm pathlength, the phase variations obtained were 0.04 radians, indicating the minimum

size of the bubble that could be detected is 0.01 µm. Figure 24 (c) shows the image of a bubble with an actual diameter of 142 µm and the diameter obtained from the PhS-SSOCT measurements was 143 µm from Figure 24 (d).

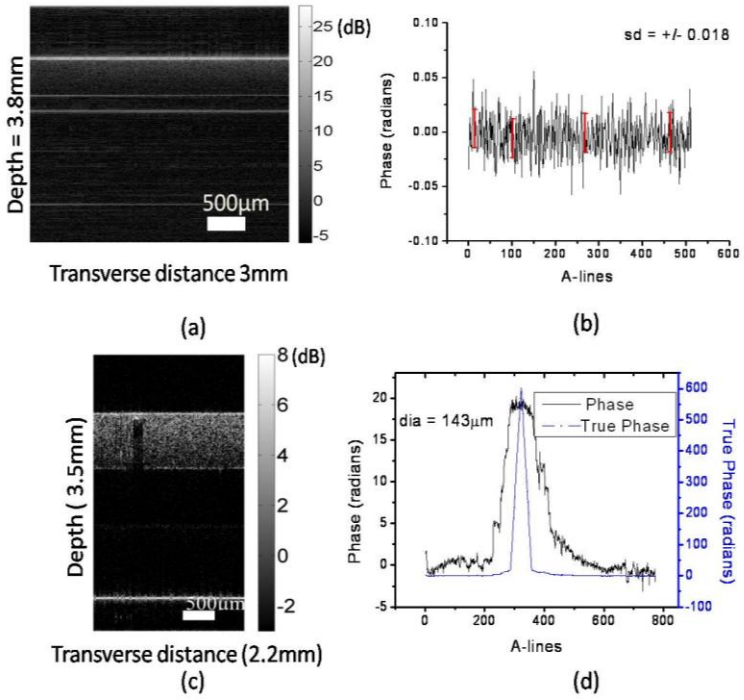

Figure 24: Image of the cuvette with scattering media (a) without any bubble and (c) with a bubble; and their corresponding temporal phase response (b) and (d).

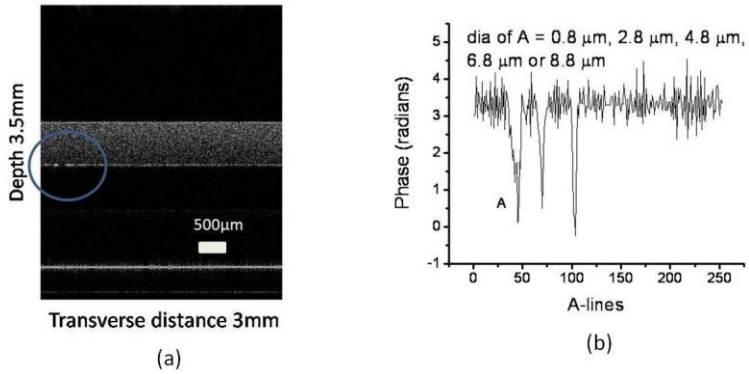

Figure 25: Cuvette with very small bubbles and their corresponding temporal phase response.

The bubbles in scattering tissue-simulating media that are beyond the imaging capabilities of SSOCT are shown in Figure 25. The portion circled in blue in the image is the place where the phase indicates that there could be three bubbles of diameters all around 0.8 μm (but that could be 2.8 μm, 4.8 μm or 6.8 μm). As the sizes of the bubbles are smaller than the focused beam spot (15 μm) they act as a hindrance to the beam passage and create a shadow on the other interface as shown in the Figure 25 (a) [40, 41].

After preliminary testing in clear and scattering media, the system was utilized to detect bubbles in the blood. Porcine blood was treated with anti-coagulant and then injected in a capillary tube. The injection of microbubbles and imaging were performed similar to the one described for clear and scattering media. Results show that the system could detect microbubbles of sizes as small as 6 μm (Figure 26). Microbubbles in flowing blood were also quantified in blood *in vitro.* In a blood flow of velocity ~ 3.2 m/s , microbubbles of sizes 264 μm, 228 μm, 208 μm, 291 μm and 187 μm (numbers correspond from a to f respectively in Figure 27) were quantified using phase resolved OCT and were verified from the image [118].

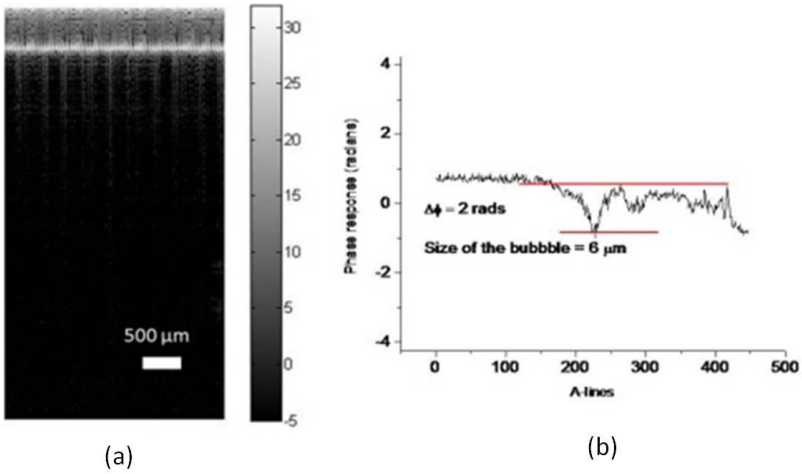

Figure 26: M-mode image of blood in capillary tube and its corresponding phase response.

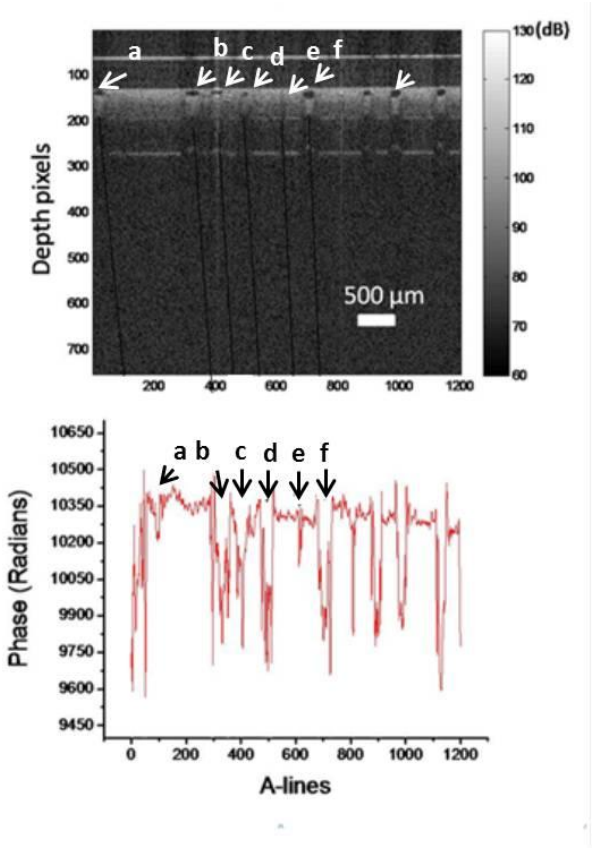

Figure 27: Microbubbles in flowing blood and its corresponding phase response.

3.3 Tissue phantom studies

The results confirmed the ability of PhS-SSOCT to quantify microbubbles in testing media. To further evaluate the system for its performance in flowing blood in a vessel embedded inside a tissue, phantom studies were performed.

A phantom that mimics a tissue with a blood vessel was prepared. The phantom had a layer of scattering media with optical properties similar to the skin, then a capillary containing porcine blood and a layer of another scattering media under the capillary. Figure 28 depicts the OCT image of the phantom in both across the vessel and along the vessel.

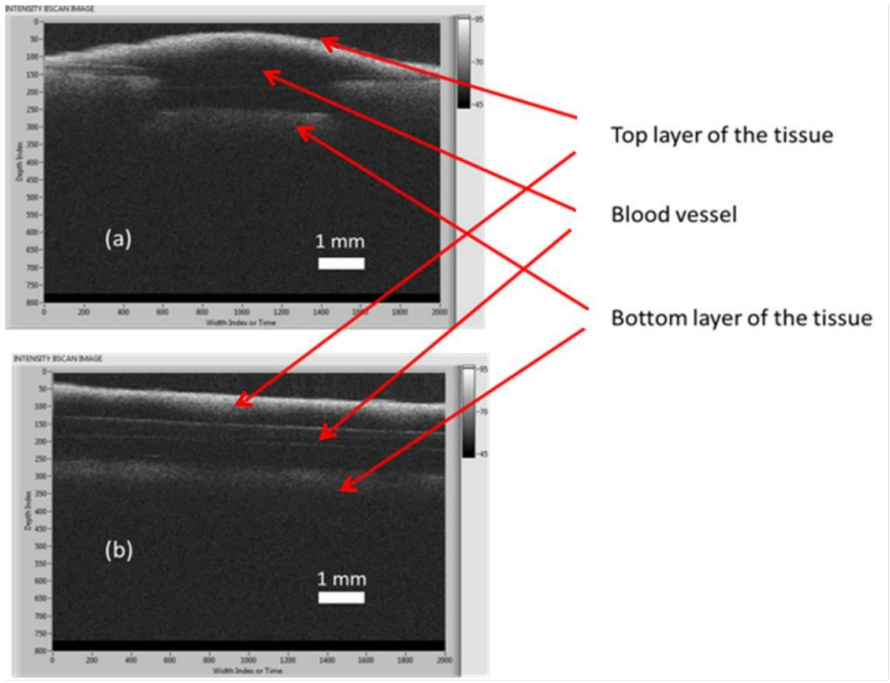

Figure 28: Phantom properties.

Air bubbles were generated in the blood vessel of the phantom by applying variable pressures. Numerous air bubbles of sizes up to 400 µm were generated and were passed through the capillary (blood vessel phantom). The real time imaging of the PhS-SSOCT is then utilized to obtain M-mode measurements before generating the bubbles and after generating the bubbles. Figure 29 (a) shows the M-mode image of the phantom before passing the bubbles.

The phase response corresponding to the two layers of the phantom blood vessel is depicted in Figure 29 (b) which indicates a slow increase and then decrease in phase. This phase profile is attributed to the presence of only environmental noise and the noise due to the movement of the blood. When a bubble of the diameter ~ 260 µm is passed through the phantom vessel, the PhS-SSOCT could detect it in both the structural image and the phase response as shown in Figure 29 (c) and (d). The diameter was calculated from the structural image as well as the true phase as described earlier and the values obtained were 256 µm and 258 µm, respectively. We have also performed similar experiments with lipid based perfluteren microbubbles (DEFINITY ®, Bristol Meyers squib) instead of air microbubbles.

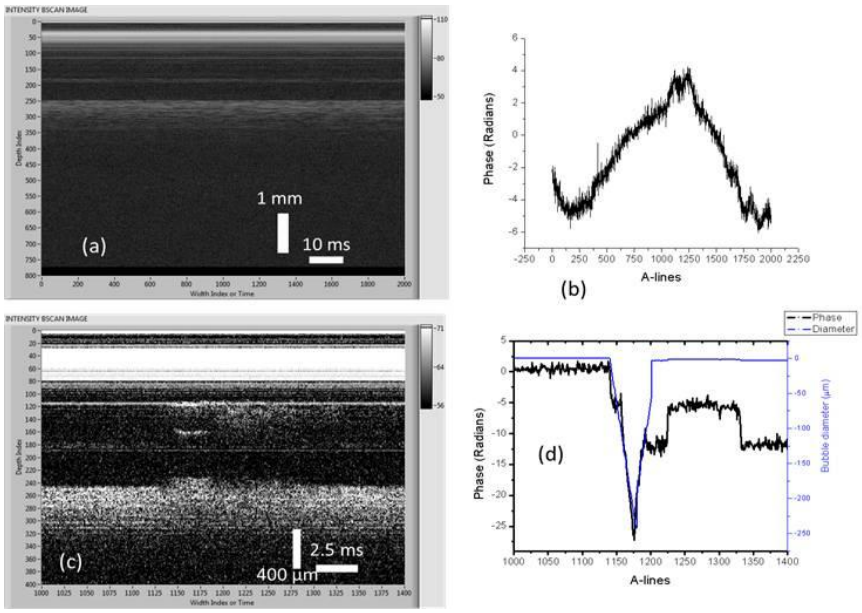

Figure 29: Bubble in the phantom (a) Phantom with no blood flow (b) corresponding phase (c) Phantom with bubble and (d) phase response showing the bubble.

The phantom studies have confirmed the ability of PhS-SSOCT to image microbubbles in blood under a scattering media. Therefore, the PhS-SSOCT is now ready to be applied to detect stable and moving microbubbles in live animals. In the next section we demonstrate the application of PhS-SSOCT to detect stable and moving microbubbles in mice tail vein under *in vivo* conditions.

3.4 *In vivo* studies

For *in vivo* studies, the experiments were conducted in two phases: the first phase was to identify blood vessels under *in vivo* conditions and microbubbles were detected in the second phase. In the first phase, various sections of the mice body were imaged and a method was developed to identify the blood vessels from the structural images. In general, blood vessels could be easily identified from the Doppler images; however, a clear Doppler signal could be attained only by scanning a small region (0.5 – 1 mm). Moreover, strength of Doppler signal depends greatly on the angle made by the beam with the blood flow. In order to obtain a strong Doppler

signal, the angle between the beam and the flow direction has to be as minimal as possible. These limitations hinder the accuracy of detection of blood vessels.

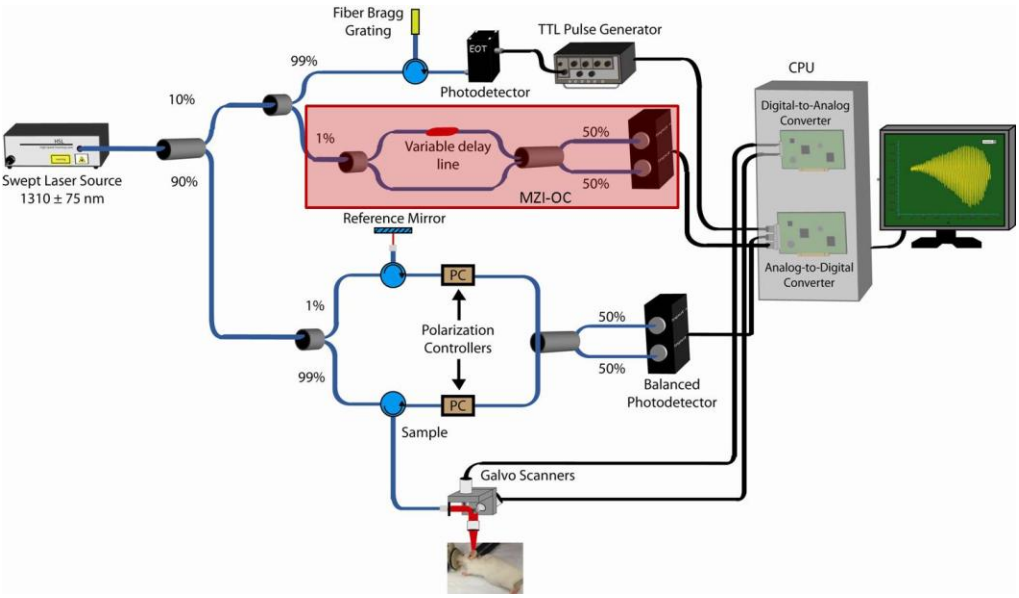

Figure 30: Schematic of PhS-SSOCT for *in vivo* experiments.

Therefore, a method for identification of blood vessels without the aid of the Doppler signal is required which is developed in the first phase. In the second phase, microbubbles were injected into the mice tails and detected using PhS-SSOCT.

To perform *in vivo* studies, the sample has to be prepared in order to keep the animal alive as well as maintain its physiology. This was achieved by the following procedure: the mice were obtained from the animal facility and were transferred to an anesthesia chamber (Summit, Veterinary Anesthesia Systems). The anesthesia chamber consists of two pathways, one for the transfer of oxygen and the other for the isoflurane. Oxygen and isoflurane were mixed at 50% concentration and supplied to the mouse. Isoflurane is responsible for inducing unconsciousness in the mouse whereas oxygen which powers up the whole anaesthesia system allows the diffusion of isoflurane. After the mouse got unconscious, it is removed from the chamber and placed under the imaging lens of the PhS-SSOCT. To keep the mouse continuously under anesthesia, the

airway from the anesthesia chamber is fixed to the mouse nose through a nose piece. The mouse was continuously monitored for any changes in its breathing. If any change was noticed, the concentration of anesthetic was varied accordingly to resume the mouse breathing.

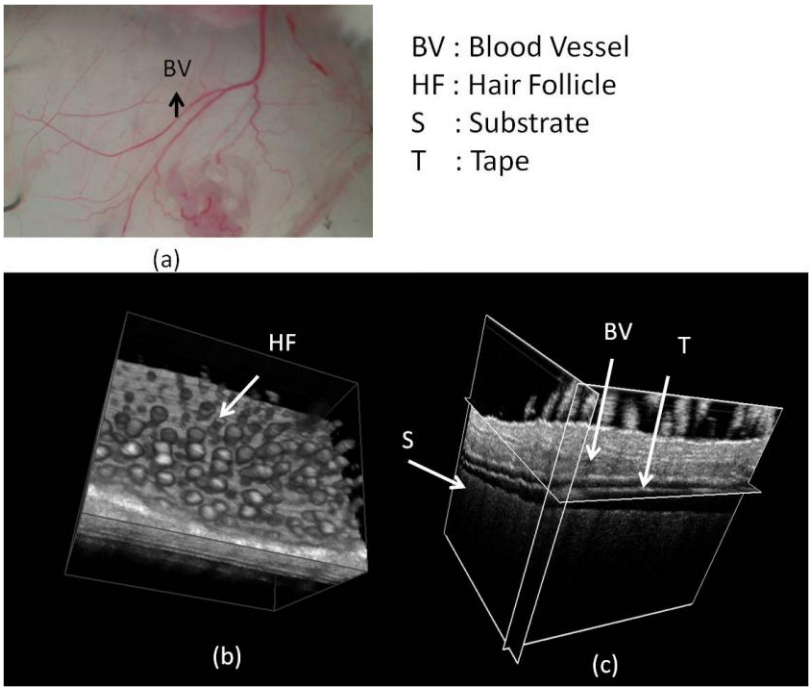

Figure 31: (a) Photographic image of mouse ear (b) 3D image obtained using PhS-SSOCT (c) 3D parallel view.

The mouse was kept alive under anesthesia for less than two hours which was the total time taken for the experiments. All these procedures were approved by the animal committee of the University of Houston.

The schematic of PhS-SSOCT that was utilized to obtain the images is shown in Figure 30. Mice ears and tails were used to locate and study the images containing blood vessels. The blood vessels in the ear are clearly visible with the naked eye as shown in Figure 31 (a). 2D, 3D and Doppler images were obtained at the location containing the vessels. The blood vessels were identified using the Doppler images and the corresponding 2D and 3D images were observed.

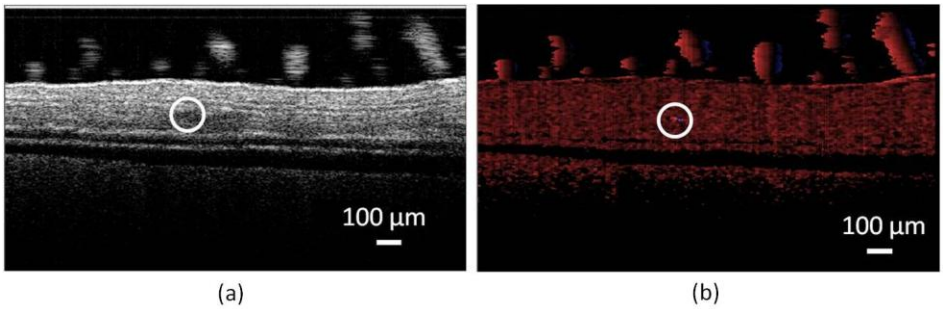

Figure 32: 2D image of the mouse ear and its corresponding Doppler.

The mouse ear was imaged for 1.25 mm X 1 mm dimensions at the area shown in the Figure 31 (a). The ear was taped to a rubber platform to avoid any movements. The corresponding 3D image obtained from the PhS-SSOCT is shown in Figure 31(b). It can be observed that the scattering signal is lower at the region corresponding to blood vessel. This is attributed to the fact that the IR light is absorbed more by the blood than the surrounding tissue or the vessel wall. Therefore, in the 3D figure, the region corresponding to a dark gap can be identified as a blood vessel (pointed in the Figure 31 (c). The presence of a blood vessel can be further verified by the corresponding Doppler image as shown in Figure 32. The Doppler signal corresponding to the 2D shows the blood flow at the region where the scattering is low. Therefore, from these observations, it can be assumed that the blood vessels can be identified from the structural image.

Phase analysis was performed at that region to further manifest that the region corresponds to a blood vessel. This was achieved by observing the phase difference between the walls of the blood vessel in the M-mode image. The walls of the vessels that are identified in the Figure 33 (a) are shown in the M-mode image in Figure 33 (b). The vessel thickness is quantified to be ~ 450 µm. The phase difference between the walls of the vessels are shown in the Figure 33(c). From the phase difference shows a periodic disturbance at every 1.85 s indicating the movement of the mouse at every end of a breath cycle. Within the breath cycle, the phase response shows a periodic sinusoidal signal with a period of 0.117 s. This signal represents blood flow. Moreover,

the phase differences at a different location other than a vessel in the tissue do not contain the high frequency signal, indicating that there is no flow.

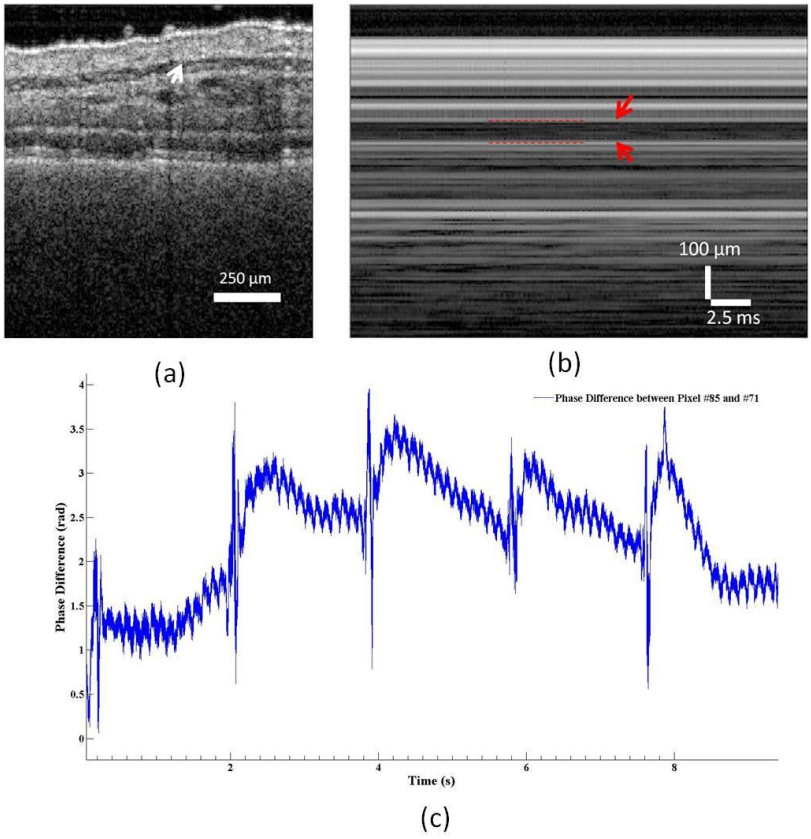

Figure 33: (a) 2D image of the mouse ear (b) m-mode image of the ear containing blood vessel (c) phase difference between the walls of the vessels.

From the phase signal, the pumping rate of the heart was quantified to be 500- 600 beats per second. From all of the above results, we can confirm that we were observing at the blood vessels.

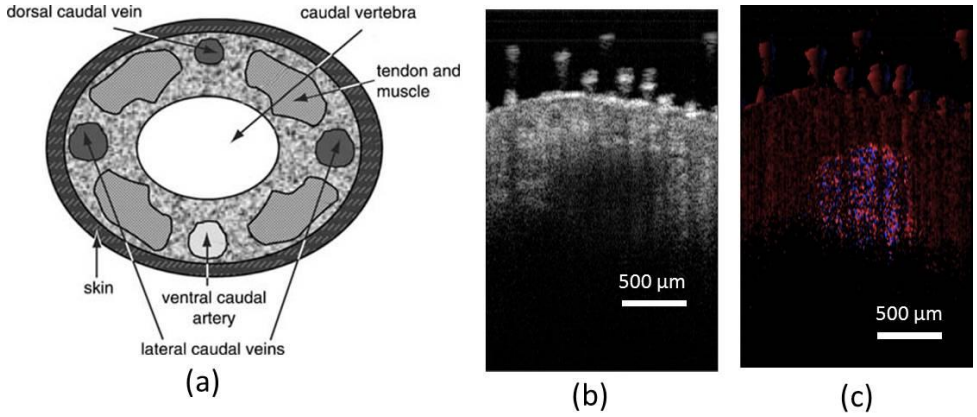

Figure 34: (a) cartoon image of a tail (b) 2D OCT image of the tail (c) corresponding Doppler image.

The similar approach was followed to identify blood vessels in the mouse tail. The schematic of the mouse tail is shown in the Figure 34 (a). OCT imaging was performed at the ventral caudal artery from the ventral side across the mouse tail for 1.8 mm. The 2D OCT image and its corresponding Doppler image are shown in Figure 34 (b) and (c). The vessel can be identified as a dark circular patch and the Doppler image corresponding to the 2D image shows that there is a blood flow in that region. The same portion of the mouse tail was also imaged in the longitudinal direction. In longitudinal direction, the blood vessel is again identified as a dark patch as shown in Figure 35 (a). The 3D Doppler image shows the presence of blood flow as shown in Figure 35 (b). All these above findings suggest that the blood vessels could be identified from the structural images even though there was a low Doppler signal.

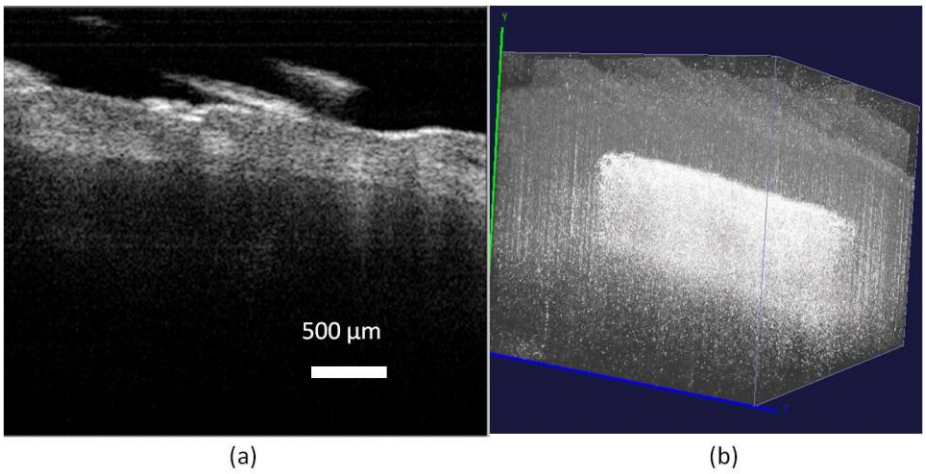

Figure 35: (a) 2D image of the mouse tail in longitudinal direction (b) 3D image of the Doppler signals.

Now that blood vessels could be identified in the mouse tail from the OCT image, microbubbles were induced and continuously monitored in the caudal artery of the mouse tail.

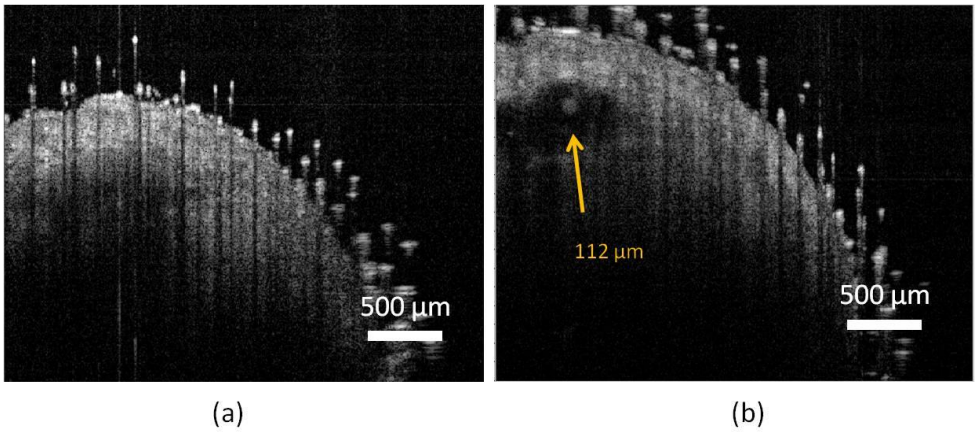

Figure 36: Transversal image of mouse tail (a) before microbubbles injection and (b) after microbubbles injection.

Definity microbubbles were induced in the up-stream blood flow of the mouse tail artery via direct injection. 2-D images were continuously acquired at a rate of 20 fps before injection, during injection and after injection of the microbubbles at 3 cm away from the injection site.

The images corresponding before injection and after injection are shown in Figure 36 (a) and (b) respectively. In the Figure 35 (a), the vessel can be seen as a dark patch with very low but uniform scattering signal similar to Figure 34 (a). When Definity bubbles were injected, the Definity bubbles travelled along the upstream flow of the blood. Few of the Definity bubbles formed clusters and flowed along the vessel. From continuous imaging of the blood vessel, one of the frames showed the cluster of Definity bubbles. As the light scattering by Definity bubbles is more than blood, the cluster was identified as a scattering ball. Figure 36 (b) shows one of the frames where a cluster of Definity bubbles were recorded. From the image, the cluster size was quantified to be 112 μm. Definity microbubbles entered the blood stream after injection that provided some scattering signal in the image. And when the injection was stopped and Definity bubbles went past the imaging region, the blood replaced the Definity microbubbles. Therefore, no more scattering was observed. This whole process was captured in a video and the successive images were shown in the Figure 37.

After successful detection of Definity microbubbles, PhS-SSOCT was utilized to detect air microbubbles in the live mouse tail. After the injection of Definity microbubbles, air microbubbles were injected after two minutes which was greater than the half life of the Definity microbubbles. Again, continuous imaging was performed before, during and after the injection of air microbubbles. Figure 38 shows a 2D frame that captured microbubbles as small as 56 μm.

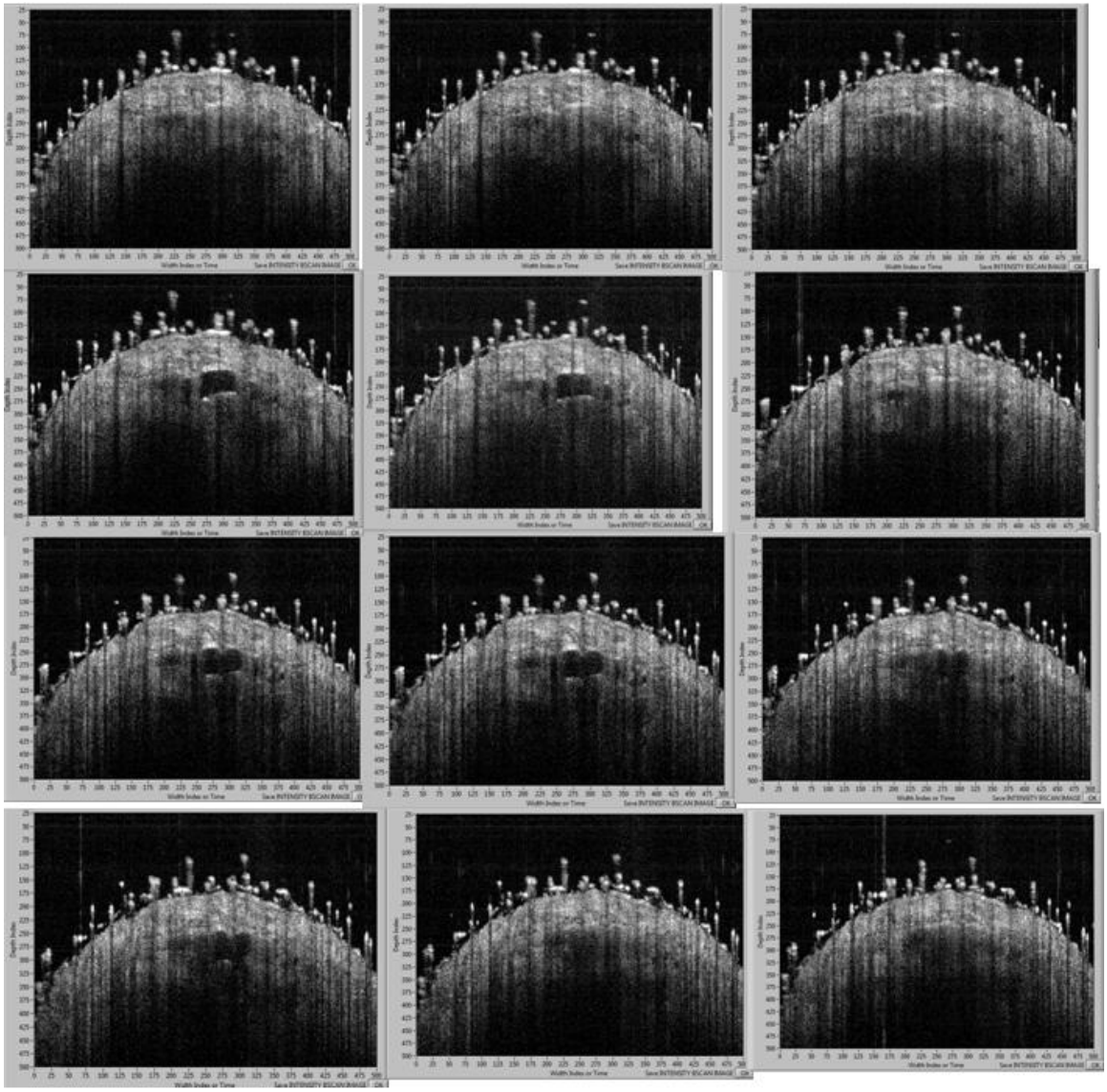

Figure 37: Continuous frames showing the process of microbubbles formation and replacement of blood.

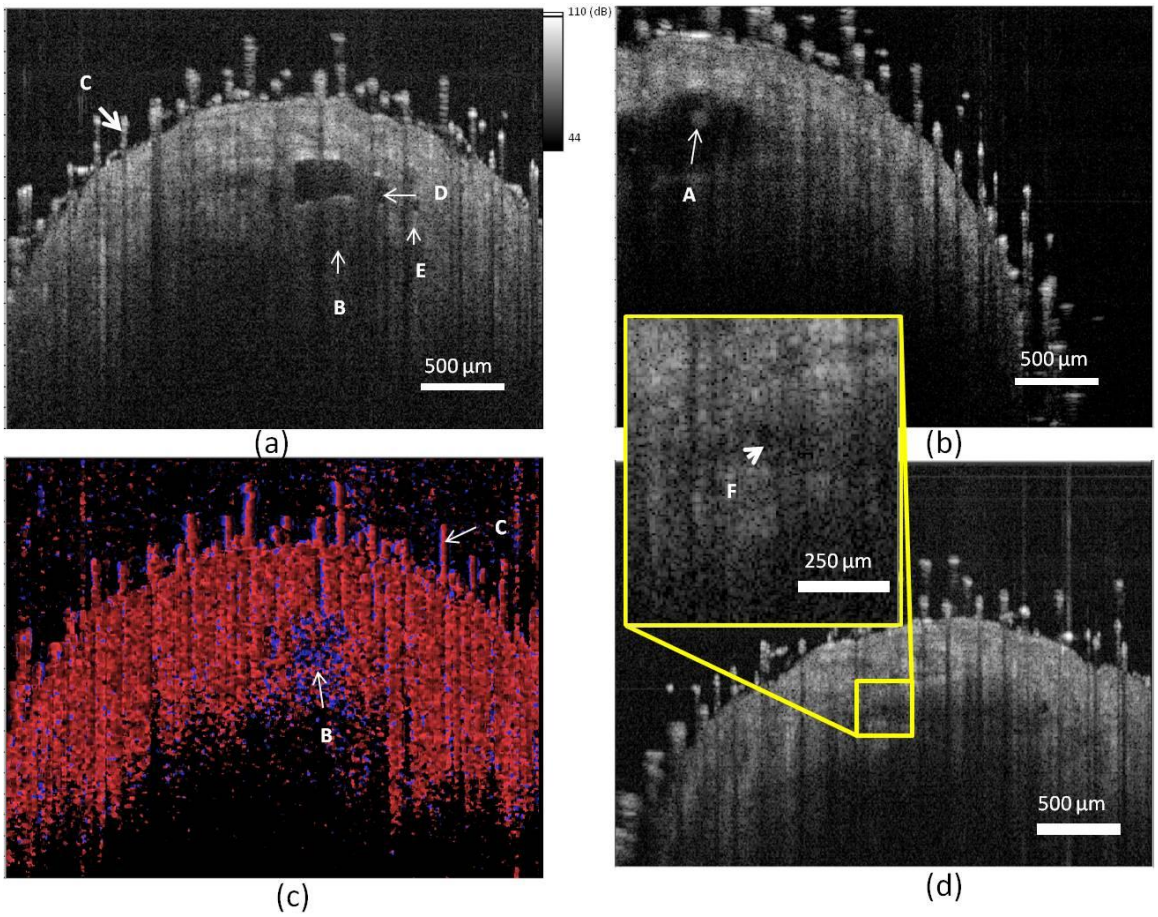

Figure 38: (a) 2D cross section of the tail (b) 2D cross section of the tail showing cluster of bubbles (c) Doppler signal showing the blood flow (d) 2D cross section showing 56 µm microbubble.

The frame also shows various bubbles such as stable and moving microbubbles. Stable air microbubbles were identified as a small dark circle that was not observed before the injection of the microbubbles. Similarly, circular scattering structures that were not observed before injection but were observed after injection were classified as clusters of Definity microbubbles. From all these findings, it can be concluded that PhS-SSOCT is an effective tool to detect and quantify gas microbubbles in live animals. These results also demonstrate that the PhS-SSOCT has the potential to diagnose diseases related to DCS.

IV. CHAPTER 4. ELASTOGRAPHY

Elastography is a noninvasive technique that allows quantification of biomechanical properties of tissue from its response to an external stimulus [119, 120]. This modality has shown great promise for various medical applications primarily because of the fact that pathological changes are often correlated with changes in tissue stiffness [121, 122]. For instance, an intravascular ultrasound (IVUS) is used to measure strain maps that help detect coronary lesions [123], atherosclerotic plaques[124], and cardiac deformation[125]. Other elastography techniques are used to reveal the shape and size of tumors [126]. Therefore, elastography is emerging as an effective tool for diagnosis.

Elastography could be implemented using several techniques. Magnetic Resonance (MRI) [126-131], Atomic Force Microscopy (AFM) [132-135], optical and microscopic imaging techniques and ultrasound-based techniques are used to define mechanical properties from the organ to the cellular level [136-144]. Outstandingly, optical elastography methods allow high sensitive measurements of ocular tissue mechanical properties [145]. Due to its high resolution, a very small external compression on the order of nanometers can be reliably measured using different optical methods [146-152]. OCT based elastography is termed as optical coherence elastography (OCE). OCE allows noninvasive measurement of elastic properties of the tissues at a higher resolution than compared to other elastography modalities such as US or MRI. Until now, OCE has been used to investigate microscopic deformation in human skin, porcine muscle, collagen organization in musculoskeletal tissue, strain maps in engineered tissues and provide material properties of the cornea. In this dissertation, a novel elastography system based on a phase stabilized swept source OCT and a method to quantify the wave parameters in mice corneas *in vivo* is introduced and evaluated.

Most of the elastography systems consist of an excitation unit to introduce a stimulus and a sensing unit to detect the tissue response. Tissue response is then passed through post processing

algorithms to retrieve information that allows quantification of biomechanical properties. The similar procedure is followed in developing a Phase Stabilized Swept Source Optical Coherence Elastography (PhS-SSOCE). The first part of this section discusses the contribution of elastography for ophthalmic applications. The second part deals with the instrumentation, methodology and postprocessing techniques to quantify wave propagation parameters required to quantify biomechanical properties of tissues. Then the developed system was evaluated in phantoms,evaluated for *in vitro* and *ex vivo* mice eyes and finally, the system was applied to *in vivo* studies.

4.1 Ophthalmic elastography

The human eye is the organ that provides vision. It is a spheroid structure that rests on the frontal surface of the skull. It contains three layers: the sclera, the choroid and the retina. The sclera is the outermost layer of the eye. The center of the sclera is the cornea, a transparent connective tissue of thickness ~ 550 μm. This tissue provides approximately 2/3 of the optical refracting power of the eye and its shape and structure are critical for normal vision. Therefore, the disorders related to the cornea such as keratitis (ulcers in the cornea), keratoconus (change in corneal structure), astigmatism and different types of corneal dystrophy can lead to permanent blindness. Keratoconus and other similar ectatic diseases of the cornea can cause severe visual disability that predominantly affects young adults. Keratoconus (prevalence 1:2000) is one of the leading causes of corneal transplant in the United States and in the developed world [153-155]. Advanced keratoconus is characterized by thinning of the corneal stroma and conical deformation of the tissue causing pronounced optical distortions and poor vision. Typically this condition is diagnosed and monitored using corneal topography to observe and quantify the gross morphological distortion of the cornea. In addition to topographic imaging, characterization of the biomechanical properties of the cornea could also provide useful diagnostic information for early detection of corneal pathologies such as keratoconus and other diseases [156-159]. Knowledge of

corneal structural properties would also be informative for surgical planning and the prediction of clinical outcomes from surgical treatments, *e.g*., responses to corneal refractive surgery [160, 161]. Similarly, it can be used to evaluate the healing process of post surgeries such as corneal transplants [160], LASIK and corneal photo ablative procedures [160, 162, 163]. It also provides information for diagnosis and management of glaucoma by allowing accurate measurements of intraocular pressure (IOP) [163, 164]. Therefore, it is important to study both the physiology and pathologies associated with the cornea.

The second layer of the tissue underneath the sclera is the choroid that contains blood vessels that nourish the tissues. The choroid consists of a ciliary body that contains the muscles used to accommodate the lens. The lens is a biconvex structure located between the pupil and the vitreous as shown in the Figure 39. It is responsible for focusing images at varying distances by becoming more convex for near vision and less convex for farther vision and this process is termed as accommodation.

Loss of the lens ability to accommodate makes the vision blurred and can cause blindness. This disorder is called presbyopia. Presbyopia is one of the most common ocular disorders affecting humans over the age of 45 [165]. The exact cause of presbyopia is still a matter of debate [166]. However, it has been suggested that presbyopia is resulted by the stiffening of the lens and this loss of focus on near objects can be explained either through Herman von Helmholtz's theory of accommodation of the lens [167], or by a controlled variation of lens thickness and curvature[168]. Thomas Young had proved, over 200 years ago, that in order for accommodation to occur the lens would need to change shape; the increase in the stiffness of the lens would inhibit the contractions of the ciliary muscles causing loss of accommodation. Therefore most surgical presbyopia correction techniques currently under development, including laser softening and lens refilling surgery rely on the assumption that presbyopia is due mainly to the stiffening of the lens [169]. A better understanding of how the lens biomechanical properties change with age and their relation with the loss of accommodation is a fundamental requirement

for the development of better models of accommodation and presbyopia and effective presbyopia correction techniques.

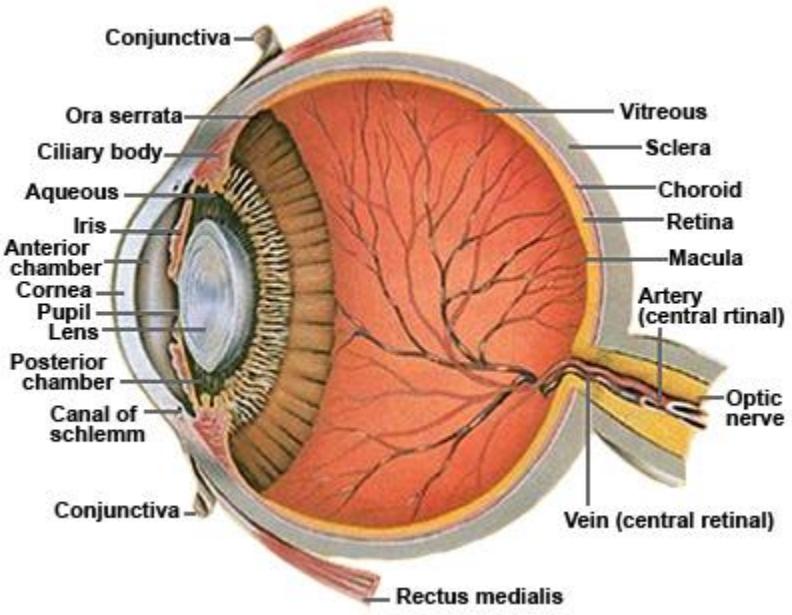

Figure 39: Anatomy of eye (Courtesy:[170] master eye associates).

The biomechanical characteristics of ocular tissues can have a profound influence on the health, structural integrity, and normal function of the eye [171, 172]. Over the past twenty years, there have been many attempts to estimate the biomechanical properties of the cornea. Most previous attempts to measure the biomechanical properties of the cornea induce a stimulus and measure the corneal response to that stimulus. The stimulus can be induced in many ways; *e.g.*, exciting with external force [173], ultrasound [162] or by using a laser pulse [174]. While, these methods are considered minimally invasive techniques to induce elastic waves in other soft tissues, (*e.g.*, the breast, liver, or muscle), FDA standards require lower vibrational intensities in the eye [157, 175]. Low intensities can only induce low amplitude vibrations; therefore, a device that can detect minute amplitude vibrations on the ocular tissue is required.

Most tissue imaging techniques such as MRI [126-128], B-mode ultrasound [137, 142, 144], acoustic radiation force imaging [176, 177] and supersonic shear imaging [157, 178, 179] require tissue stimulation on the order of millimeter amplitude. This limitation of resolution is one of the main reasons that none of the above techniques have been applied to the characterization of the biomechanical properties of the eye.

Another way of inducing vibrations that was clinically accepted is by using a pulse of air. This type of excitation is used in ocular response analyzer (ORA) which is a commercially available clinical instrument used for clinical evaluation of corneal biomechanics [180]. The ORA utilizes an electro-optical system to record applanation (flattening) of the corneal surface during both inward and outward deflection in response to an air pulse. Biomechanical properties are then estimated from the time taken for the corneal applanations to occur [180, 181]. Therefore, ORA require a large displacement of the corneal surface for evaluating biomechanical properties. Moreover, the predictability of this system is still under investigation [157]. Currently, there is no ideal clinical system that allows a noninvasive estimation of biomechanical properties of the cornea. This dissertation introduces a noninvasive method of detecting vibrations on the corneal surface with high sensitivity. The method also measures the parameters required for estimating biomechanical properties of the cornea from a very low amplitude (~ a few microns) excitation.

Lens mechanical properties have been measured directly or indirectly only *in vitro*, typically by applying a radial or axial forces. Radial forces mimicking zonular tension during disaccommodation have been produced by spinning the lens about its axis at various speeds [182, 183] or by mechanical stretching [184-187]. Resulting changes in lens size and shape determine its resistance to deformation. Other techniques include axial compression using static and dynamic indentation methods to measure the properties of whole lenses [188-191] or of the cortex and nucleus after dissection [192-198]. Separate measurement of the cortex and nucleus are of particular interest because the results of *ex vivo* experiments [193, 195, 196, 199] and finite-

element modeling [200] indicating that there is a stiffness gradient within the lens which changes with age and influences accommodative amplitude. *In vitro* techniques suffer from large variability, in part because of the difficulty in preserving the hydration state of post-mortem lenses. Unfortunately, due to its location inside the eye, the *in vivo* lens is not accessible for direct mechanical probing. There is currently no technique which provides *in vivo* measurements of the mechanical properties of the lens, and ocular tissues within the eye in general [193].

Our method utilizes optical coherence tomography (OCT), a non-invasive in-depth imaging technology, to detect the vibrations on the corneal surface. OCT was first applied in 1998 by Schmitt to measure microscopic deformations due to compressive stress [201]. Since then, several groups have been utilizing OCT to obtain the biomechanical properties of tissues [174, 202-204]. Corneal biomechanics using OCT has been demonstrated by De la Torre et al. and Ford et al. in *ex-vivo* [205] and *in-situ* [206] conditions, respectively. Recently, Alonso-Caneiro et al., measured corneal dynamics *in vivo* by observing the corneal response to an air pulse from series of depth-wise images generated from swept source OCT [164]. However, they had to displace the cornea in the order of 1 mm in order to perform measurements. No work related to estimation of corneal biomechanics *in vivo* with minute corneal displacement has been reported yet mainly due to the difficulty in inducing vibrations and detect such small amplitudes simultaneously in live conditions.

This dissertation is focused on the first systematic approach to combine expertise in OCT system development and tissue biomechanics in order to develop instrumentation and methods for the routine noninvasive *in vivo* assessment of ocular tissue pathology. The tool allowed a direct quantification of elastic wave propagation parameters of the lens and cornea *in situ* and *in vivo*.

4.2 Instrumentation of PhS-SSOCE

PhS-SSOCE consists of excitation unit, sensing unit and data acquisition unit. The excitation unit is responsible for inducing vibrations on the surface. The sensing unit measures the

amplitude of vibrations. Amplitude vibrations are achieved by obtaining M-mode images at spatially distributed points on the surface. Data is recorded using the data acquisition unit which is also responsible for providing synchronization between the sensing unit and the excitation unit. In this subsection, each unit is described in great details.

4.2.1 Excitation unit

Three different types of excitation were used in this dissertation: direct tapping with thin

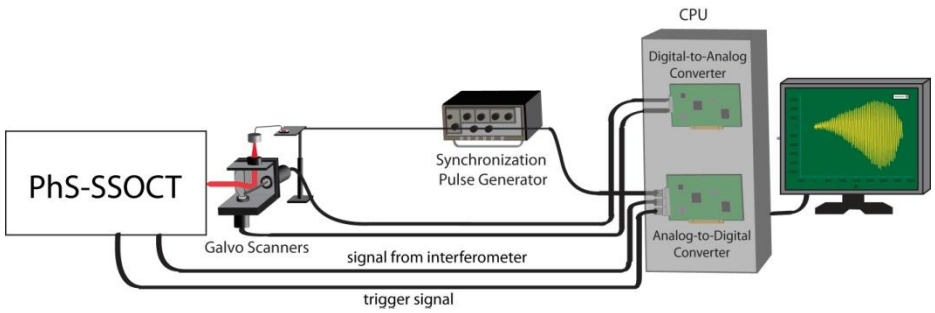

Figure 40: PhS-SSOCE with wire tapping.

but stiff wire, using ultrasound pulses, and also using small puffs of air. In the first case, a thin wire was attached to a speaker diaphragm whose electric controls were connected to a wave generator. The vibrations of the speaker diaphragm correspond to the waveforms generated by the wave generator. For instance, the diaphragm vibrates in a sinusoidal pattern if a sinusoidal wave was generated by the wave generator. These vibrations were carried by a thin wire that was attached to the diaphragm to the sample surface as shown in the Figure 40. When a pulse was generated by the wave generator, the wire tip comes in contact with the sample surface only once and the sample vibrates with its natural frequency thereafter. Therefore, dynamic response of the tissue can also be generated using this kind of excitation.

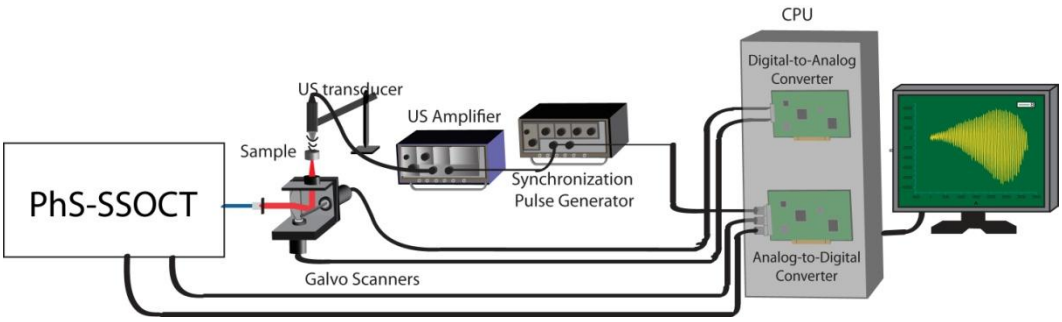

Figure 41: PhS-SSOCE with US excitation.

In order to produce excitation without direct contact with the sample, the ultrasound (US) pulse and air puff were utilized in the excitation unit. US excitation consists of a signal generator that generates a 7.5 MHz sinusoidal wave which is fed to a 7.5 MHz ultrasound transducer focused at the surface of the phantom as shown in the Figure 41. Even though US excitation offers a noninvasive method of inducing waves, there are other challenges to incorporate this kind of excitation. Firstly, due to the heavy attenuation of US wave in air, a gel is required between the sample and the US transducer. The US gel would create irritation in the eye and hence cannot be utilized in a live eye. Moreover, the gel would also introduce phase noise which would reduce the sensitivity of the measurements. Secondly, the exact focal point of the US transducer is difficult to measure. The variability in the focal point would introduce errors while measuring the velocity of the wave. Lastly, as the US transducer and the imaging lens should lie on the same side of the sample, it requires complex instrumentation to maintain the same focal point for US and laser light. The same focal point could be achieved by giving inclination on one of them; however, the inclination modifies the wave propagation which causes errors in quantifying the wave parameters. Therefore, US excitation was not utilized for *in vivo* studies. However, since the main aim of this dissertation is to develop a method to quantify wave parameters, the method was validated in phantoms for US excitation as well.

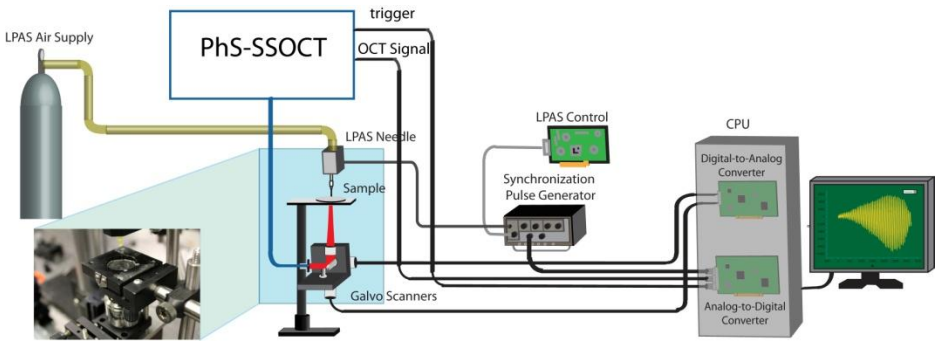

Figure 42: PhS-SSOCE with air puff stimulation.

The third type of excitation utilized to induce vibrations is a puff of air. A short duration focused air puff is delivered on to the sample using a syringe needle. The needle is connected to the output end of an electric solenoid via air passage tubes. The input end of the solenoid is connected to the air supply as shown in the Figure 42. A constant pressure was supplied to the solenoid and the opening of the valves and the amplitude of the air puff were controlled through an electric circuit (labeled local pressurized air stimulation (LPAS) control in the Figure 42). The LPAS circuit is operated by a switch that opens the solenoid valve whenever the switch is closed. The LPAS circuit also outputs a pulse with the closure of the switch, which served as the timing of the pulse. The timing of the pulse gave the moment when the solenoid valve opened which was the time of air puff delivery which gave the time when the wave was induced. Therefore, the time when the wave was introduced on the sample was recorded.

4.2.2 Sensing and data acquisition unit

The PhS-SSOCT is used to detect the tissue response to the induced stimulus. PhS-SSOCT records the phase of the interferometric signal and the tissue vibrations were extracted from the phase information. Since the tissue vibrations were measured relative to the induced wave, synchronization between the induced wave and the tissue response is required. To achieve synchronization, the excitation pulse was recorded simultaneously with OCT data using the

channel in the ADC card where MZI-OC data was acquired. As there was no other channel available to record MZI-OC data for *k*-space calibration, as done in the previous PhS-SSOCT system, calibration here is performed with pre generated data. The *k* –space calibration in the modified PhS-SSOCT is performed as follows: the sample was replaced with a mirror and the path difference between the sample mirror and the reference mirror is kept at a fixed optimal distance. The fringes from the reference and sample mirrors are converted to the complex domain using Hilbert transformation [207]. Unwrapped phases were extracted from these complex fringes which reveal the behavior of the propagation vector *k* provided that the path difference is kept constant (Equation 12). Since the path differences are kept constant, the unwrapped phase profile gives the nonlinearity in the wavelength scanning in *k*-space and was corrected by linearizing the unwrapped phases using the Equation,

$$Phase\ differences = k * path\ differences.$$

Equation 12

The coefficients obtained by linearizing the unwrapped phases were saved and used to convert the raw OCT data to linear *k*-space. Although this procedure does not allow dynamic calibration, the calibration coefficients are obtained before every experiment, making the method quasi-dynamic. With this procedure, the system showed a depth resolution of ~ 8 µm, imaging depth of 9.0 mm, phase stability of 0.04 rad and time resolution of 33 µs.

4.3 Quantifying methodology

This section deals with the experimental and quantifying methods to obtain parameters of propagating wave from PhS-SSOCT phase data. Wave parameters such as amplitude of vibrations, spatial damping of the wave amplitude and wave velocities was quantified. Two types of excitation waveforms were used for this study; they were harmonic excitation and pulsed

excitation. The procedure of quantifying wave parameters in both type of excitation is detailed in this sub section.

4.3.1 Harmonic Excitation

Harmonic excitation vibrates the tissue continuously with a given frequency and known amplitude. The frequency and amplitude of excitation wave were chosen based on the limitations of the sensing unit. The sensing unit is capable of acquiring 1500 points in 50 ms. Therefore, the range of frequencies the system can measure is 20 Hz to 15 kHz. Within this range, there are other frequencies that correspond to other factors such as environmental noise, electronic noise and external vibrations. In order to choose the appropriate frequency of excitation which is free from noise, a preliminary study was performed on a speaker diaphragm. A speaker diaphragm was imaged by M-mode scanning (OCT A-scans at a fixed position over time) at 1 kHz sampling rate. The speaker was connected to a personal computer and a software (Audacity) was used to play a sinusoidal tone of various frequencies (80, 100, 250 and 500 Hz). The peak corresponding to the surface of the diaphragm was tracked using a MATLAB code and phase was monitored at that peak. FFT was performed on the phase information to observe the presence of all frequency components. Absolute displacement amplitudes were quantified from the phase measurements using the relation shown in Equation 13,

$$V = \frac{\lambda}{2 * \pi} * \varphi.$$

Equation 13

where φ is a phase (radians), λ is a wavelength (nm), and V is a displacement amplitude (nm). Figure 43 shows the plots obtained for the vibrations induced on the surface of the speaker diaphragm. Figure 43 (a) corresponds to the peak position of the surface speaker diaphragm when there is no input vibration. The graph indicates that there was no displacement in the peak position which implies that the speaker surface is stable. The corresponding phase plot and the

calculated displacements are shown in the Figure 43 (b). The Figure 43 (b) indicates that there are some vibrations due to air or the optical table that amount to a maximum of 30 nm. The Figure 43 also shows that, the phase has a 21 Hz modulation as in 100 A-lines there is a periodicity of 2.1, and the frame captures 1000 A-lines per sec. Ideally, with no induced vibrations, no modulation in the phase profile should be observed. However, the results show a modulation of 21 Hz which is attributed to the environmental noise.

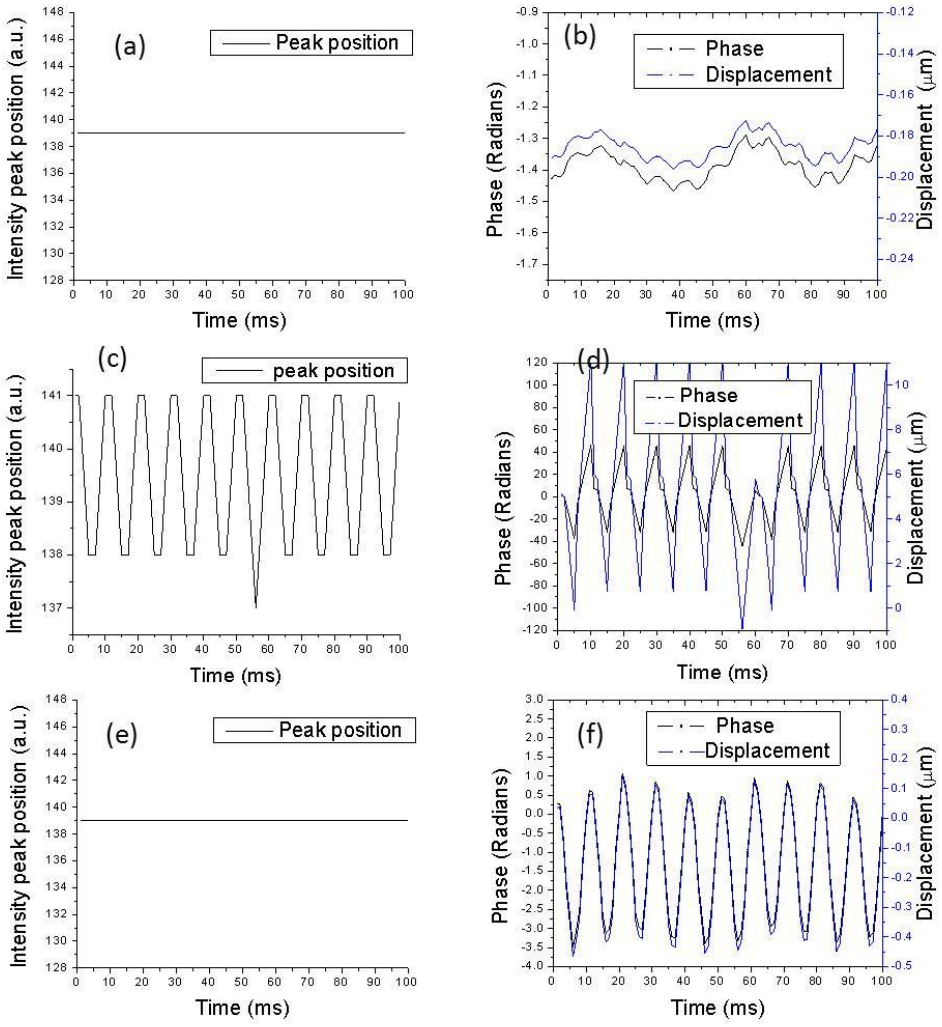

Figure 43: Vibrations of 100Hz induced on a speaker diaphragm. (a) Peak position when no vibration is applied. (b) Corresponding phase and displacement. (c) Vibrations of larger amplitude causing shift in peak position. (d) Corresponding phase and displacement. (e) Vibrations of smaller amplitude causing no shift in peak position. (f) Corresponding phase and displacement.

Now, large vibrations are introduced on the speaker surface. Figure 43 (c) depicts that large vibration amplitude (~ 4.5 μm) is reflected as a shift in peak position of the A-scan. The corresponding phase changes are plotted in the left y-axis of the Figure 43 (d). Displacement of the surface has been estimated from the unwrapped phase values using the Equation 13 and the unwrapping of the phase was done using the changes in the peak position. These displacement values are plotted on the right y-axis in the Figure 43 (d).

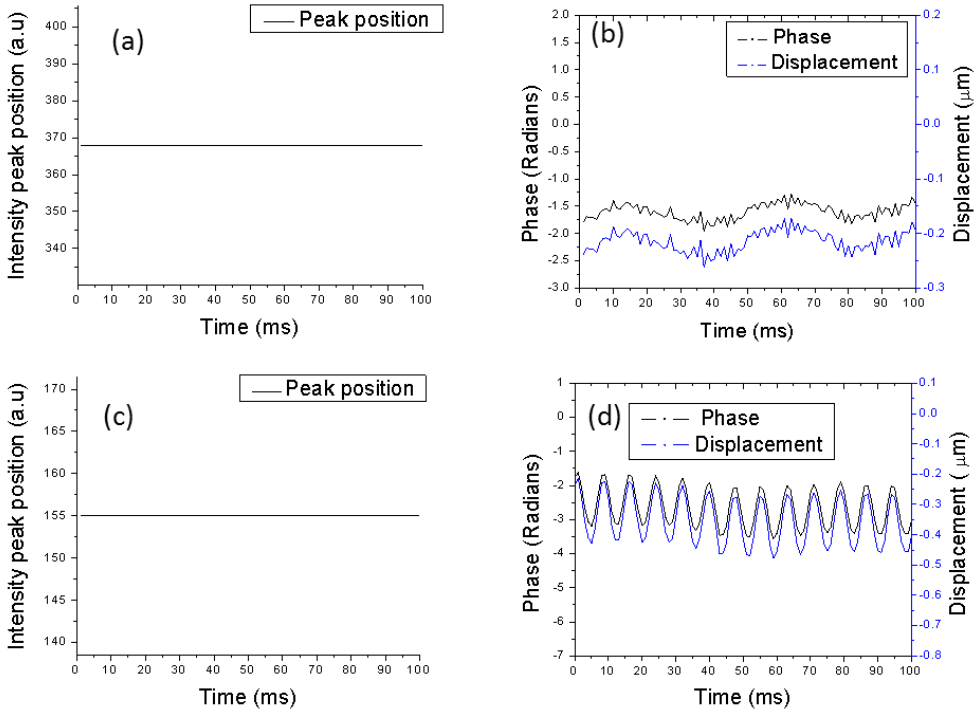

Figure 44: Vibration induced on a mouse eye lens. (a) No vibration (b) Corresponding phase and displacement. Phase showing 21 Hz noise. (c) Vibrations at 130 Hz of smaller amplitude causing no shift in peak position. (d) Corresponding phase and quantified displacement.

The calculated displacements show amplitude of 10 μm thus validating that the phase could be utilized to measure the vibrations. Figure 43 (e) shows the position of the diaphragm when vibrated with very small amplitude (~0.27 μm). As the pixel resolution of the system is 4μm, the vibrations cannot cause any shift in peak position, however, the corresponding phase response

shown in Figure 43 (f), shows changes due to displacement that was quantified with sub-micron precision.

Similar analysis was performed on the crystalline eye lens of the mouse. Eye lenses were extracted from adult mice and were placed in a container containing saline to prevent dehydration. The lenses were secured firmly to the base of the container preventing their mobility. Surface vibrations on the eye lens were induced using a wire-tapping method. A sinusoidal tone of 130 Hz was identified as the least noise affected region and hence the eye lens was excited using that frequency. M-mode scanning was performed while the external stimulus was applied and surface vibrations were quantified from the phase information using a similar method as used with speaker diaphragm. Figure 44 depicts the plots obtained for the vibrations induced on the surface of the mouse eye lens. Figure 44 (a) shows peak positions representing the case when there is no input vibration to the eye lens. Figure 44 (b) shows the corresponding phase. This phase shows a 21 Hz phase noise component which was discussed earlier. Figure 44 (c) represents the case when the vibration of very small amplitude is applied to the lens but it cannot be observed from peak positions. Figure 44 (d) shows that the phase is changing indicating that there is 130 Hz vibration of ~0.1 μm amplitude.

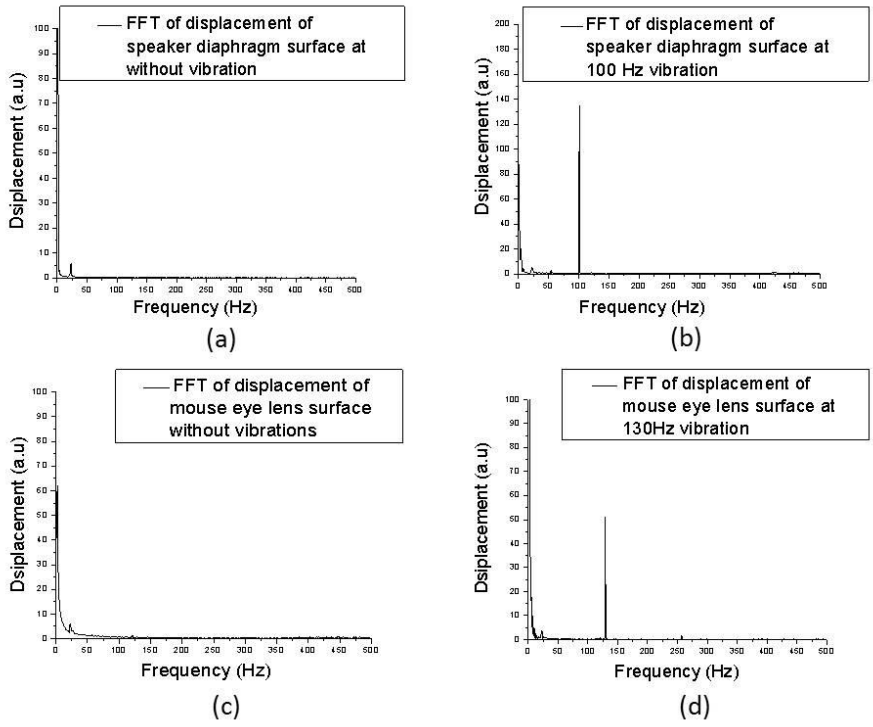

Figure 45: FFT of displacement of surface (a) Speaker diaphragm surface without vibration indicating noise at 23 Hz with amplitude of 0.012 µm. (b) Speaker diaphragm surface indicating 100 Hz with amplitude of 0.27 µm and noise at 21 Hz with amplitude of 0.01 µm. (c) Mouse eye lens surface without vibration indicating noise at 21 Hz with amplitude of 0.012 µm. (d) Mouse lens surface indicating vibration at 130 Hz with amplitude of 0.1 µm and noise at 23 Hz with amplitude of 0.007 µm.

Figure 45 depicts the plots obtained from FFT of the phase information to obtain the amplitude of vibration. All figures depict positive half of FFT, N/2 point corresponds to 500 Hz. Figure 45 (a) and (c) are FFT plot of the speaker diaphragm and mouse eye lens surfaces respectively, when no tone is played. They still show presence of a minor 21 Hz component. It can be inferred from Figure 45 (b) that, a frequency of 100 Hz tone was applied to the speaker diaphragm. Figure 45 (d) depicts FFT of the mouse eye lens surface when a 130 Hz tone was applied.

From the frequency analysis, the frequency of vibrations that falls under the least noise region is identified. For example, 60 Hz frequency was not chosen for exciting the sample as noise at

that frequency is higher. The results from surface vibrations of the speaker diaphragm indicate that OCT is sensitive to minute displacement and serves as a good tool to detect small vibrations of frequencies greater than 21 Hz and amplitudes up to an order of 0.1 μm. Since the system relies on phase sensitive measurements, it can be subjected to external conditions which are a major disadvantage of the system. For example, the 21 Hz component occurs in all phase plots and it is expected to be caused by the external environment. Since the system measures phase, it is subjected to 2π jumps and hence careful unwrapping needs to be performed. Measurement of vibrations of large frequencies can also be limited by the acquisition speed of the system as the phase will be subjected to multiple phase jumps which are very difficult to resolve. However, all the in vivo experiments were performed with small amplitudes where the phase wrapping does not cause a problem [208].

So far, the method for amplitude measurements under harmonic excitation was discussed. In order to calculate the surface wave velocities, two parameters are needed: the distance travelled and the phase delay. Distance travelled by the wave is the distance between the points where the wave is induced to the point where the measurements were made and the phase delay between the points gives the time taken for the wave to reach the points of measurements. Therefore, prior knowledge of location is required to measure the distance and time of excitation is required to measure the delays that allow velocity measurements. In case of harmonic excitation, the exact time of excitation can be measured only if the data is continuously recorded just before and right after excitation. This was not possible due to data saving limitation. PhS-SSOCE can record continuously only for 7 seconds before the internal buffer is filled. In addition to that, the wave excitation uses different software and the switching time from excitation software to the data acquisition software does not allow the saving of data continuously before and after excitation. Therefore, quantifying surface wave velocities was not feasible with harmonic excitation in our case. However, axial velocities could be quantified.

Axial velocities are measured from the time delay in the phase response between the two surfaces. However, in the continuous excitation case, both the top and bottom surfaces vibrate continuously. So, the optical path length between the surfaces keeps changing all the time. Therefore, the influence of path length change is reflected on the phase response on the second surface. For instance, if the top surface of the phantom is probed first, then the phase response at the bottom surface has the influence of both the actual physical dislocation of the bottom surface as well as the path length changes. Similarly, if the bottom surface is probed first, then the phase response on the top surface contains the actual dislocation of the top surface due to the wave propagation and the optical path length changes. However, the phase response due to the actual physical dislocation of the surface is only required. To remove the effect of path length changes, the following mathematical corrections were made.

The probing beam and induction of waves were placed on opposite sides of the phantom as explained in the experimental procedure. In the inverted sample arm position, the beam is focused on the bottom surface of the phantom first and then the top surface while vibrations were induced only on the top surface of the phantom.

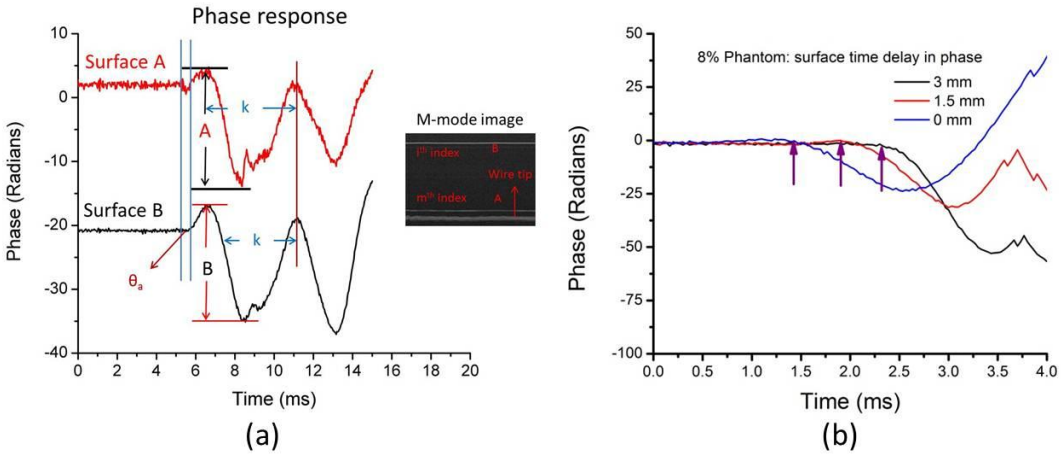

Figure 46: a) Phase response at both surfaces with labeled parameters (b) delay in phase response with increasing distance.

In this way, the measurements at both the top and bottom surfaces can be taken right at the point where vibrations are introduced. In this configuration, the top surface in the image corresponds to the bottom surface of the phantom and vice versa. Let A and B represent the top surface and the bottom surfaces of the phantom. The phase responses at A and B are shown in the insert of Figure 46 (a) and can be represented as;

$$A: \ A\ \cos(kt + \theta_a),$$

$$B: \ B\ \cos(kt + \theta_b),$$

Equation 14

where A and B are the amplitudes of the phase responses observed at the top surface and the bottom surfaces respectively, k is the frequency observed, θ_a and θ_b are the observed phase delays. As the frequency does not change during propagation, k remains the same for both the surfaces (verified experimentally). As the 1st measurement is at surface B, let us consider the phase wave at B as a reference. Then, $\theta_b = 0$; the beam passes through surface B to reach surface A. Hence, the phase response at surface A includes the phase responses because of the physical translocation of the surface due to the mechanical wave and also because of the path difference introduced due to the physical translocation of the wave at the surface B. As the latter phase is not because of wave propagation, it would not introduce any delay. Hence, the phase response at A can be written as,

$$A: \ A\ \cos(kt + \theta_a) = \ A_1 \cos(kt + \ \theta_1) + B^{'} \cos(kt),$$

Equation 15

where A_1 is the amplitude of the mechanical wave at the surface A, B' is the amplitude of the phase response carried due to the path difference introduced at the surface B. θ_1 is the required parameter which is the delay due to the propagation of the mechanical wave. Ideally, B' should

be equal to B. However, due to the dependence of phase on depth index B' is not equal to B. B' can be obtained from B and the difference in depth index from the following equation,

$$B' = B - \frac{i}{m}.A,$$

Equation 16

where *i*, *m* are the depth indices corresponding to the surfaces B and A respectively.

Solving Equation 15, we get

$$\cos(kt + \theta_a) = \frac{A_1 \cos(kt)\cos\theta_a - A_1 \sin kt \sin\theta_a + B'\cos(kt)}{A},$$

$$\cos(kt + \theta_a) = \frac{(A_1 \cos\theta_a + B')\cos(kt) - (A_1 \sin\theta_a)\ \sin kt}{A},$$

$$\mathrm{Cos}\ (\mathrm{kt}\ +\ \beta) = \frac{\mathrm{A}}{\mathrm{A}^2 + \mathrm{B}'^2 - 2\mathrm{AB}'\mathrm{Cos}\ \theta_a}\cos(kt + \theta_1),$$

Equation 17

where $\tan\beta = \frac{A\ Sin\ \theta_a}{A\cos\theta_a - B'}$. Therefore, $\theta_1 = \tan^{-1}(\frac{A\ Sin\ \theta_a}{A\cos\theta_a - B'})$.

By knowing the parameters A, B' and θ_a , as well as the thickness of the phantom, the velocity of the wave was calculated. Therefore, in this subsection, a method to quantify vibration amplitudes and axial velocities under harmonic excitation has been discussed. As it was noticed that, harmonic excitation does not provide the wave information during the dynamic response of the sample. Hence, this type of excitation is classified as static excitation.

4.3.2 Pulsed Excitation

The other type of excitation is to excite the sample with a single tap that lasts for a finite duration of time. For such kind of excitation, a pulse signal generated from a signal generator was

applied to the excitation unit rather than a sinusoidal signal. With the onset of the pulse, the sample surface is displaced and with the removal of the pulse, the sample starts to vibrate with its natural frequency. Therefore, in this type of excitation, the dynamic response of the tissue could be measured. Hence, this type of excitation falls under dynamic excitation mode.

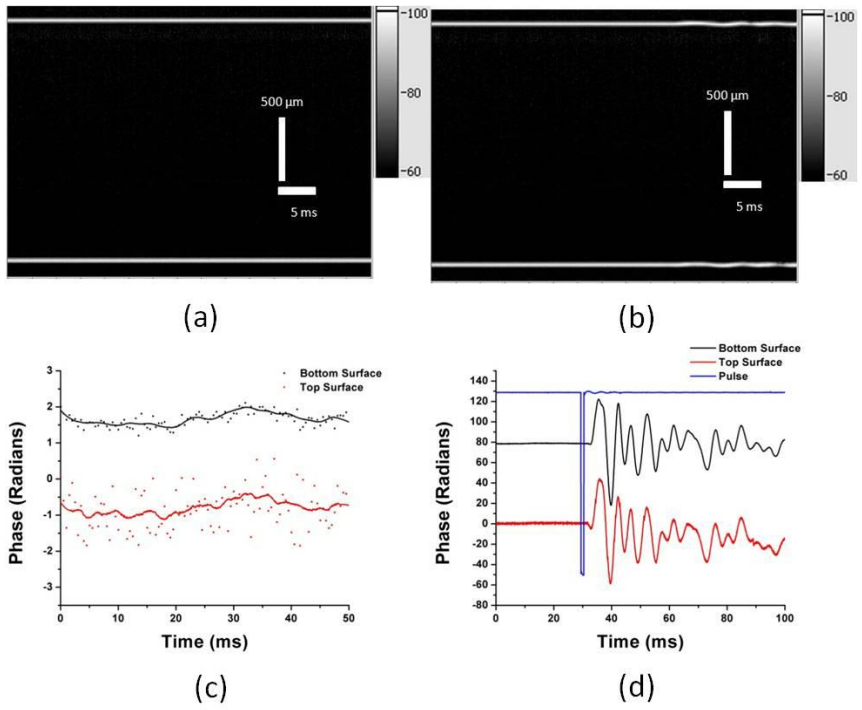

Figure 47: M-mode images (a,b) and corresponding temporal measurements of phase of OCT signal (c,d) acquired at the surface of (a,c) stationary phantom (*i.e.*, phantom was not subjected to any external mechanical excitation) and (b.d) phantom before, during and after the application of localized mechanical excitation at the surface.

Absolute amplitudes and axial velocities were measured in the similar manner as for the harmonic excitation. With pulsed excitation, quantification of shear wave velocities could also be performed. Shear wave velocities were quantified from the time delays observed in the phase response at various measuring points from the M-mode images (Figure 46 (b)). Figure 47 (a) and (b) show the M-mode images of the phantom within excitation and before, during and after the mechanical excitation, correspondingly. Both surfaces of the phantom could be seen in M-mode

images. The phases are nearly constants with insignificant variations when the sample is not excited as shown in Figure 47 (c). However, when mechanical excitation is applied externally, phases at the boundaries change as shown in Figure 47 (d).

Amplitude of induced displacements is low and hardly noticeable in M-mode image (Figure 47 (b)). To obtain the time delay, the pulse used to excite the sample was simultaneously recorded at the second channel of ADC. The delay between the generation of the excitation pulse and the wiretapping was recorded using the following procedure: the imaging objective in the sample arm was inverted such that the wire can be imaged directly through the phantom allowing direct monitoring of the wire from the image. The phase response at the point of tapping on the top surface of the phantom gives the exact time of excitation as shown in the Figure 47 (d). The blue trace in the Figure 47 (d) shows the time of occurrence of the pulse to excite the phantom. The red and black traces are the phase responses at the top and bottom surfaces of the phantom at the point where the wire touches the phantom surface. The time delay between the occurrence of the pulse and the phase response gives the total time taken for the pulse to excite the speaker diaphragm and the wire. All the delay measurements were performed relative to the pulse.

4.4 Validation of the method: phantom studies

To evaluate the system and the method of quantifying, the wave parameters were measured in phantoms of known stiffness behavior. The methods were evaluated for all three types of excitations described in this dissertation and the validation was performed on phantoms, *ex vivo* and *in vitro* mice eyes. And after validation of the method, it was applied to *in vivo* studies.

4.4.1 Harmonic Excitation

Experimental evaluation of the method with harmonic excitation was performed in gelatin phantoms by constructing 2D maps of wave propagation. This was achieved in two phases: first

with a phantom to validate the capability of the PhS-SSOCE system to measure the propagation of waves and second is to measure the change in propagation of the waves with a metallic insertion.

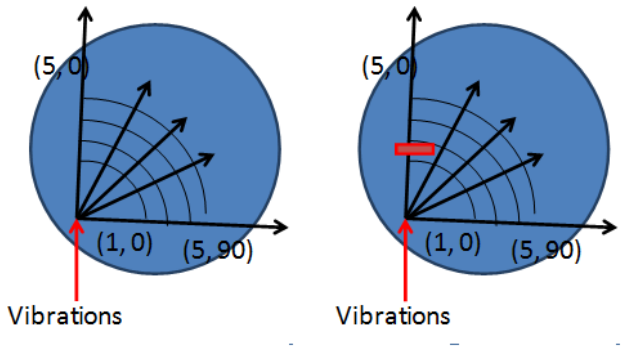

Figure 48: Cartoon of the phantom showing the points of measurements.

A phantom of thickness of approximately 2 mm was prepared in a petri dish (base thickness 1 mm) using 4% gelatin. The wiretapping method was used to induce mechanical waves on the surface of the phantom at the origin of the r-theta plane. Vibrations were measured at five radial distances from the location of tapping at angles 0, 30, 45, 60, and 90 degrees respectively with an increment of the radius by 1 mm as shown in the Figure 48.

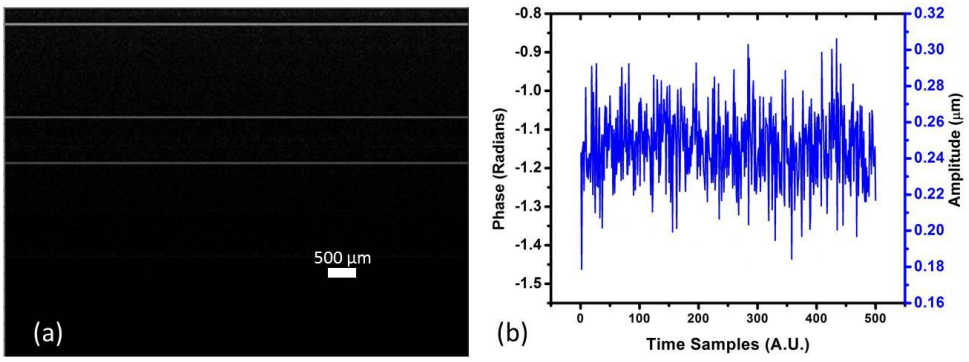

Figure 49: (a) m-mode image of the phantom (b) real time phase response at the surface of the phantom.

The M-mode image of the phantom is shown in the Figure 49 (a). The image shows three bright lines, where the top most trace is the top surface of the phantom, central bright line corresponds to the phantom-petri dish interface and the last one is the bottom surface of the petri dish. The real time phase response at the phantom surface is shown in the Figure 49 (b). The figure shows that the phase response is stable as there were no vibrations induced yet. However, the figure shows amplitude of less than 30 nm at a frequency of 60 Hz. This is attributed to electronic noise component. Phase stability of 0.09 radians is observed in this phantom as opposed to 0.01 radians on a glass slide. This reduction in the phase stability is due to the fact that there are many minute scattering particles (due to gelatin) which could not be seen in the image that are introducing phase noise. Due to the presence of phase noise, vibrations less than 30 nm at frequencies other than 60 Hz cannot be detected by the PhS-SSOCT.

Low amplitude vibrations of 400 Hz were introduced using the same procedure discussed earlier and the phase response was observed at the both top and the bottom surfaces. The amplitude of vibrations was so low that they cannot be observed in the structural. Therefore, no phase wrapping is observed.

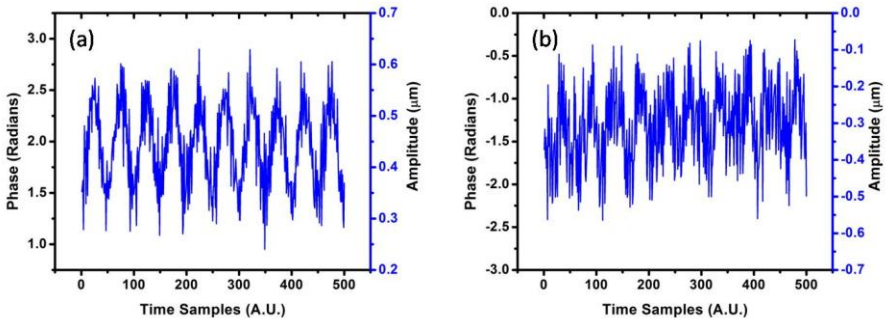

Figure 50: Phase response of the Phantom with vibrations introduced (a) at the top surface (b) at the bottom surface.

The phase response at both the top and the bottom surfaces were shown in the Figure 50 (a) and (b) respectively. The top surface shows the amplitude of vibrations around 0.35 μm whereas

the bottom surface shows around 0.22 µm. Since the frequency of the phase response in the bottom surface is the same as the top surface, it can be validated that the phase response observed is due to the wave rather than a superposition of many reflected waves. For instance, both the surfaces show a frequency of 400 Hz (for a 20 kHz laser sweeping speed, 500 A-lines are obtained in 25 ms) indicating the absence of multiple wave reflections from the walls of the petri dish at the time of measurement. If there is a superposition, then phase response should indicate the presence of multiple frequencies or at least the beat frequency which is not the case. Hence, the bottom surface phase response gives us the information of the influence of the wave on the top surface.

To evaluate the wave propagation over the distance from tapping, the amplitudes of vibrations were measured at different 2-D spatial points as described in the procedure and the contour plot has been utilized to show how the amplitude of these vibrations damp with respect to the distance. Figure 51 show the propagation of the wave along the 2-D space.

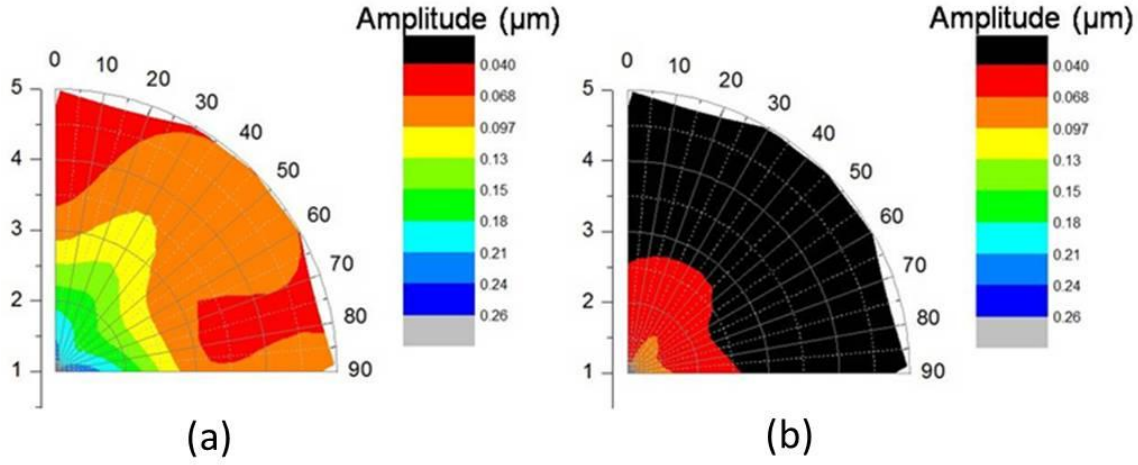

Figure 51: Wave propagation at the (a) top surface (b) bottom surface.

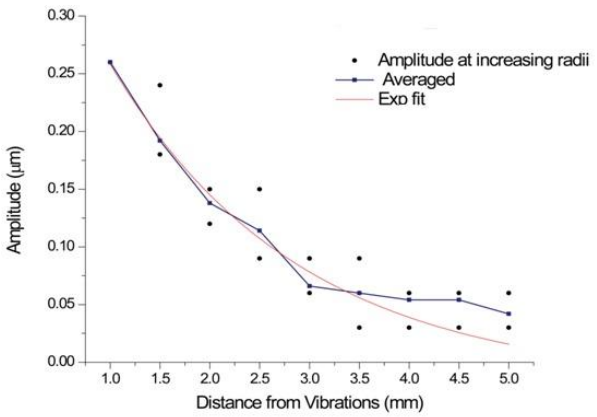

Figure 52: Evaluation of amplitude with respect to the lateral distance from the point of tapping.

The vibrations were induced at radius 1 mm. The figure clearly depicts the radial propagation of the wave as well as the drop in amplitude with the increase in distance from the tapping point (radius). The average damping of the wave along the distance for the same angle for the top surface of the phantom was measured as shown in the Figure 52. The graph clearly depicts that there is an exponential decay in the amplitude with the increase in the distance which is in accordance with the conventional theory of damping.

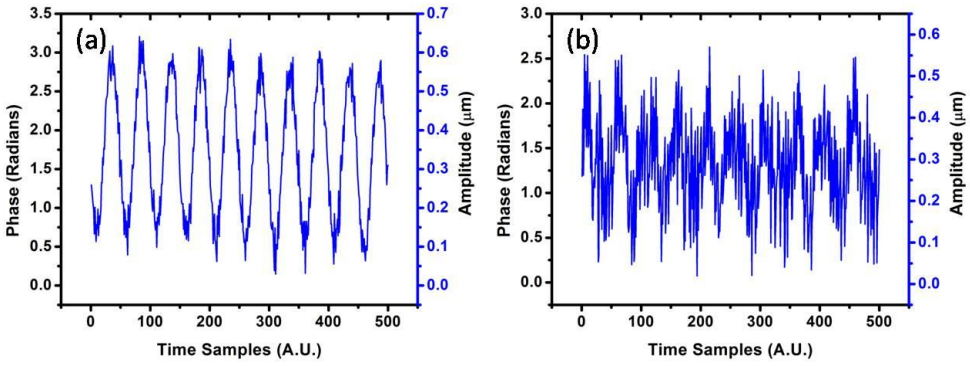

Figure 53: Phase response after the metallic insertion at (a) top surface (b) bottom surface.

To evaluate the system to see if the system can pick minute changes in the wave propagation, a metallic insertion was placed between the point of vibrations and the point at which the beam is

probed as shown in the Figure 48 (b). The insertion was placed parallel to the surface and was at a depth of 1 mm from the surface of the phantom. Now, the phase response at the top and the bottom surfaces were measured. Figure 53 shows that the real time phase response at the top and bottom surface of the phantom. The Figure 53 shows that the phase responses become more prominent due to the metallic insertion.

The contour plots, shown in the Figure 54 (a) and (b) indicate that, the insertion helps in increasing the amplitude initially but the wave damps more at farther distances, we see that, the amplitude has enhanced for all the values at 0 degrees as the insertion was lying there. Also, along 90 degrees, the wave is reflected and has got a 180 degree phase shift and hence the amplitude was reduced right from the 1 mm radius. With the insertion, the top and bottom surfaces of the phantom recorded vibrations of amplitude 0.5 µm and 0.36 µm. The contour plots suggest that, the amplitude of the wave damped from 0.26 µm to 0.09 µm along the path that contains the metallic insertion when compared to 0.26 µm to 0.06 µm when there is no metallic insertion. This result clearly indicates that the metallic insertion is in fact enhancing the signal. The results also suggest that, PhS-SSOCE can measure very minute harmonic vibrations up to amplitudes 30 nm.

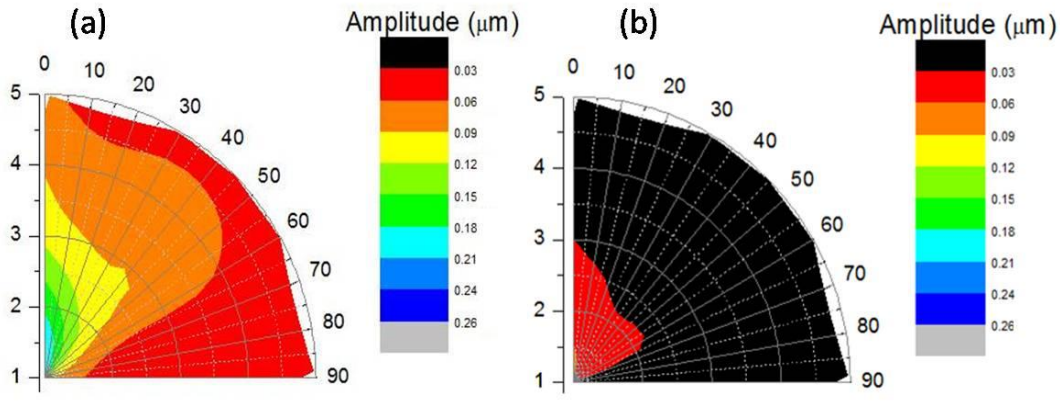

Figure 54: Wave propagation on the (a) top surface (b) bottom surface of the phantom with insertion.

4.4.2 Pulsed Excitation

In pulsed excitation mode, spatial amplitude damping as well as surface velocities was quantified as described in the previous section. The method to measure velocities is evaluated for all three different types of excitation discussed earlier.

The PhS-SSOCE used for these studies is shown in the Figure 55. Mechanical waves were introduced on the phantom surface using the wire-based mechanical excitation unit described earlier. The excitation points and measuring points are shown in the insert in Figure 55 (red and blue dots respectively). Waves propagated in all directions creating internal and surface displacements in the phantom. The displacements were recorded at several points spaced 1 mm from each other shown in the insert in the Figure 55 (blue circles). Velocity was calculated by measuring the temporal characteristics of the induced mechanical waves as described in section 4.2.

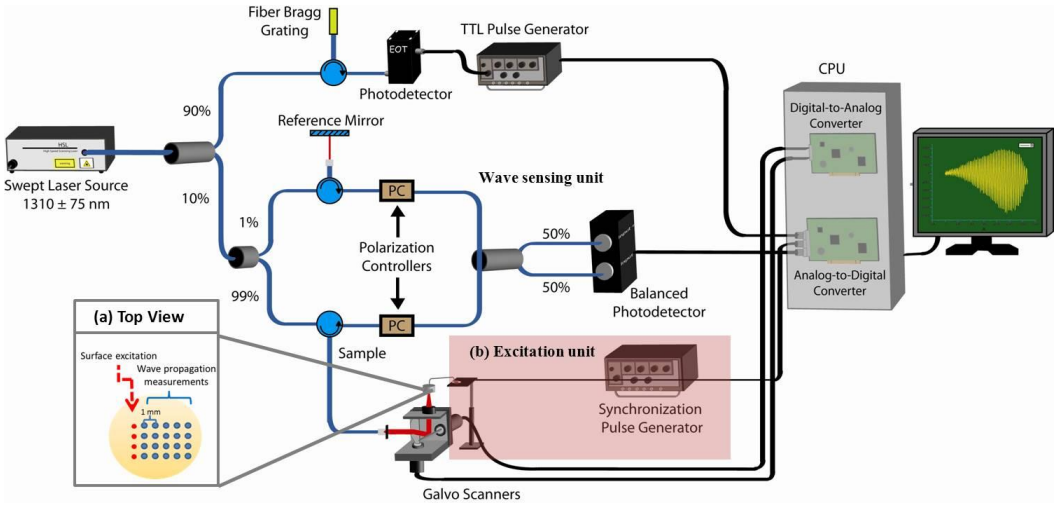

Figure 55: Schematic of the experimental system based on phase-sensitive swept-source OCT. Insert (a) shows the top view of the phantom surface indicating the location of surface excitation (red dots) and wave propagation measurements (blue dots). Insert (b) shows the source of excitation.

In order to simulate soft tissue samples of controlled stiffness, gelatin phantoms with varying concentrations (8-16% w/V) were prepared. Gelatin (P8 Gummi gelatin 250 Bloom, RB Leiner) was mixed with water at 60°C until all granules were dissolved. Care has to be taken while stirring the mixture to avoid bubbles from forming in order to avoid changes in wave propagation due to bubbles in the phantom. The mixture was poured into a mold to create ~1 mm thick layer, and cooled in the refrigerator for 30 minutes (~ 10°C) [209]. The solidified gel formed a solid slab that served as a tissue mimicking sample. It is known that the higher is the gelatin concentration, the greater is the stiffness of gel. We verified the elastic properties of the samples using the uniaxial stress-strain measurements performed using In-Spec 2200 (Instron, Inc., Norwood, MA).

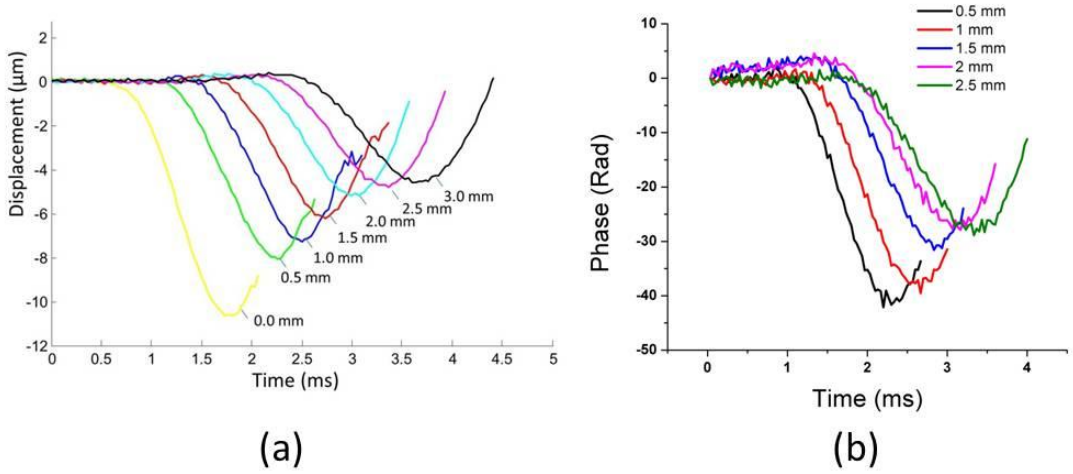

Figure 56: Phase responses recorded at various points located 0 mm to 3 mm away from the source of excitation in (a) 8% (b) 10% gelatin phantom.

Figure 56 depicts typical phase responses collected at increasing distances from the point of excitation in 8% and 10% phantom. The results clearly demonstrate attenuation of the wave amplitude as it propagates on the surface of the phantom away from the excitation point. In addition to the wave atttenuation, the time delay for the wave reaching different locations could

be used to calculate wave velocity. For example, in Figure 56 (a), there is a time delay of ~0.28 ms between the phase responses recorded at 1 mm and 0.5 mm that gives the velocity of 1.7 m/s.

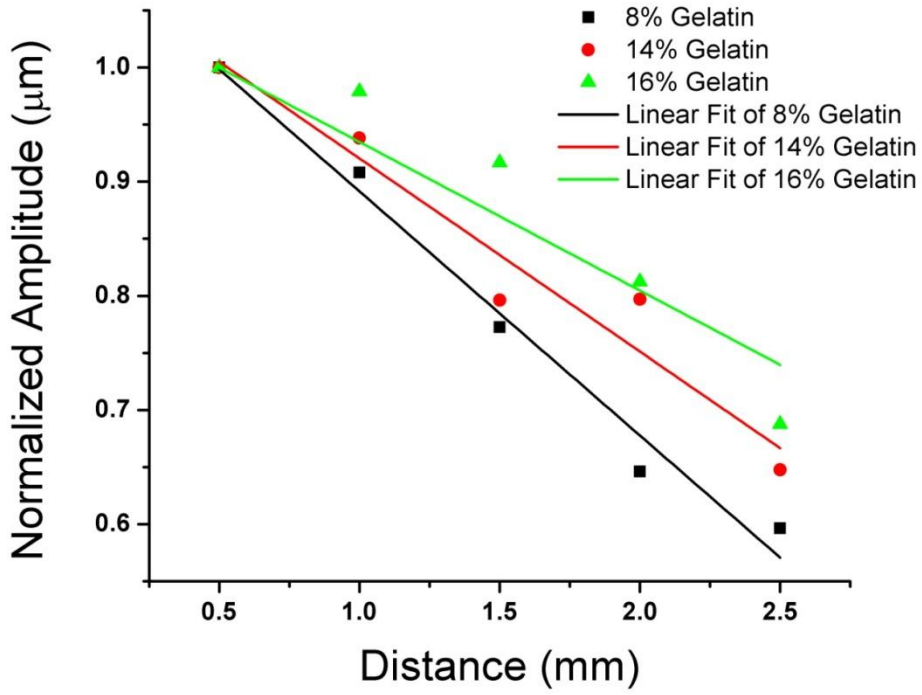

Figure 57: Amplitudes of the wave recorded at increasing distances from the source of excitation.

The attenuation of the wave amplitude with the increasing distance from the point of wave excitation for 8-16% gelatin concentrations is shown in Figure 57. As expected, the wave amplitude decreases with the increasing distance from the point of tapping for all phantoms. The amplitude of the wire motion was not controlled in the experiments; therefore the initial amplitude at zero position was an arbitrary value. The combination of measurements of the wave's amplitude attenuation together with its velocity could be used to attain viscoelastic properties of the sample.

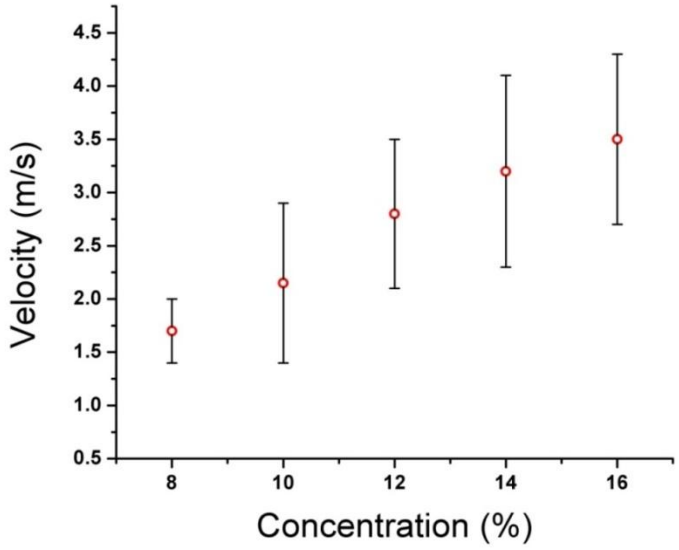

Figure 58:Shear wave velocities measured at the surface of the 8% - 16% gelatin phantoms. The bars represent the standard deviation with N= 3.

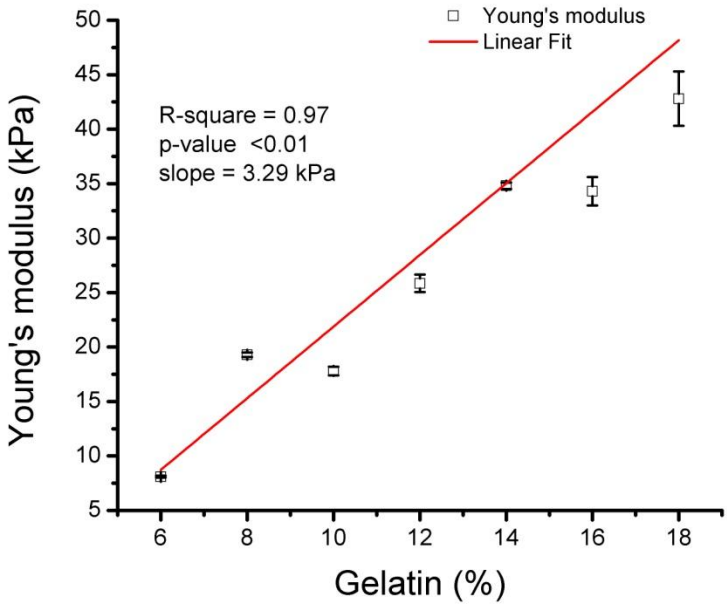

Figure 59:Young's modulus vs gelatin concentration obtained using uniaxial tests.

The velocity of the propagating surface shear waves in phantoms with varying concentration of gelatin is shown in Figure 58. The values shown represent the velocities averaged over a 3 mm range. Clearly, as depicted in Figure 58, shear wave velocity increases with the increase in gelatin concentrations. Increase in gelatin concentrations correspond to the increase in the Young's modulus of gelatin which was validated by direct stress-strain measurements using the In-Spec 2200 portable system as shown in Figure 59. Figure 59 depicts that there is a linear increase in Young's modulus with a linear increase in gelatin concentrations. Combining these results with the velocity measurements, it can be concluded that the velocity of the wave is higher in materials with higher Young's modulus of elasticity. Thus, the results presented in this section demonstrate that the PhS-SSOCE elasticity imaging method is capable of quantifying shear wave velocity and, therefore, shear or Young's modulus of the tissue.

The accuracy of the described method for quantification of amplitude and speed of the mechanical wave depends on phase-stability of the system and signal acquisition speed, respectively. The results in this section clearly demonstrate the possibility of quantification of low-amplitude (micrometer-scale) mechanical waves with the possibility to go down to nanometer scale. However, the signal acquisition speed of the described SSOCT system is 30 kHz which limits detection of high frequency waves generated on the surfaces of the cornea. Therefore, incorporating higher speed swept laser sources would increase the accuracy of the wave characterization.

Evaluation of the method for ultrasound excitation was performed in the similar manner as for the wiretapping excitation. However, the phantoms were prepared using silicone rubber rather than gelatin due to the fact that silicone is more responsive to US than compared to gelatin. Silicone rubber (Elastosil RT601, Wacker solutions) phantoms were prepared using 8:2 and 6:4 mixing ratios of silicone and oil, the optimum concentrations as specified by the supplying company. The Young's modulus of the two phantoms was measured using Instron stress strain

measurements which showed that the 8:2 phantoms are stiffer than the 6:4 phantoms (Figure 60 (d)). As it is known that the velocities in stiffer phantoms is higher, by comparing velocities in these phantoms provides a proper evaluation of the method.

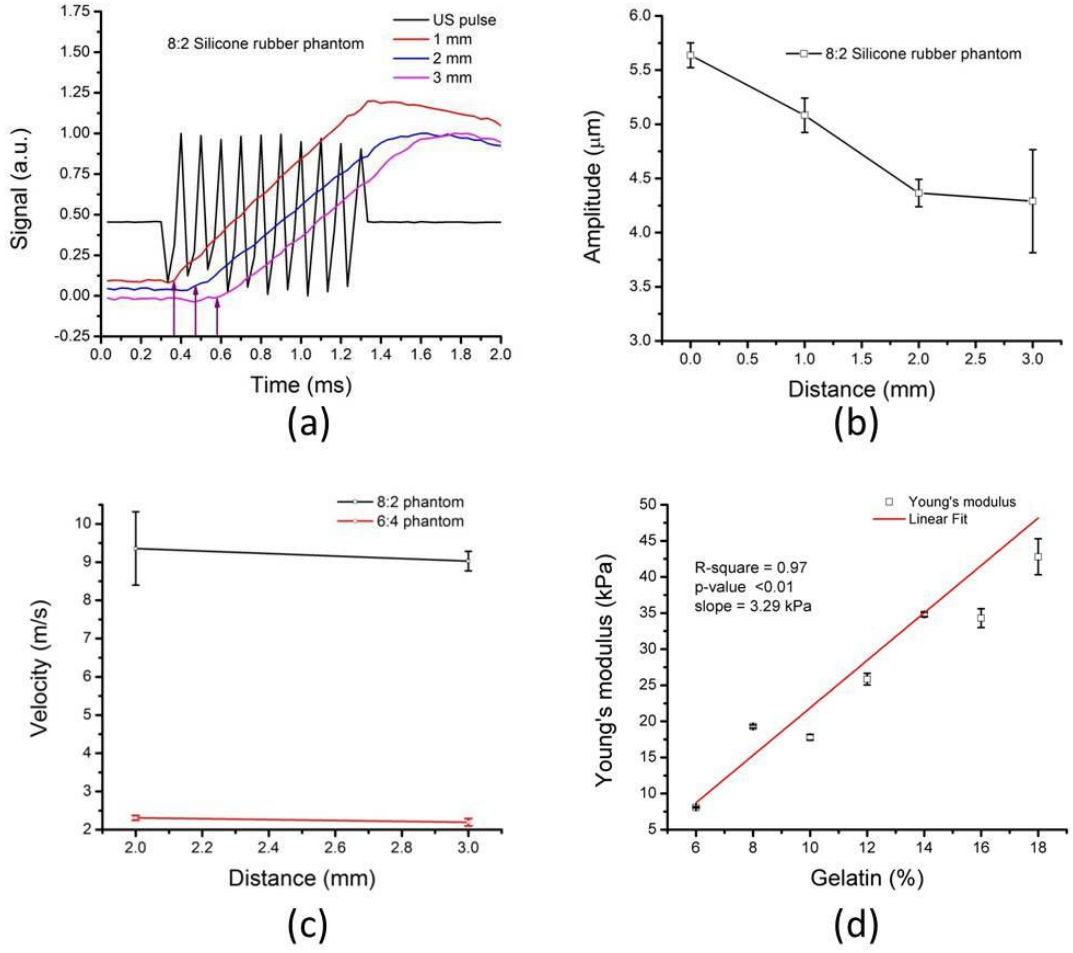

Figure 60: (a) Synchronization between the pulse causing vibrations and the phase response at the surface of the phantom (b) Normalized amplitudes vs. distance from the point of tapping (c) Surface wave velocity distribution of rubber phantoms of 80% and 60% concentrations (black and red respectively) over the distance from the US focal point (d) Relationship between Young's modulus and silicone concentration.

The PhS-SSOCE utilized for the experiments is shown in the Figure 41. The ultrasound transducer was focused at the surface of the phantom from the top and the imaging was performed from the bottom. The inverted sample arm allowed us to perform wave excitation and

imaging simultaneously at the ultrasound focal point. At the US focal point, the maximum phase is registered and the measurements were performed at 1 mm- 3mm away from this point as shown in the insert (a) of Figure 55. The excitation unit as depicted in Figure 41 is responsible for generating low amplitude mechanical waves on the sample surface. It consists of a signal generator that generates a 7.5 MHz sinusoidal wave which is fed to a 7.5 MHz ultrasound transducer focused at the surface of the phantom. The ultrasound waves propagate all over the sample and are imaged by the sensing unit.

The signal given to the ultrasound transducer and the phase responses at 1 mm, 2 mm and 3 mm distances away from the US focal point are shown in the Figure 60. The Figure 60 (a) clearly shows the attenuation of wave amplitude and delay in the phase responses with the increase in the distance from the point of excitation. As described previously, this delay was utilized to measure the velocity. The amplitudes of the vibration induced by US over the surface were plotted in Figure 60 (b) as a function of distance from the point of wave induction. The figure clearly depicts the attenuation of wave amplitude with the increase in distance. The surface wave velocities were calculated using the same method described for wiretapping method. Surface velocities for 8:2 and 6:4 phantoms were shown in Figure 60 (c) in black and red respectively. The x-axis shows the distance from the US focal point and the y-axis shows the surface wave velocities. The results depict that surface velocities are higher in phantoms with higher concentrations. Results from the Insron stress strain measurements showed that higher concentrations correspond to higher Young's modulus (Figure 60 (d)) similar to the gelatin phantoms. Therefore, the wave velocity is higher in silicone phantoms with the higher Young's modulus.

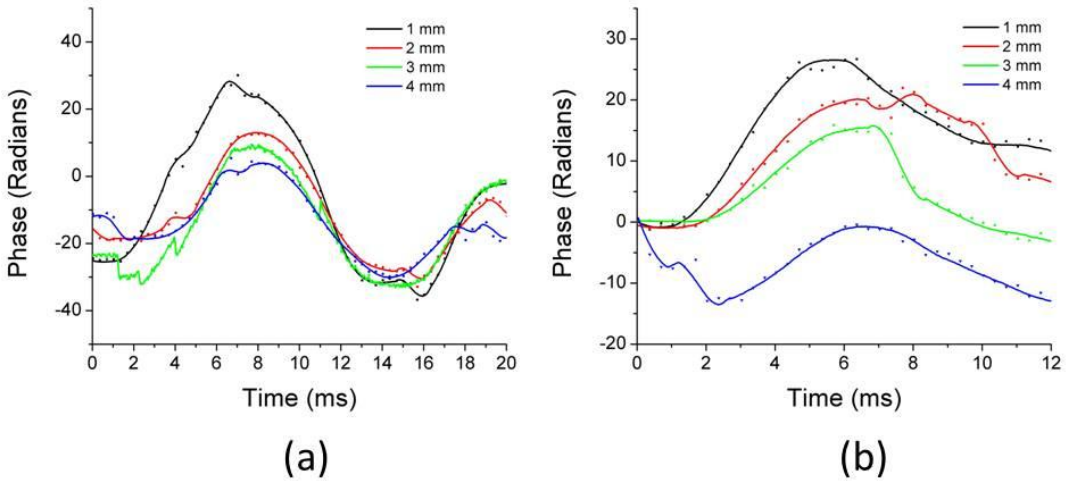

Figure 61: Phase responses to an airpuff stimulus (a) 12 % (b) 8% Gelatin.

The method for quantifying velocities was also verified for excitation of the surface with an air puff on gelatin phantoms. The experiments and the quantifying method followed the same procedure as for the wiretapping. The phase responses at increasing distances from the focal point of the airpuff are shown in Figure 61 (a) and (b) for 12% and 8 % gelatin concentrations respectively. Figure 61 depicts both the attenuation of the wave as well as the delay with the increase in distance from the excitation point.

The wave velocities were calculated from the delay and the distance between the measuring points similar to the air tapping and US excitation methods. The velocities were measured for gelatin concentrations from 8% to 16% and are shown in the Figure 62. The velocities increase with the increasing concentrations and also the absolute values are very close to the values obtained with wire tapping. The consistency in the result further advocates the capability of both PhS-SSOCE and the quantifying method.

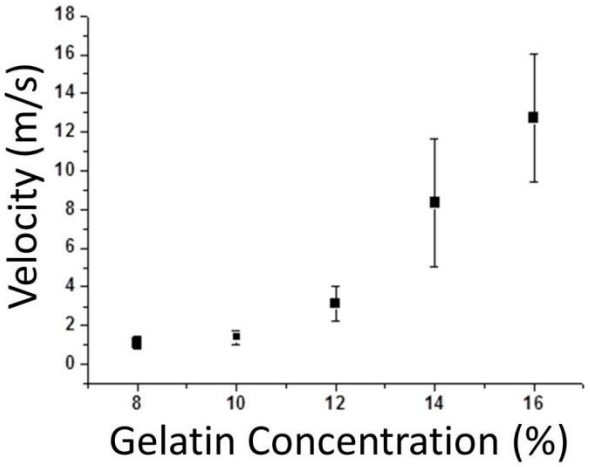

Figure 62: Velocity Vs Gelatin Concentration.

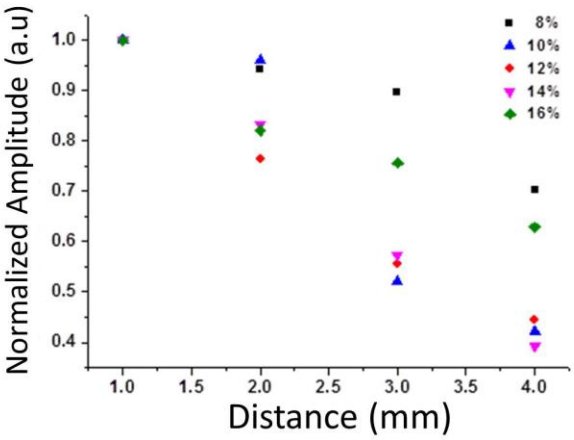

Figure 63: Amplitude vs distance for all Gelatin concentration.

The amplitude damping was also computed to further clarify the validation of the system and the method. Figure 63 shows the damping of wave for each concentration. Results again depict that the amplitudes are dropping with the increase in the distance from the airpuff focal point. Therefore, PhS-SSOCE combined with the quantifying method becomes an effective tool to study the wave propagation in biological samples.

The above results suggest that PhS-SSOCE offers a perfect tool to measure the wave parameters. However, there is a limitation in the range of velocities that can be measured by the system. The temporal resolution of our system is ~ 33 μs and therefore the smallest delay the system can measure is 33 μs. Therefore, in a sample of 1 mm thickness, the maximum velocity our system can measure is 30 m/s. With the maximum imaging depth of 4.5 mm, the system can measure a maximum velocity of 136 m/s provided that the samples are 4.5 mm thick. The wave attenuation and velocity information could be potentially be utilized to construct 2D stiffness maps. Therefore, with our method soft materials with different hardness values can be identified. Moreover, with the implementation of a model that can quantify stiffness, mechanical properties of the phantoms could be calculated.

4.5 Ex-vivo studies

After validating the method in phantoms, the PhS-SSOCE was applied to study the wave propagation in mice crystalline lens *ex-vivo.* The main aim of this section of studies is to verify whether the PhS-SSOCE combined with the phase resolved method to estimate wave propagation could be utilized in weakly scattering samples such as crystalline lens immersed in saline solution. The refractive index of saline solution and crystalline lens are nearly the same and therefore the signal from the crystalline lens surface is very weak. Phase resolved methods are very sensitive to the signal strength as the phase noise depends on the intensity of the signal. Therefore, *ex-vivo* studies were conducted in the crystalline lens of the mouse eye and the results suggest that the method is very effective even in weakly scattering samples.

This subsection of the dissertation describes the sample preparation, experimental procedure, results and discussion pertaining to the measurement of surface wave propagation in mice corneas *in situ* as a function of age.

4.5.1 Sample preparation

Eye lenses were dissected from mouse eyes, placed on a substrate and immersed in saline to maintain the physiological hydration conditions.

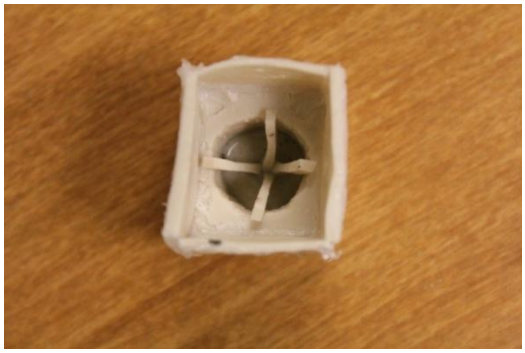

Figure 64: Substrate for imaging isolated crystalline lens.

The substrate was made of four rubber pads with chipped edges to keep both surfaces of the lens (anterior and posterior) free from contact with the walls as shown in Figure 64. The substrate design also allows the flexibility in fitting the crystalline lens of any size. The base of the substrate was fixed to the optical table using a double sided tape to reduce the vibrations. The sample arm was adjusted for the best focus before imaging.

4.5.2 Experimental procedure

Vibrations were induced on the lens surface using the wiretapping method. The vibrations were measured at 21 different spatially distributed points beginning from the one end of the lens to the other as depicted in Figure 65. Figure 65 depicts the 3-D cartoon representation of the crystalline lens and the dark dots indicate the points of measurements. Imaging was performed in all the modes namely, 3-D, 2-D and the m-mode. The thick arrow shown in the 3-D image indicates the point of introduction of vibrations.

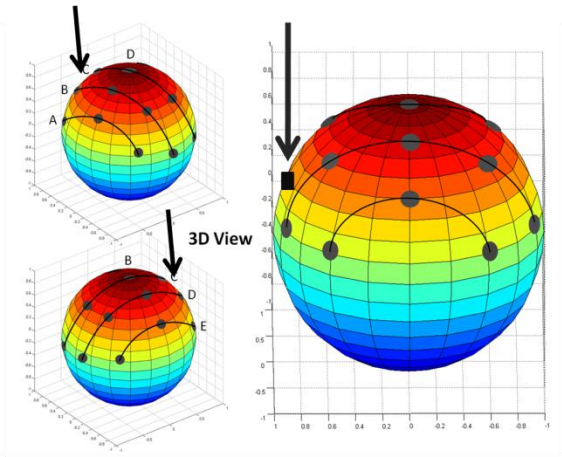

Figure 65: Cartoon representation of the crystalline lens and the positions where the vibrations are introduced and measurements made.

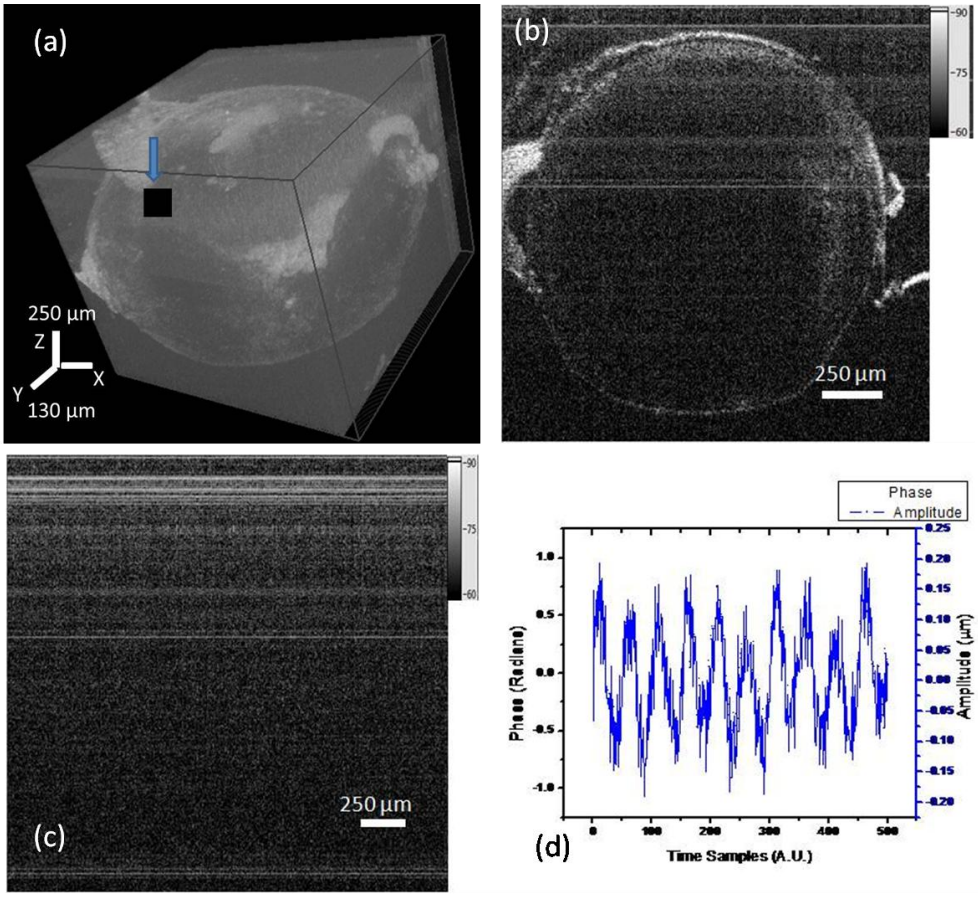

Figure 66: Crystalline lens: (a) 3-D reconstruction (b) 2-D structural image (c) M-mode image (d) phase response to vibrations.

M-mode images were obtained at three locations on each of the extreme sides and five measurements in each of the middle three scans consisting all together as 21 points. The m-mode image shows two lines each corresponding to the posterior and the anterior surface of the lens as shown in Figure 66. The distance between these lines in the image correspond to the distance between both the surfaces of the lens. The distance between the top and bottom surface of the eye lens is very small at extreme ends but it is maximum at the center. This distance was utilized to maintain the symmetry among all the measurements while conducting the experiments. Amplitude measurements were made from the phase extracted from these M-mode images as explained in the section 4.3.1 and the contour plots were plotted at both anterior and posterior surfaces of the lens.

4.5.3 Results

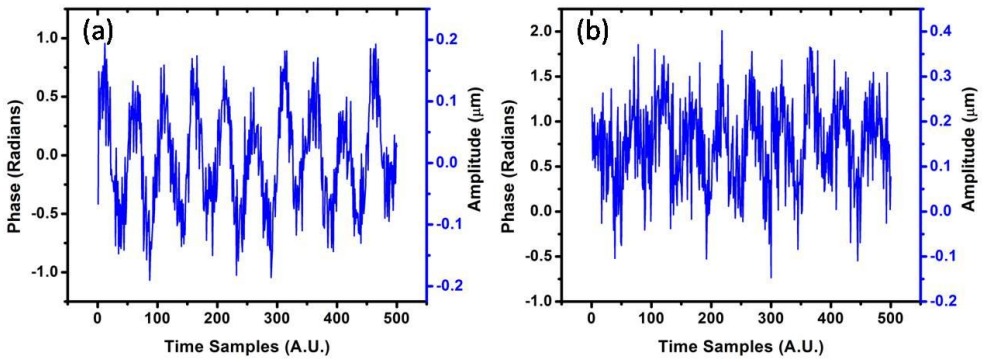

Figure 67: Vibrations recorded on the Crystalline Lens at (a) anterior surface (b) Posterior surface.

The Figure 67 (a) and (b) show the phase response of the anterior and posterior surface of the lens. As the vibrating point is closer to the anterior surface, highest amplitude of 0.25 μm was recorded. The posterior surface phase was very noisy, however, the signal could still be extracted and the displacement of 0.15 μm was recorded. The drop in amplitude is due to the damping of the wave from the anterior surface to the posterior surface.

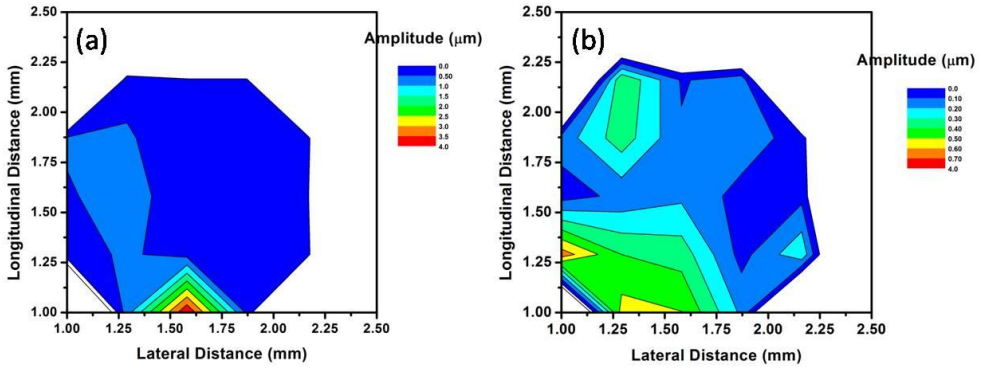

Figure 68: 2D distribution of wave amplitude on (b) anterior surface and (c) posterior surface of the eye lens.

2D contour plots were constructed from the amplitude distribution of the wave. In the 2-D contour plots, the point of vibration was at 1.6 mm in the lateral direction is depicted in Figure 68. It can be noted that the amplitude completely attenuated within 0.15 mm distance in the lateral direction whereas longitudinally, it sustained for 0.25 mm. This asymmetric attenuation of the wave along the lateral direction and longitudinal direction suggest that the lens stiffness is not uniformly distributed. Vibrations were observed at 1.6 mm lateral distance on the posterior surface of the lens suggest that the wave did not attenuate completely even after travelling the distance equal to the diameter of the lens which was ~ 0.5 mm. Therefore, the wave sustained for a longer distance inside the lens when compared to the surface. This result shows that the propagation of the waves was faster inside the lens than on the outer surface of the lens. Moreover, the Figure 68 (b) shows a little higher amplitude at (1.25, 2.0) co-ordinates in the contour plot. These co-ordinates correspond to the longer areal distance (and hence inside the lens) compared to other co-ordinates on the periphery of the lens.

Results show that the wave propagation was constructed from amplitude values as small as 0.03 μm. By quantifying the wave attenuation and velocity, stiffness measurements could be potentially quantified using the models described in [210]. Also, researchers have demonstrated the quantification of elasticity properties using a single excitation pulse (non-periodic for a long

time) [211]. In this dissertation, we have shown the method to quantify wave attenuation and velocity could be applied for a single excitation pulse as well. Therefore, these results demonstrate the capability of the PhS-SSOCE system to assess the propagation of the waves in the crystalline lens with high sensitivity and hence the system could be potentially utilized to obtain the biomechanical properties of the lens.

4.6 In-situ studies

After validating PhS-SSOCE and the quantifying methodology in phantoms and *ex-vivo* studies, the method was applied to study the surface wave propagation in mice corneas as a function of age under *in-situ* conditions. *In-situ* studies are the studies performed when the biological sample is exactly in place. This subsection of the thesis describes the sample preparation, experimental procedure, results and discussion pertaining to the measurement of the surface wave propagation in mice corneas *in situ* as a function of age.

4.6.1 Sample preparation

Twelve CD1 mice consisting of six of one month in age and six of nine months in age, with a typical lifespan approximately of two years, [212] are utilized for this study. The mice were sacrificed before performing the experiment and fixed firmly below the imaging lens of the PhS-SSOCT. The mice were placed on a styrofoam base carved in the shape of the mice so that any inherent motion of the mouse head could be avoided. Before fixing the mice to the base, the eye lids and fur around the eye were shaved to avoid obstruction of the beam. The eye was hydrated periodically (every minute) to avoid dehydration and was imaged under the PhS-SSOCT.

4.6.2 Experimental procedure

The surface wave propagation on the cornea *in situ* was studied by exciting the cornea with 80 Hz sinusoidal oscillations with a maximum amplitude of 1 μm. The wave excitation is performed in the same manner as described in the phantom section.

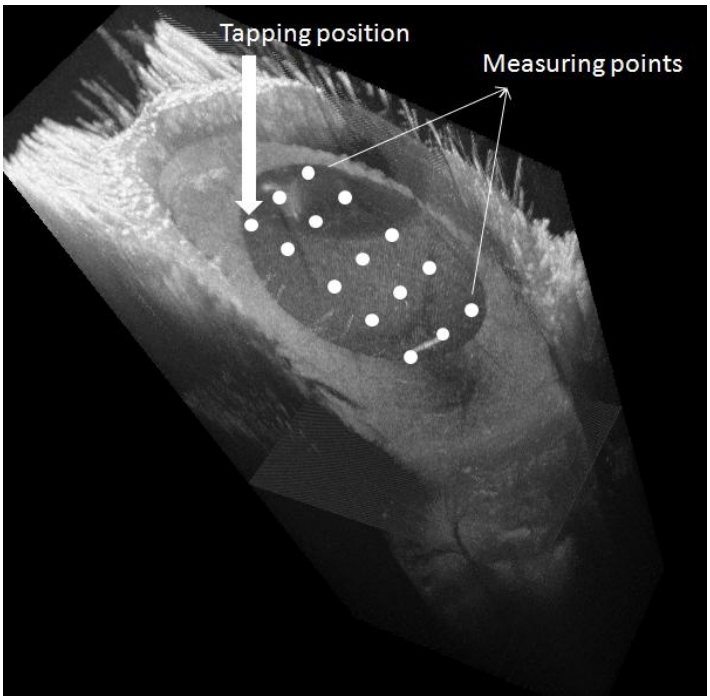

Figure 69: 3D image of the Eye indicating point of excitation and points of measurements.

Mechanical waves of 80 Hz sinusoidal frequency were introduced near the circumference of the cornea as denoted by white dots in Figure 69. Figure 69 shows the 3-D reconstruction of the mice eyes *in-situ* imaged using PhS-SSOCT before conducting the experiments. The bold pointer indicates the position where the wave is induced and all the other points indicate the measuring locations. The amplitudes are measured from the phase response of the M-mode image at the measuring points as described in the methodology section. As from the M-mode image it is

difficult to validate whether the image corresponds to the cornea or other ocular tissue nearby, at every measuring location, a 2D image is also acquired.

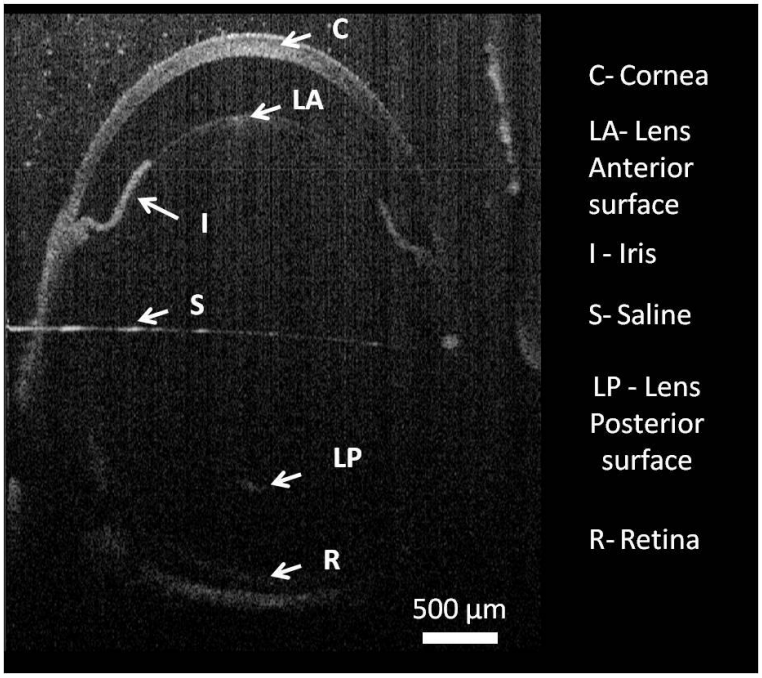

Figure 70: 2D image of the mouse eye.

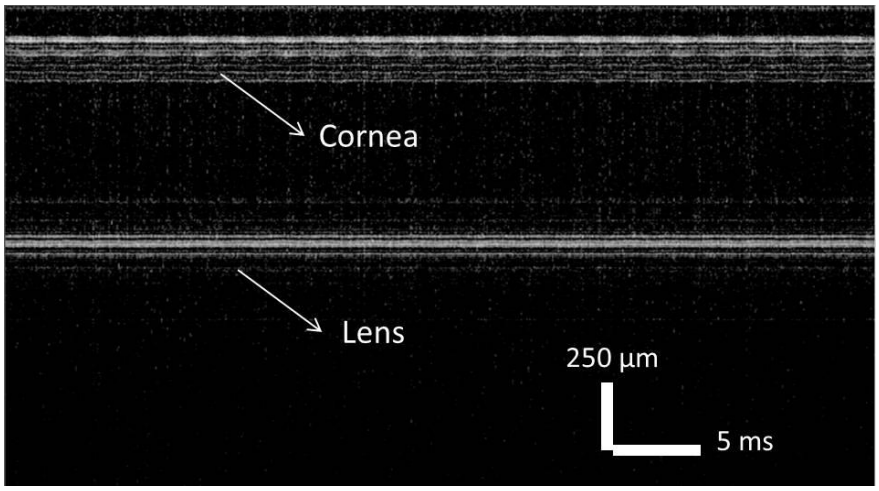

Figure 71: M-mode image at the apex of mouse eye.

If the 2D image and the M-mode image are acquired with the same data acquisition parameters, *i.e*., the B scan width of 1500 pixels, a delay of 50 ms with no phase and offsets to the galvo scanners, then the M-mode image corresponds to the center of the 2D image. The 2D image confirms the imaging location. For example, in the Figure 70, the center of the image corresponds to the corneal apex. The cornea and the lens anterior surfaces could be identified in the corresponding M-mode image as shown in Figure 71. In this way, it can be validated that the M-mode image corresponds to the cornea surface. The amplitudes were converted to absolute amplitudes as described in section 4.3.1, and a contour map of the amplitudes were plotted for the one month and the nine month old mice.

4.6.3 Results

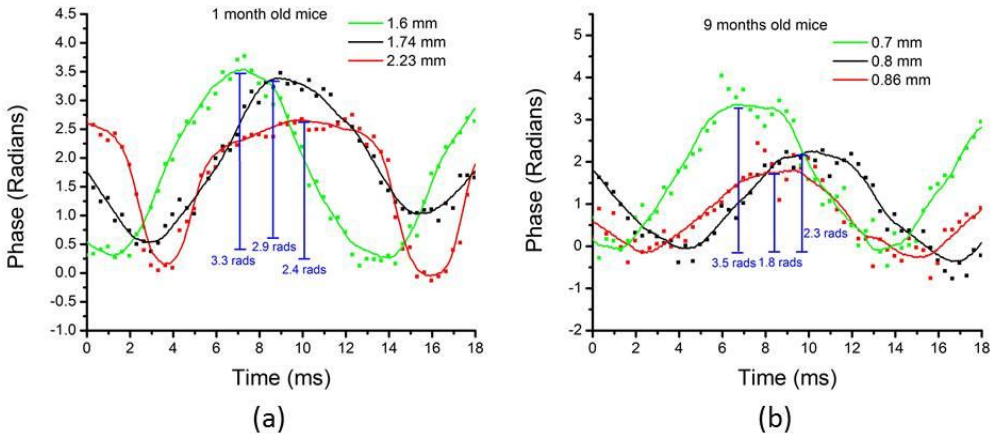

Figure 72: Phase response at the surface of the cornea to 80 Hz oscillations (a) 9 month old (b) one month old.

Figure 72 (a) and (b) show the phase responses at the cornea surface to an 80 Hz sinusoidal excitation of one month and nine months old respectively. Green, black and red are the phase values at the points away from the point of tapping. Figure 72 (a) and (b) clearly depict the decrease in the amplitudes with the increase in the distance from the point of tapping.

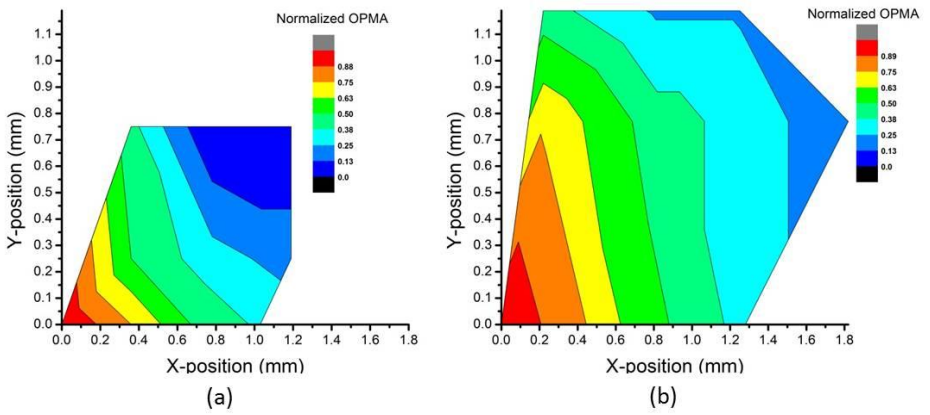

Figure 73: Amplitude distribution of propagating wave in (a) one months old mice (b) nine month old mice with point of tapping at (0, 0)

The contour plots of wave amplitudes across the cornea for the one month old and the nine months old mice are shown in Figure 73 (a) and (b) respectively. In the graphs, the X-direction is the direction where the wave amplitudes are measured parallel to the eye lid and the Y-direction is perpendicular to the eye lid. The point of tapping is taken as the origin and the amplitudes of vibrations at every point of measurement are normalized to the amplitude at the point of tapping. It can be clearly depicted from the figure that the cornea from the older eye is larger than the younger and the wave amplitudes are decreasing from the point of vibrations. It can also be seen that the wave amplitude decreases from the point of origin due to wave damping. From the data shown in Figure 73 we can assess the direction of the propagating wave and spatial damping of the wave. The amplitude distribution covered a smaller area in the one month old mouse compared to the nine month old which shows that the cornea of older mice was significantly larger than the one of the younger mice. The younger mice showed a damping of 93% per mm whereas the older mice showed a damping of 43% per mm. Moreover, the normalized amplitude drop along the X-direction is 0.714 /mm where as it is 0.35 /mm along the Y-axis in the case of the one month old mice, whereas for the older mice, it is 0.5 /mm along the X-direction and 0.28/mm along the Y-direction. This indicates that the wave attenuation is not the same across the

cornea attributing to it anisotropy. This lateral spatial anisotropy is to be expected based upon the nonuniform orientation and distribution of collagen fibrils that has been shown in mice and other animals [213]. This anisotropy is also a product of the interwoven anterior lamellar stromal architecture of the cornea at the microscopic level [214].

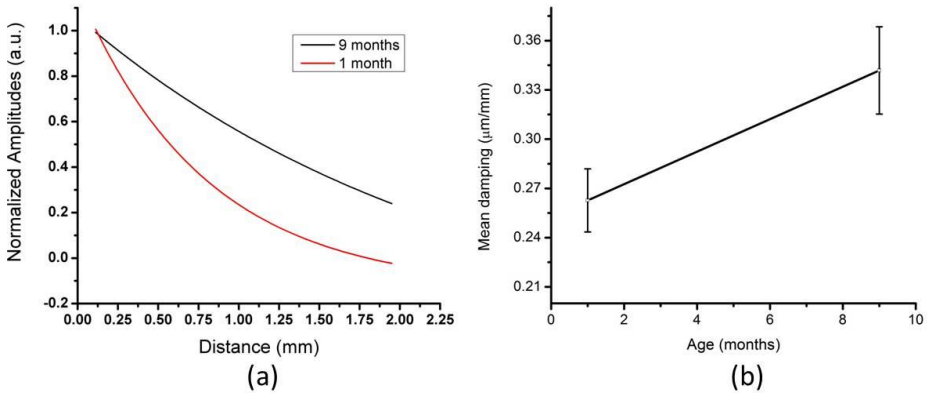

Figure 74: (a) Damping of normalized amplitude damping over the distance from the tapping point and (b) Mean attenuation vs mice age.

From these 2D distributions, the attenuation in amplitude with the increase in distance from the point of tapping in both younger and older mice is evaluated and shown in Figure 74 (a). The spatial damping of the surface wave depends on both the elasticity and the viscosity of the material; hence no quantitative conclusion about the stiffness of the cornea can be derived from these measurements. However, from Figure 74 (a) which shows the spatial damping of unit amplitude that is evaluated from the 2D maps, the ability of the cornea to absorb or transmit the vibrations can be evaluated. From the above two results, it is clear that the attenuation of the wave is not uniform across the cornea attributing to different stiffness values. Therefore, evaluation of maximum attenuation of the wave within the cornea provided the maximum possible variation in stiffness spatially. This value is calculated for all the mice corneal tissues

and we found that this value can clearly differentiate between younger and older mice. However, to obtain the stiffness distribution all over the cornea, quantification of velocity is necessary.

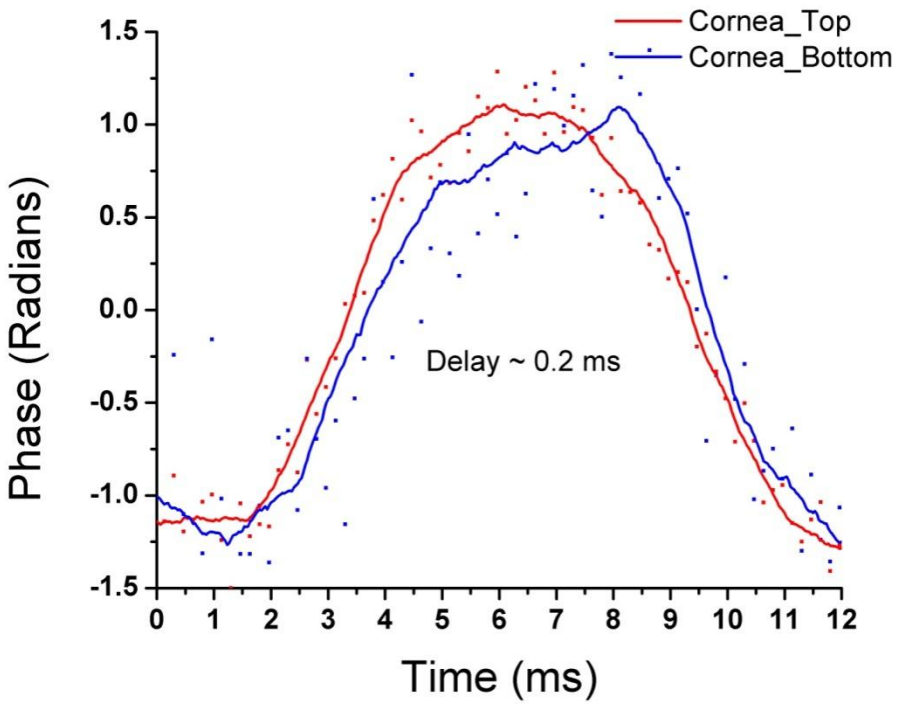

Figure 75: Phase response measured at the anterior and posterior surface of the cornea simultaneously.

Similarly, the maximum drop in amplitude per unit distance (averaged over 6 mice) is evaluated for each eye and is plotted with respect to the age of the mouse in Figure 74 (b). It clearly demonstrates that older mice have a higher maximum drop in amplitude than in younger mice. All of the above results correspond to the phase response on the top surface of the cornea.

The evaluation of phase response on the bottom layer of the cornea revealed the phase shift in the wave. The phase shift in the wave amplitude from the top surface to the bottom surface is clearly depicted in Figure 75. Preliminary analysis of the phase response on both surfaces of the cornea revealed that the phase response on the bottom surface of the cornea is shifted by 0.2 ms from the top surfaces. Therefore, the PhS-SSOCE method allows the measurement of amplitude distribution and time delay in the wave from both surfaces of the mouse cornea *in situ*.

4.7 In-vivo studies

Finally, the PhS-SSOCE is utilized to study the wave propagation in live mice *in vivo.* Wave parameters were quantified in the mouse cornea as a function of age. To the best of our knowledge, no group has so far quantified wave velocities in animal cornea under *in vivo* conditions. Therefore, PhS-SSOCE is one of the first non-invasive tools that allow *in vivo* quantification of biomechanical properties of animal cornea.

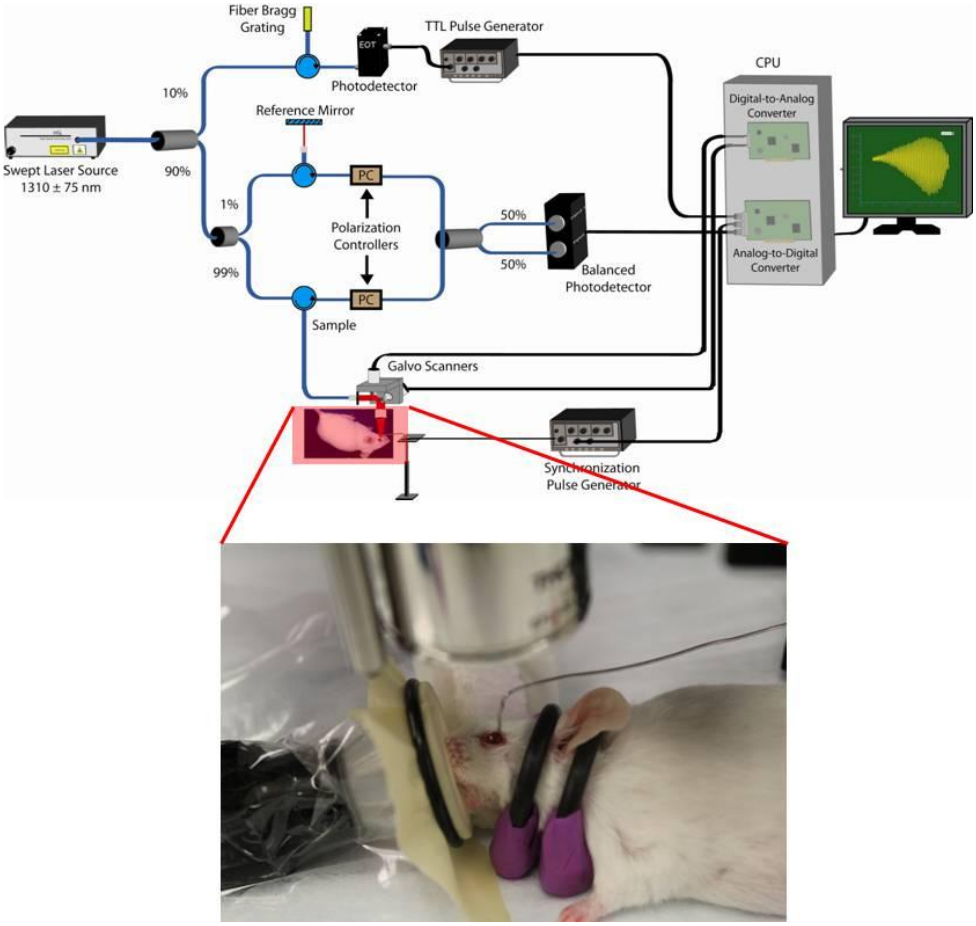

Figure 76: Experimental set up for quantification of wave parameters in live mice *in vivo.*

This section deals with the detailed description of the results and the inferences that could be drawn out from the results. This section is again organized as follows: it first describes the sample

preparation for *in vivo* studies, then the experimental procedure, results and analysis of the results.

4.7.1 Sample preparation

Three mice comprising of ages one month, six months and thirteen months were utilized for this study. The mice were anesthetized in the same manner as described in section 3.3. The mice were laid on their semi dorsal side as shown in the insert of Figure 76 so that the eyeball aligns as perpendicular as possible with the probing beam. Two rubber rings were placed around its neck which act as shock absorbers and avoid sudden artifacts in phase due to its movements. They also avoid the movement of the head due to the breathing of the mice. Before fixing the mice, the eye lids and fur around the eye were shaved to avoid obstruction of the beam. The eye was hydrated periodically (every minute) to avoid dehydration and was imaged under the PhS-SSOCT.

4.7.2 Experimental procedure

The surface wave propagation on the mice corneas *in vivo* was studied by exciting the cornea in pulsed excitation mode as described for the phantom studies. A 1 ms pulse with maximum amplitude of 1 μm was used to excite the cornea. Mechanical waves were introduced near the circumference of the cornea as denoted by white dots in Figure 77. It shows the 3-D reconstruction of the mouse eye *in-vivo* imaged using PhS-SSOCT before conducting the experiments. The bold pointer indicates the position where the wave is induced and all the other points indicate the measuring locations. The amplitudes are measured from the phase response of the M-mode image at the measuring points as described in the methodology section. The similar procedure explained under *in situ* section was adopted to make sure that the cornea was imaged. All the imaging parameters were kept the same as for the *in situ* measurements.

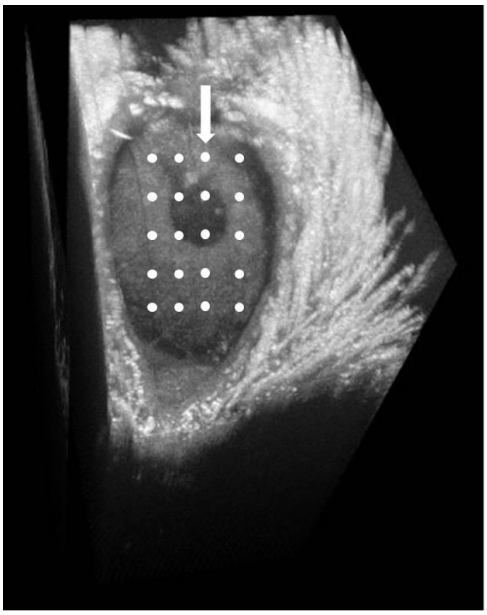

Figure 77: 3D construction of live mouse eye.

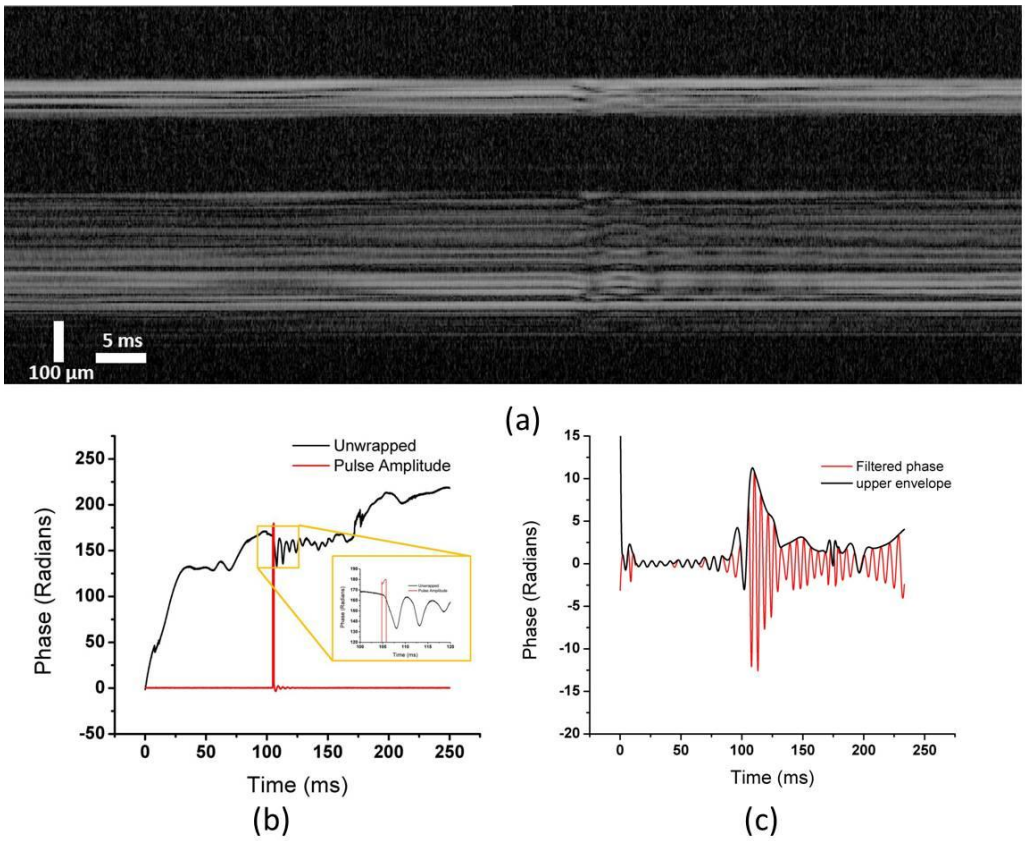

Figure 78: (a) M-mode image of the cornea (b) realtime phase response (black), excitation pulse (red) (c) Filtered phase response.

The M-mode image of the cornea when the excitation pulse is given is shown in Figure 78 (a). The image shows a wave like pattern after the induction of the wave. The corresponding phase response is shown in the Figure 78 (b). The red trace indicates the pulse when the excitation is provided and the black trace shows the real time phase response. The black trace shows an irregular pattern until the wave was induced. With the induction of the wave, the dynamic response of the cornea could be observed as shown in the insert of Figure 78 (b). The amplitudes and delays were calculated from the black trace. In case of very noisy signals, it is difficult to quantify amplitudes and delay from the real time phase. In such cases, the dynamic response could be clearly identified by filtering out the low frequency noise as shown in Figure 78 (c).

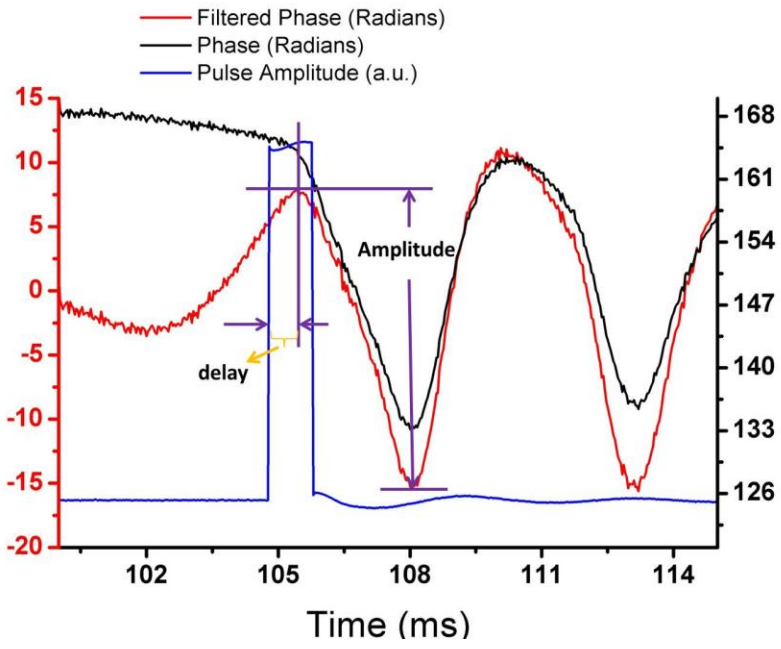

Figure 79: Signal showing quantifiable parameters.

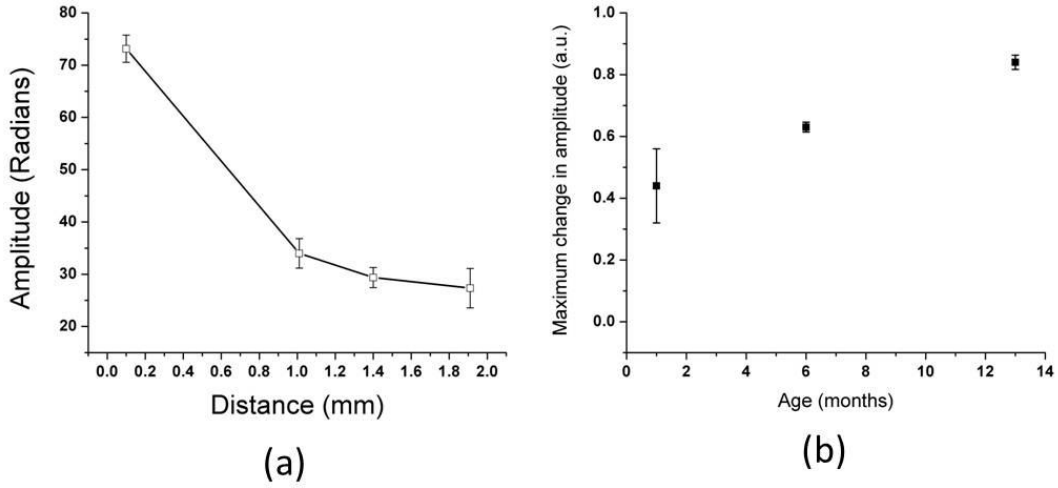

Figure 80: (a) Amplitude damping with increasing distance from tapping of six month old mice. (b) Damping per 1 mm with respect to age.

From Figure 78, the amplitudes of vibrations, delay as well as the time taken for the amplitudes to completely attenuate could be measured. The latest parameter gives the time damping of the wave. All these parameters were quantified for all the three different aged mice. The quantification of each parameter was clearly shown in Figure 79.

Amplitudes of vibrations were plotted with the increasing distance from the point of tapping. As expected, the amplitudes dropped in an exponential pattern as shown in Figure 80 (a). The maximum attenuation of amplitude per mm was plotted in Figure 80 (b). Figure 80 (b) shows that the damping per unit distance is higher for older mice. However, if we consider that the older mice corneas are more elastic than the younger ones, then damping per unit distance must be higher for younger mice as shown for *in situ* measurements. This inconsistency could be explained by analyzing the *in situ* results with more details. From the *in situ* results, it was known that the amplitude damping of the wave is not uniform over the eyeball which was attributed to the anisotropy of the eye. Moreover, from the graph showing the maximum stiffness change within the eye, it was inferred that the younger mice corneas have lower stiffness change within

the eye, whereas the older mice corneas have higher stiffness change. With this background and the fact that the amplitude propagation depends on both elasticity and viscocity of the medium, the graph shown in the Figure 80 (b) depicts the maximum stiffness change within the eye.

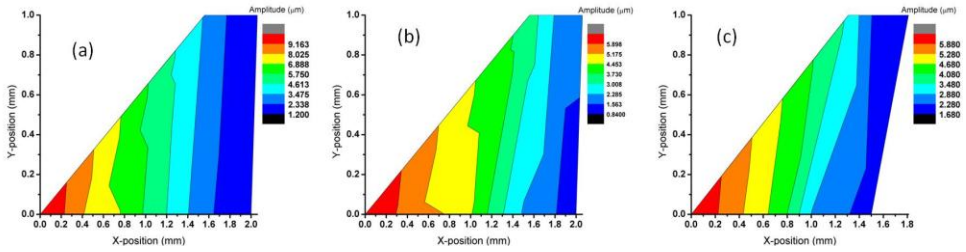

Figure 81 (a) 2D wave propagation on mice cornea (b) corresponding wave propagation on the anterior surface of the lens (c) corresponding wave propagation on posterior surface of the lens.

2D contour maps of the wave propagation on the cornea, anterior and posterior surfaces of the lens were plotted in Figure 81 (a), (b) and (c) respectively. The 2D contour plots generated in this case do not have sufficient sampling as the bottom layer of the lens is not captured at many locations. However, the result still depicts the decrease in amplitude away from the point of tapping.

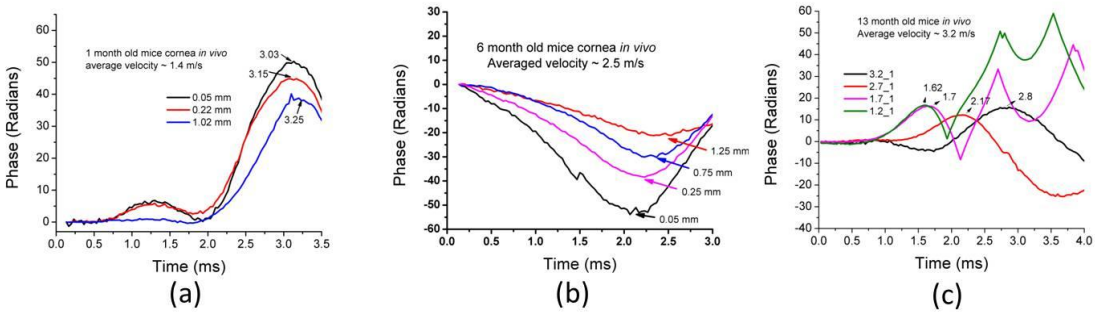

Figure 82: Phase response of one month old mice showing the delay and drop in amplitude.

Wave velocities were measured following the same procedure as described in the phantoms section. The phase response at an increasing distance from the point of tapping to all mice is

shown in Figure 82. As expected, the amplitude dropped with the increase in distance from the point of tapping and a delay was observed. The wave velocities were quantified from these delays.

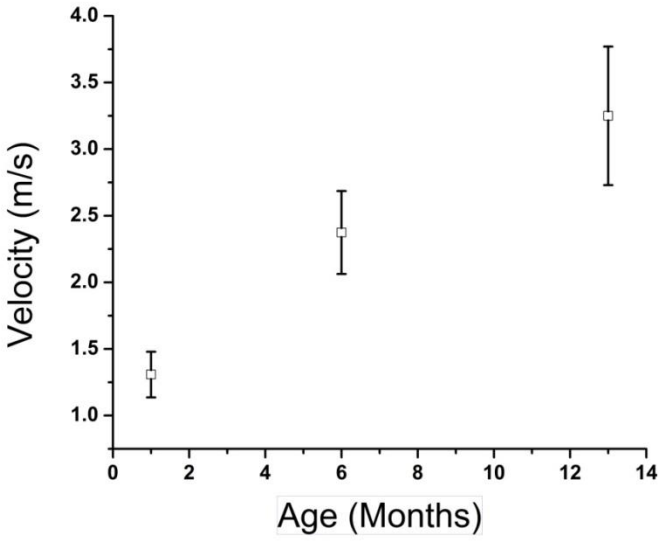

Figure 83: Surface wave velocity Vs age in mice cornea.

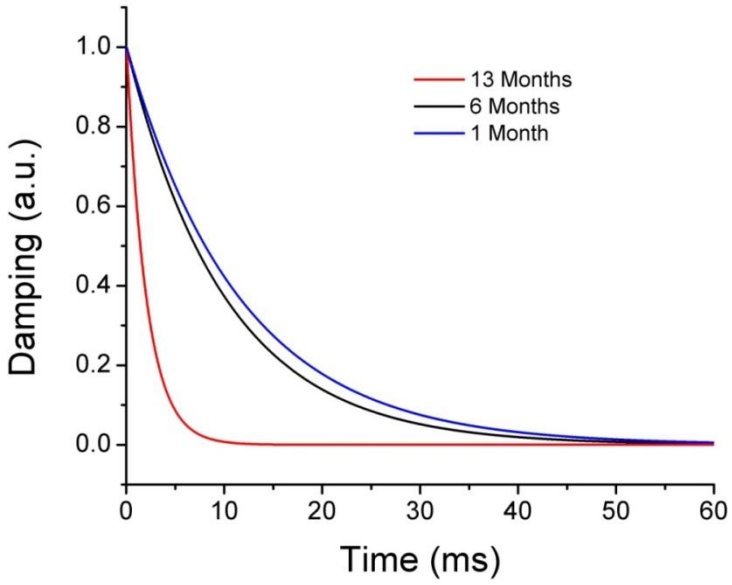

Figure 84: Time damping of mice corneas to pulsed excitation.

The wave velocities for all the three ages are plotted in Figure 83. The figure depicts that the velocities increased with the increase in age. Comparing these results with the phantoms, it can be clearly stated that older mice corneas are stiffer than the younger mice.

Time damping or the amount of time for which the cornea vibrated is calculated for each mouse. This value is measured by obtaining the exponential fit to the filtered phase response. These exponential fits corresponding to the region where the wave velocity was maximum is plotted and shown in Figure 84. It can be clearly depicted from the figure that, older mice cornea damps faster than the younger mice. Moreover, there is not much of a difference in time constants between one month and six month old, however, the difference is higher in 13 months compared to the younger mice. The results suggest that, time damping can also be a quantifying parameter that can distinguish stiffness.

From all of the above results, it can be stated that PhS-SSOCE is the first tool to measure wave parameters in the cornea and lens *in vivo.* By developing a proper model, biomechanical properties could be quantified. However, the scope of this dissertation is to develop instrumentation and a method to quantify wave parameters in live animals which was achieved.

V. CHAPTER 5. CONCLUSION

5.1 Summary

This dissertation described the design and development of a novel imaging device that was capable of high speed, 2D and 3D non-invasive imaging of tissue samples under *in vivo* conditions. Applications of the developed system for *in vivo* detection of microbubbles in mice tail vein and *in vivo* quantification of wave parameters in mice eyes were presented. Results suggest that PhS-SSOCT is an effective biosensor that can be easily translated for early clinical diagnosis.

The results of characterization of the system (Chapter II) demonstrated the high speed real time imaging capabilities of the developed system. Real time speed of 40 fps with a frame size of 1600X 500, an axial resolution of 8 μm, a SNR > 100 dB allows for an easy translation of the system for clinical applications. A phase stability of 0.016 radians which translates to a displacement sensitivity of ~ 2 nm shows that the major advantage of the developed system is the high sensitivity of detection.

The results of studies performed for the detection of microbubbles in clear and scattering media (Chapter III) demonstrated that the developed phase resolved method for quantifying air bubbles is capable of detecting bubbles smaller than 8 μm. The *in vivo* results show that the system is capable of detecting and monitoring microbubbles of sizes as small as 60 μm inside a mouse tail vein. Results also suggest the possibility of 3D monitoring of microbubbles in live animals. 3-D monitoring of microbubbles in tissues and blood by PhS-SSOCT offers a glimpse into the future of second generation OCT systems that might reside in the diagnostics wing of space stations and underwater machines. With its demonstrated performance and potential, PhS-

SSOCT is a promising technology for early diagnostics of diseases related to decompression sickness.

The results for the elastography applications (Chapter IV) demonstrate that the system in combination with the imaging and quantifying method is capable of very high sensitive displacement measurements (~ 30 nm) in phantoms. They also suggest that the wave velocities within 150 m/s can be measured. The *in vitro* and *ex vivo* results allowed a detailed analysis of wave propagation in mice corneas and lens as a function of age. Results showed that the velocities increased with the increase in age and also wave attenuation is not uniform within the eye attributing to anisotropy of the eye. The similar analysis was extended to the *in vivo* quantification of wave parameters suggesting that the system along with the quantifying method is capable of obtaining parameters of the waves propagating in the ocular tissues. These results could be utilized for various studies. For example, the results could be used to obtain biomechanical properties such as Young's modulus of ocular tissues under live conditions which has not been achieved so far.

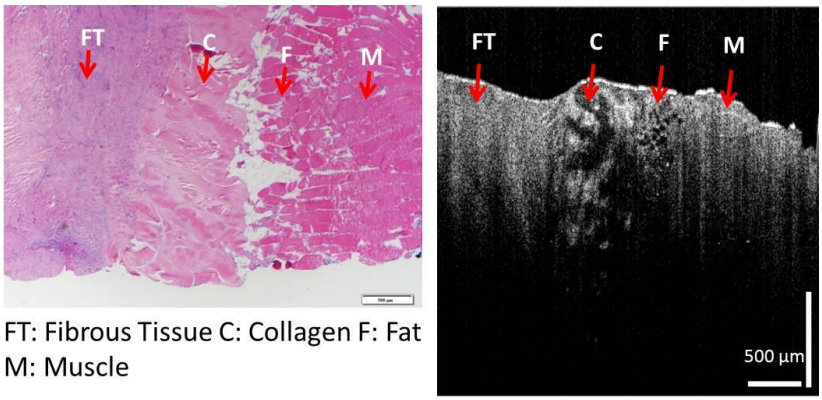

Figure 85: 2D image of human fat tissue showing the boundary between cancer and normal tissue.

Apart from the major applications described in this dissertation, the system was also used in various other biomedical applications such as imaging cancerous and normal tissues, whole zebra fish and mutant mice. For example, Figure 85 shows the 2D image of human tissue dissected for biopsy for cancer diagnosis. The figure depicts both cancerous and normal fat tissue showing capability of PhS-SSOCT to distinguish leiomyosarcoma and fat tissue. The boundary between the cancerous and normal tissue can be clearly identified. Therefore, PhS-SSOCT could also be applied for cancer diagnosis.

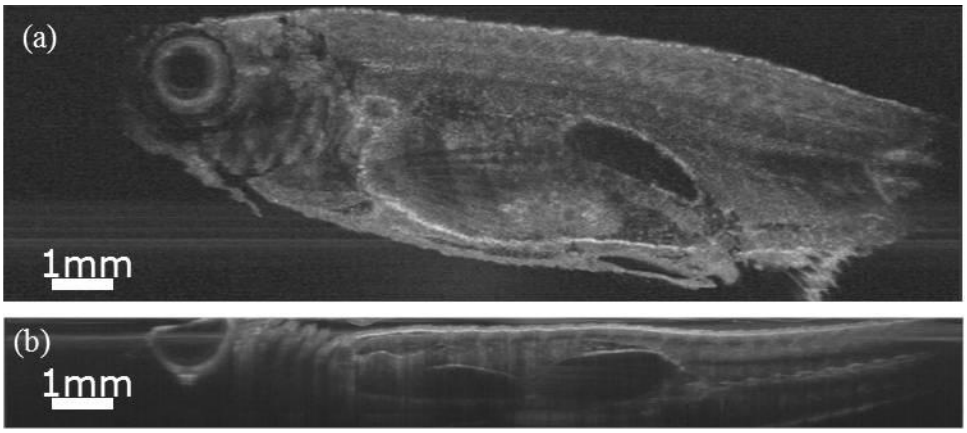

Figure 86: (a) Enface image of a Zebra fish (b) Longitudinal 2D depth wise image.

Similarly, a whole Zebrafish was imaged as shown in the Figure 86. Figure 86 (a) depicts the wide field of view (10 mm X 10 mm) and Figure 86 (b) shows the capability of PhS-SSOCT for imaging whole depth.

Applications of PhS-SSOCT in developmental biology were demonstrated by comparing mutant and normal mice embryos of the same stage. 3D images of mice embryo limbs were taken and observed for their differences with mutant samples. In Figure 87 (a), the mutant's fingers on its left forelimb look conjoined or webbed, while the normal embryo's fingers in Figure 87 (b) are more distinct. These embryos are at the same stage of development, and yet the normal mouse's fingers seem more mature.

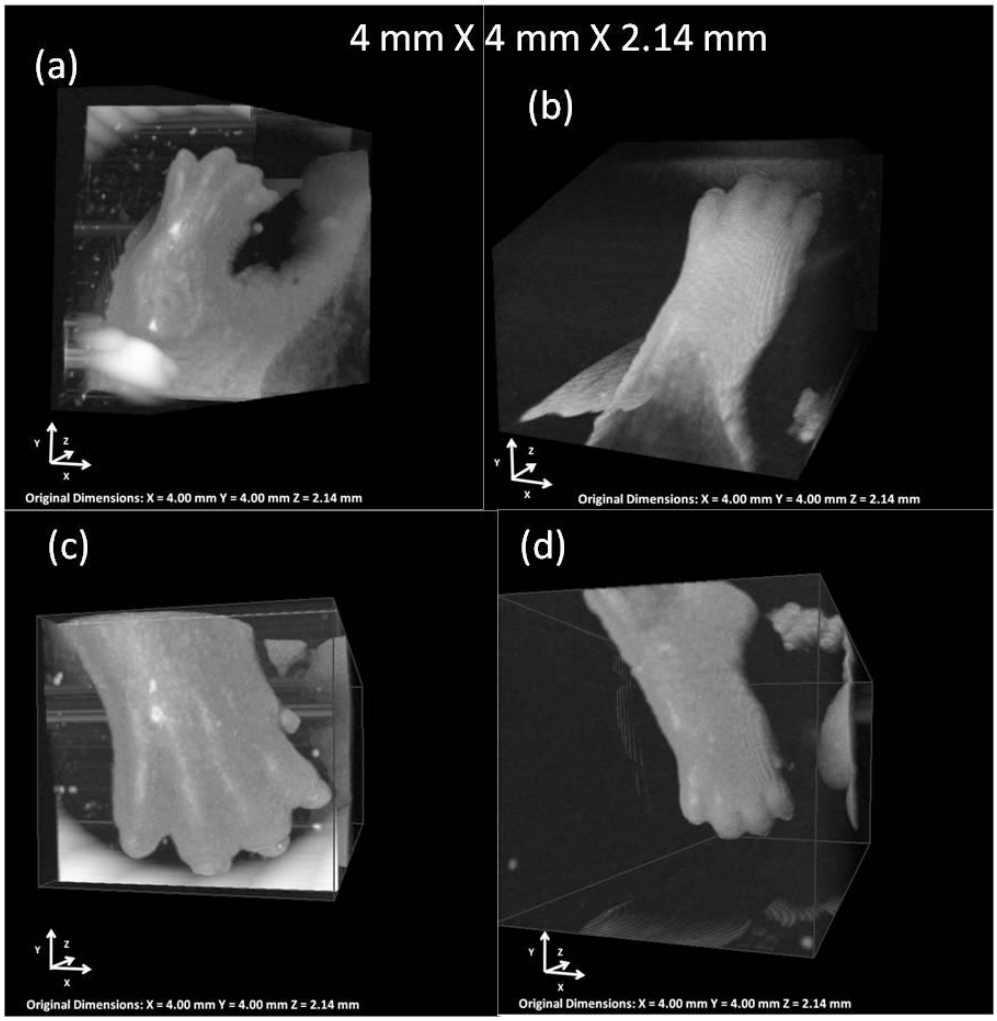

Figure 87: 3D image of limb of mice embryo (a) Mutant fore limb (b) Normal forelimb (c) mutant hind limb (d) normal hind limb.

Like its left one, the mutant's right forelimb also has webbed fingers as shown in Figure 87 (c). The normal mouse's fingers are more defined and even bent a little which demonstrates increasing dexterity (Figure 87 (d)). These images suggest that the bone growth in the mutant's forelimbs is stunted relative to that of the normal embryo.

All of the above results suggest the capability of OCT for studying pathologies of various kinds. In particular, PhS-SSOCT is an effective tool that has the potential to be an early

diagnostic tool as well as a tool to study biomedical processes non-invasively and under live conditions.

5.2 Discussions and future work

The uniqueness of these phase-resolved measurements presents challenges as well as opportunities for the future. Stabilizing the phase from the reference arm can drive the system for its use in inter-interference mode that would allow the detection of bubbles in tissues and blood. Stabilizing the phase from the reference arm would be a challenging task when MZI is used for the recalibration process. Although there have been many studies published on phase stabilization of up to 3 mrad, they either use offline calibration or software techniques like Kasai autocorrelation[215]. With offline calibration, the calibration is done only once, which does not allow calibrating every time the laser starts. So, any drift in the laser output spectrum with time would result in a faulty calibration, thus leading to resolution degradation. For clinically viable systems, it is not desirable to have to calibrate regularly. Thus, achieving a phase stability of 0.03 radians in inter-interference mode with real time calibration using MZI that would not yield images with resolution degradation with time, would allow the system to be clinically viable.

Addressing to the above challenges, a slightly modified design and calibration algorithms were developed that offered better phase stability. This new design was developed as a proof of concept only and was not utilized in this dissertation. With the implementation of this concept, the phase stability could be further enhanced to improve the sensitivity of measurements. The new design is shown in Figure 88. 90% of the light from the laser is given to the imaging interferometer that contains two arms; the reference and the sample arm. Fringes are formed from the interference of the light returned from each of the arms which is then detected by a balanced photodiode. The computer acquires the data by digitizing the photodiode output using a 16-bit (ADC).

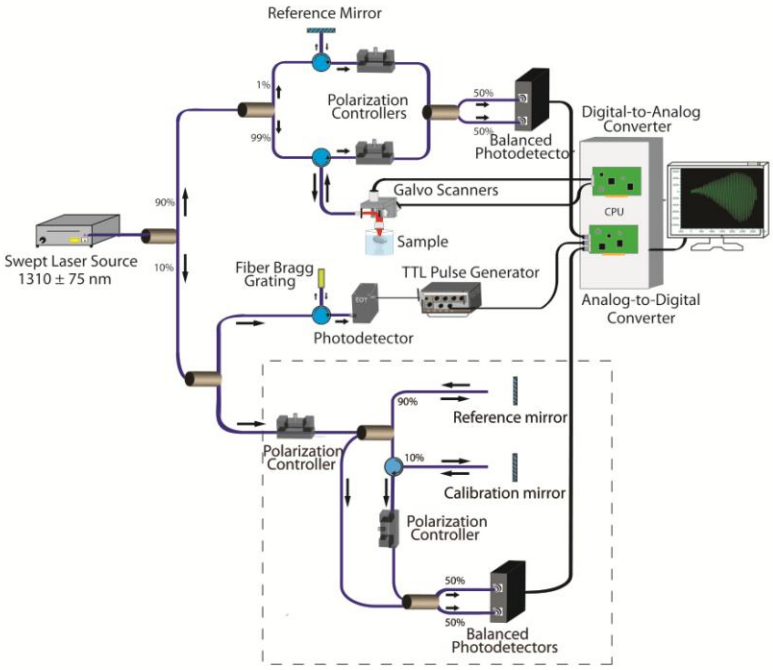

Figure 88: The Schematic of PhS-SSOCT.

The calibration interferometer is another Mach-Zehnder based interferometer in which one of the arms is placed on a 1-D stage to attain variable path differences. The fringes from the calibration interferometer are utilized to correct the non-linearity in wavelength scanning of the swept laser and remapping the time delay domain to frequency *k*-space. The procedure is adapted as follows: The real fringes are converted to the complex domain using Hilbert transformation. The unwrapped phase differences extracted from these complex fringes gave us the behavior of the propagation vector *k* for one laser sweep provided the path length is kept constant (Equation 19). Hence, the non-linearity in the wavelength scanning is obtained directly in *k*-space and was corrected by linearizing the unwrapped phases using Equation 12.

The phase calibration is performed similar to the phase resolved OCT technique described in Ref [216]. In this method, the phase variations at the end of every sweep and the beginning of the next sweep are obtained from the *k*-space calibration interferometer itself, thus

maintaining dynamic calibration. These phase variations are then utilized to correct the original phase using the Equation 18,

$$\Delta\widetilde{\emptyset}_{i,j} = \Delta\emptyset_{i,j} - \left\{\frac{i}{m}\right\} * \Delta\emptyset_{m,j}.$$

Equation 18

In the Equation 18, $\Delta\widetilde{\emptyset}_{i,j}$ is the corrected phase difference at the depth index *i*, $\Delta\emptyset_{i,j}$ is the original phase difference and $\Delta\emptyset_{m,j}$ is the phase difference of the calibrating signal at the depth index *m.* Our study showed that the measurement of these phase variations depend on the *k*-space calibration and it is a well-known fact that the resolutions also depend on the calibration. Thus, the resolutions and the phase stabilities are evaluated for different calibrating signals generated at various path lengths of the calibrating interferometer and finally correction coefficients are generated from the sectional depths called sectional linear *k* (*slk*) coefficients for the optimal performance of the PhS-SSOCT.

The preliminary results depicted in Figure 89 (a) and (b) show the improvement of the resolution and the phase stability after utilizing the sectional *k*-space calibration and phase correction respectively. The x-axis in the Figure 89 (a) is the path differences between the two arms in the calibration interferometer. The y-axis is the phase stability obtained from the self-interference peak from a glass slide of thickness 0.12 mm. From the Figure 89(a), the phase stability is improved by 0.03 radians for most of the calibration frequencies. Only these frequencies are utilized for generating the *slk* mapping, thus maintaining the phase stabilities. In Figure 89 (b), resolutions are plotted at each depth after calibrating the raw signal with the conventional *k*-space calibration and with the *slk* calibration. The result clearly depicts the improvement of the resolution.

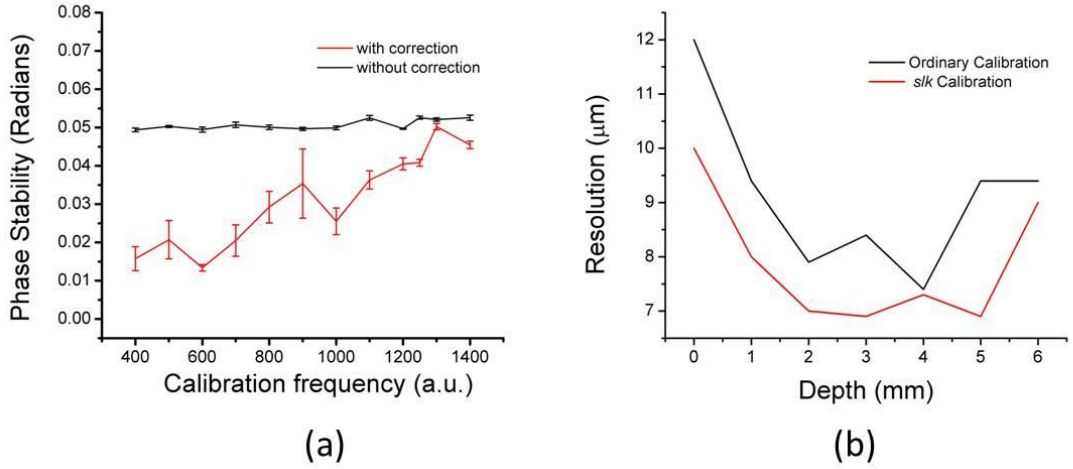

Figure 89: (a) Phase stability with and without correction vs Calibration frequency (b) Resolution vs Depth.

5.3 Conclusion

Our studies demonstrated:

1. the design and instrumentation of a phase stabilized swept source OCT with an axial resolution of 8 μm, real time imaging speed of 40 fps and a phase stability of 0.016 radians that translates to ~2 nm displacements,

2. an effective quantification method that allowed quantification of very small microbubbles,

3. the wave velocities in the mice corneas increased with the increase in age,

4. the wave attenuation is different across the eye as well as with the change in age.

The obtained results suggest that the PhS-SSOCT in combination with the quantification method has the potential to monitor microbubbles in arteries and veins. In addition, it enables the quantification of wave parameters in the ocular tissue with very small excitation amplitude.

Successful development of the system allows clinical diagnosis of diseases related to DCS and also ophthalmic pathologies.

REFERENCES

[1] J. Miao, P. Charalambous, J. Kirz, and D. Sayre, "Extending the methodology of X-ray crystallography to allow imaging of micrometre-sized non-crystalline specimens," Nature, 400(6742), 342-344 (1999).

[2] F. Pfeiffer, T. Weitkamp, O. Bunk, and C. David, "Phase retrieval and differential phase-contrast imaging with low-brilliance X-ray sources," Nature Physics, 2(4), 258-261 (2006).

[3] B. F. Wall, G. M. Kendall, A. A. Edwards, S. Bouffler, C. R. Muirhead, and J. R. Meara, "What are the risks from medical X-rays and other low dose radiation?," British Journal of Radiology, 79(940), 285-294 (2006).

[4] F. A. Mettler, and M. J. Guiberteau, [Essentials of nuclear medicine imaging. 3rd edition], (1991).

[5] M. W. Groch, and W. D. Erwin, "SPECT in the Year 2000: Basic Principles," Journal of Nuclear Medicine Technology, 28(4), 233-244 (2000).

[6] P. C. Lauterbur, "Image Formation by Induced Local Interactions: Examples Employing Nuclear Magnetic Resonance," Nature, 242(5394), 190-191 (1973).

[7] R. Turner, D. L. Bihan, C. T. W. Moonen, D. Despres, and J. Frank, "Echo-planar time course MRI of cat brain oxygenation changes," Magnetic Resonance in Medicine, 22(1), 159-166 (1991).

[8] A. Cusumano, D. J. Coleman, R. H. Silverman, D. Z. Reinstein, M. J. Rondeau, R. Ursea, S. M. Daly, and H. O. Lloyd, "Three-dimensional ultrasound imaging: Clinical applications," Ophthalmology, 105(2), 300-306 (1998).

[9] H.-I. W. Lihong V. Wang, [Biomedical optics: Principles and Imaging] Wiley-Interscience, (2007).

[10] D. Huang, E. A. Swanson, C. P. Lin, J. S. Schuman, W. G. Stinson, W. Chang, M. R. Hee, T. Flotte, K. Gregory, C. A. Puliafito, and J. G. Fujimoto, “Optical coherence tomography,” Science, 254(5035), 1178-81 (1991).

[11] A. F. Fercher, W. Drexler, C. K. Hitzenberger, and T. Lasser, “Optical coherence tomography - principles and applications,” Reports on Progress in Physics, (2003).

[12] J. M. Schmitt, “Optical coherence tomography (OCT): A review. ,” IEEE Journal of Selected Topics in Quantum Electronics, 1205 (1999).

[13] P. H. Tomlins, and R. K. Wang, “Theory, developments and applications of optical coherence tomography,” Journal of Physics D: Applied Physics, 2519-2535 (2005).

[14] D. Huang, J. wang, C. P. Lin, C. A. Puliafito, and J. G. Fujimoto, “Micro-resolution ranging of cornea and anterior chamber by optical reflectometry.,” Lasers Surgery in medicine, 11, 419-425 (1991).

[15] M. R. Hee, C. A. Puliafito, C. Wong, J. S. Duker, E. Reichel, B. Rutledge, J. S. Schuman, E. A. Swanson, and J. G. Fujimoto, “Quantitative assessment of macular edema with optical coherence tomography,” Archives of Ophthalmology, 113(8), 1019-29 (1995).

[16] S. A. Chalabi, B. Culshaw, and D. E. N. Davies, "Partially coherent sources in interferometric sensors.." IEE, 132-135.

[17] R. C. Youngquist, S. Carr, and D. E. N. Davies, “Optical Coherence-domain reflectometry: A new optical evaluation technique,” Optics Letters, 12(3), 158-160 (1987).

[18] A. F. Fercher, K. Mengedoht, and W. Werner, “Eye length measurement by interferometry with partially coherent light,” Optics Letters, 13(3), 186-189 (1988).

[19] C. K. Hitzenberger, “Optical measurement of the axial eye length by laser doppler interferometry,” Investigative Opthalmology and visual science, 32, 616-624 (1991).

[20] J. F. de Boer, B. Cense, B. H. Park, M. C. Pierce, G. J. Tearney, and B. E. Bouma, "Improved signal-to-noise ratio in spectral-domain compared with time-domain optical coherence tomography," Optics Express, 28, 2067-2069 (2003).

[21] R. Leitgeb, C. K. Hitzenberger, and A. F. Fercher, "Performance of Fourier domain vs time domain optical coherence tomography," Optics Express, 11, 889-894 (2003).

[22] B. Veksler, E. Kobzev, M. Bonesi, and I. Meglinski, "Application of optical coherence tomography for imaging of scaffold structure and micro-flows characterization," Laser Physics Letters, 5(3), 236-239 (2007).

[23] B. J. Vakoc, S. H. Yun, J. F. de Boer, G. J. Tearney, and B. E. Bouma, "Phase-resolved optical frequency domain imaging," Optics Express, 13, 5483-5493 (2005).

[24] E. C. W. Lee, [Optical frequency domain imaging of human retina and choroid] Massachusetts Institute of Technology, Cambridge(2006).

[25] M. A. Choma, M. V. Sarunic, C. H. Yang, and J. A. Izatt, "Sensitivity advantage of swept source and Fourier domain optical coherence tomography," Optics Express, 11(18), 2183 (2003).

[26] J. F. de Boer, B. Cense, B. H. Park, M. C. Pierce, G. J. Tearney, and B. E. Bouma, "Improved signal-to-noise ratio in spectral-domain compared with time-domain optical coherence tomography," Optics Letters, 28(21), 2067 (2003).

[27] R. Leitgeb, C. K. Hitzenberger, and A. F. Fercher, "Performance of fourier domain vs. time domain optical coherence tomography," Optics Express, 11(8), 889 (2003).

[28] M. A. Choma, K. Hsu, and I. A. Izatt, "Swept source optical coherence tomography using al fiber 1300 nm ring laser source," Journal of Biomedical Optics, 10(4), (2005).

[29] H. Barfuss, and E. Brinkmeyer, "Modified optical frequency domain reflectometry with high spatial resolution for components of integrated optics systems," Journal of Light wave technology, 7, 3-10 (1989).

[30] E. Brinkmeyer, and R. Ulrich, “High resolution OCDR in dispersive waveguides,” Electronic letters, 26, 413-414 (1990).

[31] S. H. Yun, C. Boudoux, G. J. Tearney, and B. E. Bouma, “High-speed wavelength-swept semiconductor laser with a polygon-scanner-based wavelength filter.,” Optics Letters, 28, 1981-1983 (2003).

[32] S. H. Yun, G. J. Tearney, J. F. De Boer, and B. E. Bouma, “Motion artifacts in optical coherence tomography with frequency-domain ranging,” Optics Express, 12, 2977-2998 (2004).

[33] S. H. Yun, G. J. Tearney, J. F. De Boer, N. Iftimia, and B. E. Bouma, “High speed optical-frequency domain imaging,” Optics Express, 11(22), 2953-2963 (2003).

[34] A. Szkulmowska, M. Szkulmowski, A. Kowalczyk, and M. Wojtkowski, “Phase-resolved Doppler optical coherence tomography?limitations and improvements,” Optics Letters, 33(13), 1425-1427 (2008).

[35] B. Baumann, B. Potsaid, M. F. Kraus, J. J. Liu, D. Huang, J. Hornegger, A. E. Cable, J. S. Duker, and J. G. Fujimoto, “Total retinal blood flow measurement with ultrahigh speed swept source/Fourier domain OCT,” Biomedical Optics Express, 2(6), 1539-1552 (2011).

[36] M. A. Choma, A. K. Ellerbee, C. Yang, T. L. Creazzo, and J. A. Izatt, “Spectral-domain phase microscopy,” Optics Letters, 30(10), 1162-1164 (2005).

[37] E. C. Lee, J. F. de Boer, M. Mujat, H. Lim, and S. H. Yun, “In vivo optical frequency domain imaging of human retina and choroid,” Optics Express, 14(10), 4403-4411 (2006).

[38] B. E. Bouma, and G. J. Tearney, [Handbook of optical coherence tomography] Marcel Dekker, Inc.,, New York(2002).

[39] D. Marks, P. S. Carney, and S. A. Boppart, “Adaptive spectral apodization for sidelobe reduction in optical coherence tomography images,” Journal of Biomedical Optics, 9(6), 1281-1287 (2004).

[40] R. Manapuram, V. Manne, and K. Larin, "Development of phase-stabilized swept-source OCT for the ultrasensitive quantification of microbubbles," Laser Physics, 18(9), 1080-1086 (2008).

[41] R. K. Manapuram, V. G. R. Manne, and K. V. Larin, "Phase-sensitive swept source optical coherence tomography for imaging and quantifying of microbubbles in clear and scattering media," Journal of Applied Physics, 105(10), 102040 (2009).

[42] S. A. Pulley, [Decompression Sickness] eMedicine, (2005).

[43] D. G. Grosset, D. Georgiadis, A. W. Kelman, P. Cowburn, S. Stirling, K. R. Lees, A. Faichney, A. Mallinson, R. Quin, I. Bone, L. Pettigrew, E. Brodie, T. MacKay, and D. J. Wheatley, "Detection of microemboli by transcranial Doppler ultrasound," Tex Heart Inst J, 23(4), 289-92 (1996).

[44] T. G. Mackay, D. Georgiadis, D. G. Grosset, K. R. Lees, and D. J. Wheatley, "On the origin of cerebrovascular microemboli associated with prosthetic heart valves," Neurol Res, 17(5), 349-52 (1995).

[45] D. Georgiadis, D. G. Grosset, A. Kelman, A. Faichney, and K. R. Lees, "Prevalence and characteristics of intracranial microemboli signals in patients with different types of prosthetic cardiac valves," Stroke, 25(3), 587-92 (1994).

[46] V. Zderic, A. Keshavarzi, M. A. Andrew, S. Vaezy, and R. W. Martin, "Attenuation of porcine tissues in vivo after high-intensity ultrasound treatment," Ultrasound in Medicine and Biology, 30(1), 61-66 (2004).

[47] H. L. Liu, Y. Y. Chen, W. S. Chen, T. C. Shih, J. S. Chen, and W. L. Lin, "Interactions between consecutive sonications for characterizing the thermal mechanism in focused ultrasound therapy," Ultrasound in Medicine and Biology, 32(9), 1411-1421 (2006).

[48] W. S. Chen, C. Lafon, T. J. Matula, S. Vaezy, and L. A. Crum, "Mechanisms of lesion formation in high intensity focused ultrasound therapy," Acoustics Research Letters Online-Arlo, 4(2), 41-46 (2003).

[49] D. E. Davies, K. I. Digwood, and J. N. Hilton, "Air-Embolism During Cesarean-Section," Medical Journal of Australia, 1(13), 644-646 (1980).

[50] T. W. K. Lew, D. H. B. Tay, and E. Thomas, "Venous Air-Embolism During Cesarean-Section - More Common Than Previously Thought," Anesthesia and Analgesia, 77(3), 448-452 (1993).

[51] D. Younker, V. Rodriguez, and J. Kavanagh, "Massive Air-Embolism During Cesarean-Section," Anesthesiology, 65(1), 77-79 (1986).

[52] A. Weissman, S. Kol, and B. A. Peretz, "Gas embolism in obstetrics and gynecology - A review," Journal of Reproductive Medicine, 41(2), 103-111 (1996).

[53] D. R. Stoloff, R. A. Isenberg, and A. I. Brill, "Venous air and gas emboli in operative hysteroscopy," Journal of the American Association of Gynecologic Laparoscopists, 8(2), 181-192 (2001).

[54] D. A. Robinson, and M. S. Albin, "Venous Air-Embolism and Cesarean Sections," Anesthesiology, 66(1), 93-94 (1987).

[55] M. Nims, H. Hallonquist, and W. Camann, "Coronary arterial air embolus occurring during cesarean delivery," Int J Obstet Anesth, 15(2), 166-9 (2006).

[56] A. Nims, H. Hallonquist, and W. Camann, "Coronary arterial air embolus occurring during cesarean delivery," International Journal of Obstetric Anesthesia, 15(2), 166-169 (2006).

[57] Y. Mushkat, D. Luxman, Z. Nachum, M. P. David, and Y. Melamed, "Gas Embolism Complicating Obstetric or Gynecologic Procedures - Case-Reports and Review of the Literature," European Journal of Obstetrics Gynecology and Reproductive Biology, 63(1), 97-103 (1995).

[58] N. C. Matthews, and G. Greer, "Embolism During Cesarean-Section," Anaesthesia, 45(11), 964-965 (1990).

[59] M. A. Kostash, and F. Mensink, “Lethal air embolism during cesarean delivery for placenta previa,” Anesthesiology, 96(3), 753-754 (2002).

[60] J. S. Handler, and P. R. Bromage, “Venous Air-Embolism During Cesarean Delivery,” Regional Anesthesia, 15(4), 170-173 (1990).

[61] M. Kurusz, and B. D. Butler, “Bubbles and bypass: an update,” Perfusion-Uk, 19, S49-S55 (2004).

[62] K. Yoshitani, F. de Lange, Q. Ma, H. P. Grocott, and G. B. Mackensen, “Reduction in air bubble size using perfluorocarbons during cardiopulmonary bypass in the rat,” Anesthesia and Analgesia, 103(5), 1089-1093 (2006).

[63] S. Martens, M. Dietrich, M. Doss, H. Deschka, H. Keller, and A. Moritz, “Behavior of gaseous microemboli in extracorporeal circuits: Air versus CO2,” International Journal of Artificial Organs, 29(6), 578-582 (2006).

[64] S. Goritz, H. Schelkle, J. G. Rein, and S. Urbanek, “Dynamic bubble trap can replace an arterial filter during cardiopulmonary bypass surgery,” Perfusion-Uk, 21(6), 367-371 (2006).

[65] W. D. Liska, and B. A. Poteet, “Pulmonary embolism associated with canine total hip replacement,” Veterinary Surgery, 32(2), 178-186 (2003).

[66] J. Dalsgaard, N. P. Sand, S. Felsby, P. Juelsgaard, and K. Thygesen, “R-wave changes in fatal air embolism during bone cementation,” Scand Cardiovasc J, 35(1), 61-4 (2001).

[67] R. A. Weiss, and G. Munavalli, “Endovenous ablation of truncal veins,” Seminars in Cutaneous Medicine and Surgery, 24(4), 193-199 (2005).

[68] R. S. Reust, B. C. Diener, J. S. Stroup, and G. D. Haraway, “Hyperbaric treatment of arterial CO2 embolism occuring after laparoscopic surgery: A case report,” Undersea & Hyperbaric Medicine, 33(5), 317-320 (2006).

[69] T. Lifshitz, J. Levy, I. Klemperer, and S. Levinger, "Anterior chamber gas bubbles after corneal flap creation with a femtosecond laser," Journal of Cataract and Refractive Surgery, 31(11), 2227-2229 (2005).

[70] C. Hieber, G. Ihra, S. Nachbar, A. Aloy, A. Kashanipour, and F. Coraim, "Near-fatal paradoxical gas embolism during gynecological laparoscopy," Acta Obstet Gynecol Scand, 79(10), 898-9 (2000).

[71] N. Akhtar, W. Jafri, and T. Mozaffar, "Cerebral artery air embolism following an esophagogastroscopy: a case report," Neurology, 56(1), 136-7 (2001).

[72] F. Kodama, T. Ogawa, M. Hashimoto, Y. Tanabe, Y. Suto, and T. Kato, "Fatal air embolism as a complication of CT-guided needle biopsy of the lung," Journal of Computer Assisted Tomography, 23(6), 949-951 (1999).

[73] J. D. Tobias, J. O. Johnson, D. F. Jimenez, C. M. Barone, and D. S. McBride, Jr., "Venous air embolism during endoscopic strip craniectomy for repair of craniosynostosis in infants," Anesthesiology, 95(2), 340-2 (2001).

[74] M. Arcari, S. D. Phillips, P. Gibbs, S. M. Rela, and N. D. Heaton, "An investigation into the risk of air embolus during veno-venous bypass in orthotopic liver transplantation," Transplantation, 68(1), 150-2 (1999).

[75] G. Thiery, F. Le Corre, P. Kirstetter, A. Sauvanet, J. Belghiti, and J. Marty, "Paradoxical air embolism during orthoptic liver transplantation: diagnosis by transoesophageal echocardiography," Eur J Anaesthesiol, 16(5), 342-5 (1999).

[76] R. F. Wolf, W. J. Sluiter, A. Ballast, R. Verwer, R. M. van Dam, and M. J. Slooff, "Venous air embolism, preservation/reperfusion injury, and the presence of intravascular air collection in human donor livers: a retrospective clinical study," Transpl Int, 8(3), 201-6 (1995).

[77] E. W. Ely, R. D. Hite, A. M. Baker, M. M. Johnson, D. L. Bowton, and E. F. Haponik, "Venous air embolism from central venous catheterization: a need for increased physician awareness," Crit Care Med, 27(10), 2113-7 (1999).

[78] O. Vignaux, P. Borrego, L. Macron, A. Cariou, and Y. E. Claessens, "Cardiac gas embolism after central venous catheter removal," Undersea Hyperb Med, 32(5), 325-6 (2005).

[79] T. J. Porea, J. F. Margolin, and M. M. Chintagumpala, "Radiological case of the month: pulmonary air embolus with home antibiotic infusion," Arch Pediatr Adolesc Med, 155(8), 963-4 (2001).

[80] The US Food and Drug Administration, and Bristol Myers Squibb Imaging, [IMPORTANT DRUG WARNING: Serious Cardiopulmonary Reactions], Washington, DC(2007).

[81] B. W. Holcomb, J. E. Loyd, B. F. Byrd, 3rd, T. T. Wilsdorf, T. Casey-Cato, W. R. Mason, and I. M. Robbins, "Iatrogenic paradoxical air embolism in pulmonary hypertension," Chest, 119(5), 1602-5 (2001).

[82] A. Boussuges, F. Molenat, D. Carturan, P. Gerbeaux, and J. M. Sainty, "Venous gas embolism: Detection with pulsed Doppler guided by two-dimensional echocardiography," Acta Anaesthesiologica Scandinavica, 43(3), 328-332 (1999).

[83] A. Boussuges, D. Carturan, P. Ambrosi, G. Habib, J. M. Sainty, and R. Luccioni, "Decompression induced venous gas emboli in sport diving: Detection with 2D echocardiography and pulsed Doppler," International Journal Of Sports Medicine, 19(1), 7-11 (1998).

[84] B. D. Butler, and W. P. Morris, "Transesophageal Echocardiographic Study Of Decompression-Induced Venous Gas Emboli," Undersea & Hyperbaric Medicine, 22(2), 117-128 (1995).

[85] B. D. Butler, S. Luehr, and J. Katz, "Venous Gas Embolism - Time Course Of Residual Pulmonary Intravascular Bubbles," Undersea Biomedical Research, 16(1), 21-29 (1989).

[86] D. Wallach, H. Holtmann, H. Engelmann, and Y. Nophar, "Sensitization And Desensitization To Lethal Effects Of Tumor Necrosis Factor And Il-1," Journal Of Immunology, 140(9), 2994-2999 (1988).

[87] K. Bergh, A. Hjelde, O. J. Iversen, and A. O. Brubakk, "Variability Over Time Of Complement Activation Induced By Air Bubbles In Human And Rabbit Sera," Journal Of Applied Physiology, 74(4), 1811-1815 (1993).

[88] A. Hjelde, K. Bergh, A. O. Brubakk, and O. J. Iversen, "Complement Activation In Divers After Repeated Air/Heliox Dives And Its Possible Relevance To Dcs," Journal Of Applied Physiology, 78(3), 1140-1144 (1995).

[89] S. R. Kayar, E. O. Aukhert, M. J. Axley, L. D. Homer, and A. L. Harabin, "Lower decompression sickness risk in rats by intravenous injection of foreign protein," Undersea & Hyperbaric Medicine, 24(4), 329-335 (1997).

[90] A. Ersson, C. Linder, K. Ohlsson, and A. Ekholm, "Cytokine response after acute hyperbaric exposure in the rat," Undersea & Hyperbaric Medicine, 25(4), 217-221 (1998).

[91] A. Boussuges, E. Succo, I. Juhan-Vague, and J. M. Sainty, "Activation of coagulation in decompression illness," Aviation Space And Environmental Medicine, 69(2), 129-132 (1998).

[92] I. Brenner, R. J. Shephard, and P. N. Shek, "Immune function in hyperbaric environments, diving, and decompression," Undersea & Hyperbaric Medicine, 26(1), 27-39 (1999).

[93] C. A. Ward, D. McCullough, and W. D. Fraser, "Relation between complement activation and susceptibility to decompression sickness.," J Appl Physiol, 62, 1160-1166 (1987).

[94] A. Ersson, M. Walles, K. Ohlsson, and A. Ekholm, “Chronic hyperbaric exposure activates proinflammatory mediators in humans,” Journal Of Applied Physiology, 92(6), 2375-2380 (2002).

[95] T. S. Neuman, “Arterial Gas Embolism and Decompression Sickness,” News Physiol Sci, 17, 77-81 (2002).

[96] B. A. Hills, and B. D. Butler, “Size distribution of intravascular air emboli produced by decompression,” Undersea Biomed Res, 8(3), 163-70 (1981).

[97] R. S. Meltzer, P. W. Serruys, J. McGhie, N. Verbaan, and J. Roelandt, “Pulmonary wedge injections yielding left-sided echocardiographic contrast,” Br Heart J, 44(4), 390-4 (1980).

[98] A. Bouakaz, and N. de Jong, “WFUMB Safety Symposium on Echo-Contrast Agents: nature and types of ultrasound contrast agents,” Ultrasound Med Biol, 33(2), 187-96 (2007).

[99] D. Georgiadis, M. Kaps, M. Siebler, M. Hill, M. Konig, J. Berg, M. Kahl, P. Zunker, B. Diehl, and E. B. Ringelstein, “Variability of Doppler microembolic signal counts in patients with prosthetic cardiac valves,” Stroke, 26(3), 439-43 (1995).

[100] W. Mullges, D. Franke, W. Reents, and J. Babin-Ebell, “Brain microembolic counts during extracorporeal circulation depend on aortic cannula position,” Ultrasound Med Biol, 27(7), 933-6 (2001).

[101] R. Y. Nishi, [Doppler and ultrasonic bubble detection] Saunders, London(1993).

[102] D. N. Walder, A. Evans, and H. V. Hempleman, “Ultrasonic monitoring of decompression,” Lancet 1, 897–898 (1968).

[103] R. G. Eckenhoff, C. S. Olstad, and G. Carrod, “Human-dose response relationship for decompression and endogenous bubble formation,” J Appl Physiol 69, 914–918 (1990).

[104] B. A. Hills, and B. D. Butler, “Size distribution of intra-vascular emboli produced by decompression,” Undersea Biomed Res 8, 163–170 (1981).

[105] M. Malconian, P. B. Rock, and J. Devine, “Operation Everest II: altitude decompression sickness during repeated altitude exposure,” Aviat Space Environ Med 58, 679–682 (1987).

[106] M. A. Chappell, and S. J. Payne, “A method for the automated detection of venous gas bubbles in humans using empirical mode decomposition,” Ann Biomed Eng, 33(10), 1411-21 (2005).

[107] K. Reynaud, D. Nogueira, R. Cortvrindt, R. Kurzawa, and J. Smitz, “Confocal microscopy: principles and applications to the field of reproductive biology,” Folia Histochemica Et Cytobiologica, 39(2), 75-85 (2001).

[108] B. Cheng, D. Y. Lin, X. G. Wang, D. Y. Chen, and W. Y. Ma, “Application of two-photon excitation fluorescence imaging to real-time investigation of mouse preimplantation embryo,” Spectroscopy and Spectral Analysis, 26(2), 193-197 (2006).

[109] E. Brustein, N. Marandi, Y. Kovalchuk, P. Drapeau, and A. Konnerth, “"In vivo" monitoring of neuronal network activity in zebrafish by two-photon Ca2+ imaging,” Pflugers Archiv-European Journal of Physiology, 446(6), 766-773 (2003).

[110] J. M. Squirrell, D. L. Wokosin, J. G. White, and B. D. Bavister, “Long-term two-photon fluorescence imaging of mammalian embryos without compromising viability,” Nature Biotechnology, 17(8), 763-767 (1999).

[111] V. Daria, O. Nakamura, C. Palmes-Saloma, and S. Kawata, “Enhanced depth penetration in imaging of turbid biological samples by two-photon fluorescence microscopy,” Japanese Journal of Applied Physics Part 2-Letters, 37(8A), L959-L961 (1998).

[112] R. G. Summers, D. W. Piston, K. M. Harris, and J. B. Morrill, “The orientation of first cleavage in the sea urchin embryo, Lytechinus variegatus, does not specify the axes of bilateral symmetry,” Developmental Biology, 175(1), 177-183 (1996).

[113] S. W. Chu, S. Y. Chen, T. H. Tsai, T. M. Liu, C. Y. Lin, H. J. Tsai, and C. K. Sun, “In vivo developmental biology study using noninvasive multi-harmonic generation microscopy,” Optics Express, 11(23), 3093-3099 (2003).

[114] C. K. Sun, S. W. Chu, S. Y. Chen, T. H. Tsai, T. M. Liu, C. Y. Lin, and H. J. Tsai, “Higher harmonic generation microscopy for developmental biology,” Journal of Structural Biology, 147(1), 19-30 (2004).

[115] J. Squier, and M. Muller, “High resolution nonlinear microscopy: A review of sources and methods for achieving optimal imaging,” Review of Scientific Instruments, 72(7), 2855-2867 (2001).

[116] V. V. Tuchin, [Optical Clearing of Tissues and Blood] SPIE Press, (2005).

[117] V. V. Tuchin, [Tissue Optics: Light Scattering Methods and Instruments for Medical Diagnosis] SPIE, Bellingham, WA(2000).

[118] R. K. Manapuram, V. R. Manne, N. Sudheendran, E. F. Carbajal, and K. V. Larin, "Quantification of microbubbles in blood with phase-sensitive SSOCT." SPIE 7563, 75630B-7.

[119] J. Ophir, I. Cespedes, H. Ponnekanti, Y. Yazdi, and X. Li, “Elastography: a quantitative method for imaging the elasticity of biological tissues,” Ultrasonic Imaging, 13(2), 111-34 (1991).

[120] M. F. Insana, [Elasticity Imaging] John Wiley & Sons, Inc., Hoboken, NJ(2006).

[121] S. R. Agliamov, and A. R. Skovoroda, “[Mechanical properties of soft biological tissues],” Biofizika, 45(6), 1137-45 (2000).

[122] A. P. Sarvazian, [Elastic Properties Of Soft Tissues] Academic Press, (2001).

[123] M. M. Doyley, F. Mastik, C. L. de Korte, S. G. Carlier, E. I. Céspedes, P. W. Serruys, N. Bom, and A. F. W. van der Steen, “Advancing intravascular ultrasonic palpation toward clinical applications,” Ultrasound in Medicine & Biology, 27(11), 1471-1480 (2001).

[124] C. L. de Korte, M. J. Sierevogel, F. Mastik, C. Strijder, J. A. Schaar, E. Velema, G. Pasterkamp, P. W. Serruys, and A. F. W. van der Steen, "Identification of Atherosclerotic Plaque Components With Intravascular Ultrasound Elastography In Vivo: A Yucatan Pig Study," Circulation, 105(14), 1627-1630 (2002).

[125] E. E. Konofagou, J. D'Hooge, and J. Ophir, "Myocardial elastography--a feasibility study in vivo," Ultrasound in Medicine & Biology, 28(4), 475-482 (2002).

[126] A. Manduca, T. E. Oliphant, M. A. Dresner, J. L. Mahowald, S. A. Kruse, E. Amromin, J. P. Felmlee, J. F. Greenleaf, and R. L. Ehman, "Magnetic resonance elastography: Non-invasive mapping of tissue elasticity," Medical Image Analysis, 5(4), 237-254 (2001).

[127] P. J. McCracken, A. Manduca, J. Felmlee, and R. L. Ehman, "Mechanical transient-based magnetic resonance elastography," Magnetic Resonance in Medicine, 53(3), 628-639 (2005).

[128] R. Muthupillai, D. Lomas, P. Rossman, J. Greenleaf, A. Manduca, and R. Ehman, "Magnetic resonance elastography by direct visualization of propagating acoustic strain waves," Science, 269(5232), 1854-1857 (1995).

[129] E. E. W. Van Houten, M. M. Doyley, F. E. Kennedy, J. B. Weaver, and K. D. Paulsen, "Initial in vivo experience with steady-state subzone-based MR elastography of the human breast," Journal of Magnetic Resonance Imaging, 17(1), 72-85 (2003).

[130] J. B. Weaver, M. Doyley, Y. Cheung, F. Kennedy, E. L. Madsen, E. E. W. Van Houten, and K. Paulsen, "Imaging the shear modulus of the heel fat pads," Clinical Biomechanics, 20(3), 312-319 (2005).

[131] L. Xu, Y. Lin, J. C. Han, Z. N. Xi, H. Shen, and P. Y. Gao, "Magnetic resonance elastography of brain tumors: preliminary results," Acta Radiologica, 48(3), 327-330 (2007).

[132] K. D. Costa, "Single-cell elastography: Probing for disease with the atomic force microscope," Disease Markers, 19(2/3), 139-154 (2003).

[133] H. Haga, M. Nagayama, K. Kawabata, E. Ito, T. Ushiki, and T. Sambongi, "Time–lapse viscoelastic imaging of living fibroblasts using force modulation mode in AFM," Journal of Electron Microscopy, 49(3), 473-481 (2000).

[134] R. Höper, T. Gesang, W. Possart, O. D. Hennemann, and S. Boseck, "Imaging elastic sample properties with an atomic force microscope operating in the tapping mode," Ultramicroscopy, 60(1), 17-24 (1995).

[135] E. Nagao, and J. A. Dvorak, "Phase Imaging by Atomic Force Microscopy: Analysis of Living Homoiothermic Vertebrate Cells," Biophysical Journal, 76(6), 3289-3297 (1999).

[136] Y. Hong, X. Liu, Z. Li, X. Zhang, M. Chen, and Z. Luo, "Real-time Ultrasound Elastography in the Differential Diagnosis of Benign and Malignant Thyroid Nodules," Journal of Ultrasound Medicine, 28(7), 861-867 (2009).

[137] J. Ophir, S. K. Alam, F. Kallel, E. Konofagou, T. Varghese, B. Garra, and T. Krouskop, "Elastography: Ultrasonic Estimation and Imaging of the Elastic Properties of Tissues," Proceedings of the Institution of Mechanical Engineers -- Part H -- Journal of Engineering in Medicine (Professional Engineering Publishing), 213(3), 203-233 (1999).

[138] J. Ophir, I. Céspedes, H. Ponnekanti, Y. Yazdi, and X. Li, "Elastography: A quantitative method for imaging the elasticity of biological tissues," Ultrasonic Imaging, 13(2), 111-134 (1991).

[139] J. Ophir, F. Kallel, T. Varghese, M. Bertrand, I. Céspedes, and H. Ponnekanti, "Elastography: A systems approach," International Journal of Imaging Systems and Technology, 8(1), 89-103 (1997).

[140] M. Tristam, D. C. Barbosa, D. O. Cosgrove, J. C. Bamber, and C. R. Hill, "Application of fourier analysis to clinical study of patterns of tissue movement," Ultrasound in Medicine & Biology, 14(8), 695-707 (1988).

[141] M. Tristam, D. C. Barbosa, D. O. Cosgrove, D. K. Nassiri, J. C. Bamber, and C. R. Hill, "Ultrasonic study of in vivo kinetic characteristics of human tissues," Ultrasound in Medicine & Biology, 12(12), 927-937 (1986).

[142] J. J. Finneran, and M. C. Hastings, "A continuous-wave ultrasound system for displacement amplitude and phase measurement," The Journal of the Acoustical Society of America, 115(6), 3202-3209 (2004).

[143] J. F. Greenleaf, M. Fatemi, and M. Insana, "SELECTED METHODS FOR IMAGING ELASTIC PROPERTIES OF BIOLOGICAL TISSUES," Annual Review of Biomedical Engineering, 5(1), 57-78 (2003).

[144] K. J. Parker, and R. M. Lerner, "Sonoelasticity of organs: shear waves ring a bell," Journal of Ultrasound Medicine, 11(8), 387-392 (1992).

[145] S. G. Adie, X. Liang, B. F. Kennedy, R. John, D. D. Sampson, and S. A. Boppart, "Spectroscopic optical coherence elastography," Optics Express, 18(25), 25519-34 (2010).

[146] D. Duncan, and S. Kirkpatrick, "Performance analysis of a maximum-likelihood speckle motion estimator," Optics Express, 10(18), 927-941 (2002).

[147] D. D. Duncan, and S. J. Kirkpatrick, "Processing algorithms for tracking speckle shifts in optical elastography of biological tissues," Journal of Biomedical Optics, 6(4), 418-426 (2001).

[148] S. Rigozzi, R. Müller, and J. G. Snedeker, "Local strain measurement reveals a varied regional dependence of tensile tendon mechanics on glycosaminoglycan content," Journal of Biomechanics, 42(10), 1547-1552 (2009).

[149] Y. Zhang, R. T. Brodell, E. N. Mostow, C. J. Vinyard, and H. Marie, "In vivo skin elastography with high-definition optical videos," Skin Research and Technology, 15(3), 271-282 (2009).

[150] K. Sean, "Imaging the mechanical properties of biological tissues." MI3.

[151] G. Le Goualher, A. Perchant, M. Genet, C. Cavé, B. Viellerobe, F. Berier, B. Abrat, and N. Ayache, [Towards Optical Biopsies with an Integrated Fibered Confocal Fluorescence Microscope] Springer Berlin / Heidelberg, (2004).

[152] J. G. Snedeker, A. Ben Arav, Y. Zilberman, G. Pelled, and D. Gazit, "Functional Fibered Confocal Microscopy: A Promising Tool for Assessing Tendon Regeneration," Tissue Engineering Part C: Methods, 15(3), 485-491 (2009).

[153] R. H. Kennedy, W. M. Bourne, and J. A. Dyer, "A 48-year clinical and epidemiologic study of keratoconus," American Journal of Ophthalmology, 101, 267-273 (1986).

[154] J. H. Krachmer, R. S. Feder, and M. W. Belin, "Keratoconus and related noninflammatory corneal thinning disorders," Survey of Ophthalmology, 28(4), 293-322 (1984).

[155] Y. S. Rabinowitz, "Keratoconus," Survey of Ophthalmology, 42(4), 111-134 (1998).

[156] L. T. Nordan, "Keratoconus: diagnosis and treatment," International Ophthalmology Clinics, 37(1), 51-63 (1997).

[157] M. Tanter, D. Touboul, J. L. Gennisson, J. Bercoff, and M. Fink, "High-resolution quantitative imaging of cornea elasticity using supersonic shear imaging," IEEE Transactions on Medical Imaging, 28(12), 1881-93 (2009).

[158] I. F. Comaish, and M. A. Lawless, "Progressive post-LASIK keratectasia: biomechanical instability or chronic disease process?," Journal of Cataract and Refractive Surgery, 28(12), 2206-13 (2002).

[159] W. J. Dupps, Jr., "Biomechanical modeling of corneal ectasia," Journal of Refractive Surgery, 21(2), 186-90 (2005).

[160] T. Juhasz, F. H. Loesel, R. M. Kurtz, C. Horvath, J. F. Bille, and G. Mourou, "Corneal refractive surgery with femtosecond lasers," Selected Topics in Quantum Electronics, IEEE Journal of, 5(4), 902-910 (1999).

[161] M. D. Twa, J. J. Nichols, C. E. Joslin, P. S. Kollbaum, T. B. Edrington, M. A. Bullimore, G. L. Mitchell, K. J. Cruickshanks, and D. J. Schanzlin, "Characteristics of Corneal Ectasia After LASIK for Myopia," Cornea, 23(5), 447-457 (2004).

[162] K. W. Hollman, S. Y. Emelianov, J. H. Neiss, G. Jotyan, G. J. Spooner, T. Juhasz, R. M. Kurtz, and M. O'Donnell, "Strain imaging of corneal tissue with an ultrasound elasticity microscope," Cornea, 21(1), 68-73 (2002).

[163] J. Liu, and C. J. Roberts, "Influence of corneal biomechanical properties on intraocular pressure measurement: Quantitative analysis," Journal of Cataract & Refractive Surgery, 31(1), 146-155 (2005).

[164] D. Alonso-Caneiro, K. Karnowski, B. J. Kaluzny, A. Kowalczyk, and M. Wojtkowski, "Assessment of corneal dynamics with high-speed swept source Optical Coherence Tomography combined with an air puff system," Optics Express, 19(15), 14188-14199 (2011).

[165] K. R. Heys, M. G. Friedrich, and R. J. Truscott, "Presbyopia and heat: changes associated with aging of the human lens suggest a functional role for the small heat shock protein, alpha-crystallin, in maintaining lens flexibility," Aging Cell, 6(6), 807-15 (2007).

[166] W. N. Charman, "The eye in focus: accommodation and presbyopia," Clinical and Experimental Optometry, 91(3), 207-25 (2008).

[167] K. Vogelsang, "[100 Years of Helmholtz' accommodation theory]," Klin Monbl Augenheilkd Augenarztl Fortbild, 126(6), 762-5 (1955).

[168] J. F. Koretz, and G. H. Handelman, "Model of the accommodative mechanism in the human eye," Vision Research, 22(8), 917-927 (1982).

[169] A. Glasser, "Restoration of accommodation: surgical options for correction of presbyopia," Clinical and Experimental Optometry, 91(3), 279-95 (2008).

[170] [Anatomy of the Human Eye] http://www.mastereyeassociates.com/, (2012).

[171] E. L. Smith, 3rd, L. F. Hung, J. Huang, T. L. Blasdel, T. L. Humbird, and K. H. Bockhorst, "Effects of optical defocus on refractive development in monkeys: evidence for local, regionally selective mechanisms," Investigative Ophthalmology and Visual Science, 51(8), 3864-73 (2010).

[172] M. D. Roberts, Y. Liang, I. A. Sigal, J. Grimm, J. Reynaud, A. Bellezza, C. F. Burgoyne, and J. C. Downs, "Correlation between local stress and strain and lamina cribrosa connective tissue volume fraction in normal monkey eyes," Investigative Ophthalmology and Visual Science, 51(1), 295-307 (2010).

[173] M. Orescanin, and M. Insana, "Shear modulus estimation with vibrating needle stimulation," IEEE Transactions on Ultrasonics, Ferroelectrics and Frequency Control, 57(6), 1358-67 (2010).

[174] C. Li, Z. Huang, and R. K. Wang, "Elastic properties of soft tissue-mimicking phantoms assessed by combined use of laser ultrasonics and low coherence interferometry," Optics Express, 19(11), 10153-10163 (2011).

[175] [Information for Manufacturers Seeking Marketing Clearance of Diagnostic Ultrasound Systems and Transducers] US Department of Health and human services, Silver Spring(2008).

[176] M. D'Onofrio, A. Gallotti, and R. P. Mucelli, "Tissue Quantification With Acoustic Radiation Force Impulse Imaging: Measurement Repeatability and Normal Values in the Healthy Liver," American Journal of Roentgenology, 195(1), 132-136 (2010).

[177] Z. Xiaoming, and J. F. Greenleaf, "Estimation of tissue's elasticity with surface wave speed," Journal of the Acoustical Society of America, 122(5), 2522-2525 (2007).

[178] J. Bercoff, M. Tanter, and M. Fink, "Supersonic shear imaging: a new technique for soft tissue elasticity mapping," IEEE Transactions on Ultrasonics, Ferroelectrics and Frequency Control, 51(4), 396-409 (2004).

[179] M. Tanter, J. Bercoff, A. Athanasiou, T. Deffieux, J. L. Gennisson, G. Montaldo, M. Muller, A. Tardivon, and M. Fink, "Quantitative assessment of breast lesion viscoelasticity: initial clinical results using supersonic shear imaging," Ultrasound in Medicine and Biology 34(9), 1373-86 (2008).

[180] D. A. Luce, "Determining in vivo biomechanical properties of the cornea with an ocular response analyzer," Journal of Cataract and Refractive Surgery, 31(1), 156-62 (2005).

[181] G. J. Orssengo, and D. C. Pye, "Determination of the true intraocular pressure and modulus of elasticity of the human cornea in vivo," Bulletin of Mathematical Biology, 61(3), 551-72 (1999).

[182] R. F. Fisher, "The elastic constants of the human lens," Journal of Physiology, 212(1), 147-80 (1971).

[183] R. F. Fisher, "Presbyopia and the changes with age in the human crystalline lens," Journal of Physiology, 228(3), 765-79 (1973).

[184] R. F. Fisher, "The force of contraction of the human ciliary muscle during accommodation," Journal of Physiology, 270(1), 51-74 (1977).

[185] B. K. Pierscionek, " In vitro alteration of human lens curvature by radial stretching," Experimental Eye Research, 57, 629-635 (1993).

[186] B. K. Pierscionek, "Age-related response of human lenses to stretching forces," Experimental Eye Research, 60(325-332), (1995).

[187] N. M. Ziebarth, D. Borja, E. Arrieta, M. Aly, F. Manns, I. Dortonne, D. Nankivil, R. Jain, and J.-M. Parel, "Role of the lens capsule on the mechanical accommodative response in a lens stretcher," Investigative Ophthalmology and Visual Science, 49(10), 4490-4496 (2008).

[188] H. Pau, and J. Kranz, "The increasing sclerosis of the human lens with age and its relevance to accommodation and presbyopia," Graefe's Archive of Clinical and Experimental Ophthalmology, 229, 294-296 (1991).

[189] A. Glasser, and M. C. W. Campbell, “Biometric, optical, and physical changes in the isolated human crystalline lens with age in relation to presbyopia,” Vision Research, 39(11), 1991-2015 (1999).

[190] Y. Kikkawa, and T. Sato, “Elastic properties of the lens,” Experimental Eye Research, 2, 210-215 (1963).

[191] G. W. H. M. van Alphen, and W. P. Graebel, “Elasticity of tissues involved in accommodation,” Vision Research, 31(7-8), 1417-1438 (1991).

[192] G. Czygan, and C. Hartung, “Mechanical testing of isolated senile human eye lens nuclei,” Medical Engineering and Physics, 18(5), 345-349 (1996).

[193] K. R. Heys, S. L. Cram, and R. J. Truscott, “Massive increase in the stiffness of the human lens nucleus with age: the basis for presbyopia?,” Molecular Vision, 10, 956-63 (2004).

[194] M. A. Reilly, G. Perry, and N. Ravi, “A dynamic microindentation device with electrical contact detection,” Review of Scientific Instruments, 80, 015105-1-9 (2009).

[195] M. A. Reilly, and N. Ravi, “Microindentation of the young porcine ocular lens,” Journal of Biomechanical Engineering, 131, 044502-1-4 (2009).

[196] H. A. Weeber, G. Eckert, W. Pechhold, and R. G. L. van der Heijde, “Stiffness gradient in the crystalline lens,” Graefe's Archive of Clinical and Experimental Ophthalmology, 245, 1357-1366 (2007).

[197] H. A. Weeber, G. Eckert, F. Soergel, C. H. Meyer, W. Pechhold, and R. G. L. van der Heijde, “Dynamic mechanical properties of human lenses,” Experimental Eye Research, 80(3), 425-434 (2005).

[198] K. R. Heys, S. L. Cram, and R. J. W. Truscott, “ Massive increase in the stiffness of the human lens nucleus with age: the basis for presbyopia?,” Molecular Vision, 10, 956-963 (2004).

[199] T. N. Erpelding, K. W. Hollman, and M. O'Donell, “Mapping age-related elasticity changes in porcine lenses using bubble-based acoustic radiation force,” Experimental Eye Research, 84, 332-341 (2007).

[200] H. A. Weeber, and G. L. van der Heijde, “On the relationship between lens stiffness and accommodative amplitude,” Experimental Eye Research, 85, 602-607 (2007).

[201] J. Schmitt, “OCT elastography: imaging microscopic deformation andstrain of tissue,” Optics Express, 3(6), 199-211 (1998).

[202] B. F. Kennedy, T. R. Hillman, R. A. McLaughlin, B. C. Quirk, and D. D. Sampson, “In vivo dynamic optical coherence elastography using a ring actuator,” Optics Express, 17(24), 21762-21772 (2009).

[203] X. Liang, S. G. Adie, R. John, and S. A. Boppart, “Dynamic spectral-domain optical coherence elastography for tissue characterization,” Optics Express, 18(13), 14183-14190 (2010).

[204] X. Liang, A. L. Oldenburg, V. Crecea, E. J. Chaney, and S. A. Boppart, “Optical micro-scale mapping of dynamic biomechanical tissue properties,” Optics Express, 16(15), 11052-11065 (2008).

[205] M. H. De la Torre-Ibarra, P. D. Ruiz, and J. M. Huntley, “Double-shot depth-resolved displacement field measurement using phase-contrast spectral optical coherence tomography,” Optics Express, 14(21), 9643-9656 (2006).

[206] M. R. Ford, J. W. J. Dupps, A. M. Rollins, A. S. Roy, and Z. Hu, “Method for optical coherence elastography of the cornea,” Journal of Biomedical Optics, 16(1), 016005-7 (2011).

[207] M. Gora, K. Karnowski, M. Szkulmowski, B. J. Kaluzny, R. Huber, A. Kowalczyk, and M. Wojtkowski, “Ultra high-speed swept source OCT imaging of the anterior segment of human eye at 200 kHz with adjustable imaging range,” Optics Express, 17(17), 14880-14894 (2009).

[208] N. Sudheendran, V. R. Manne, R. K. Manapuram, S. A. Baranov, S. Aglyamov, S. Emelianov, and K. V. Larin, "Measurement of vibrations induced on the surface of crystalline eye lens using PhS-SDOCT." SPIE 7550, 755007-8.

[209] T. J. Hall, M. Bilgen, M. F. Insana, and T. A. Krouskop, "Phantom materials for elastography," IEEE Transactions on Ultrasonics, Ferroelectrics and Frequency Control, 44(6), 1355-1365 (1997).

[210] X. Zhang, and J. F. Greenleaf, "Estimation of tissue's elasticity with surface wave speed," Journal of Acoustic Society of America, 122(5), 2522-2525 (2007).

[211] X. Liang, M. Orescanin, K. S. Toohey, M. F. Insana, and S. A. Boppart, "Acoustomotive optical coherence elastography for measuring material mechanical properties," Optics Letters, 34(19), 2894-6 (2009).

[212] C. G. Liddle, J. P. Putnam, and O. P. Huey, "Alteration of life span of mice chronically exposed to 2.45 GHz CW microwaves," Bioelectromagnetics, 15(3), 177-181 (1994).

[213] S. Hayes, C. Boote, J. Lewis, J. Sheppard, M. Abahussin, A. J. Quantock, C. Purslow, M. Votruba, and K. M. Meek, "Comparative Study of Fibrillar Collagen Arrangement in the Corneas of Primates and Other Mammals," The Anatomical Record: Advances in Integrative Anatomy and Evolutionary Biology, 290(12), 1542-1550 (2007).

[214] W. Radner, M. Zehetmayer, R. Aufreiter, and R. Mallinger, "Interlacing and Cross-Angle Distribution of Collagen Lamellae in the Human Cornea," Cornea, 17(5), 537-543 (1998).

[215] A. Mariampillai, B. A. Standish, N. R. Munce, C. Randall, G. Liu, J. Y. Jiang, A. E. Cable, I. A. Vitkin, and V. X. D. Yang, "Doppler optical cardiogram gated 2D color flow imaging at 1000 fps and 4D *in vivo* visualization of embryonic heart at 45 fps on a swept source OCT system," Optics Express, 15(4), 1627-1638 (2007).

[216] B. Vakoc, S. Yun, J. de Boer, G. Tearney, and B. Bouma, "Phase-resolved optical frequency domain imaging," Optics Express, 13(14), 5483-5493 (2005).